

Copyright is owned by the Author of the thesis. Permission is given for a copy to be downloaded by an individual for the purpose of research and private study only. The thesis may not be reproduced elsewhere without the permission of the Author.

**Vertical and Lateral Variations of Grainsize and  
Pyroclast Componentry in the Taupo 232 CE Y2  
Fall Deposit: Implications for Spatiotemporal  
Deposition and Conduit Conditions in Large  
Plinian Eruptions.**

A thesis presented in partial fulfillment of the requirements for the  
degree of

*Magister Scientiarum*

in

Earth Science

At Massey University, Manawatū, New Zealand.

Hannah Walters

2020



# Abstract

The Taupo Volcanic Zone is one of the most frequent producers of Plinian eruptions globally, which constitute one of the most powerful natural disasters on Earth. These types of eruptions can eject volumes of tephra  $>10 \text{ km}^3$  into the atmosphere. The dispersal and sedimentation of pyroclasts in Plinian eruptions, as well as the high risk of pyroclastic density current production, pose significant environmental and societal threats. Therefore, further understanding of the dynamics of these volcanic events is essential for hazard planning and decision making at many volcanoes across the globe.

The Hatepe pumice of the Taupo 232 CE eruption (Y2) is an extremely well-preserved example of a seemingly monotonous plinian fall deposit, and previous studies exhibit a lack of investigation into vertical and lateral deposit variations which would allow the reconstruction of eruption dynamics and deposition history. This study examined three tephra profiles using a combination of grain-size, componentry and clast density measurements, as well as microscopic analysis of juvenile pyroclast textures and petrographic analysis of foreign lithic components to define syn-eruption chronostratigraphic time markers. The juvenile components were grouped into five distinctive textural classes (C1 – C5) which showed a systematic increase in clast density and shear deformed bubbles and glass, respectively. From this, a tentative conduit model for the time immediately prior to magma fragmentation was developed to explain the strong horizontal gradients in magma density and estimate radial extents of the variably vesiculated and shear-deformed proportions of the magma. Identification and distinction of foreign lithic lithologies and broad estimates of their likely depth of origin showed that deep excavation of plutonic country rock above the magma mush reservoir occurred strongly during onset of the eruption, but rapidly declined thereafter. The chronostratigraphic time markers, determined through componentry analysis, can be used in future computational studies as a real-world test for the validation of plume and ash-dispersal models. This research will allow for the possibility of further investigations to add more complexity to the understanding of the Y2 eruption and large Plinian eruptions elsewhere.



# Table of Contents

List of Figures .....	vii
List of Tables.....	ix
Acknowledgements .....	xi
<b>1 Introduction.....</b>	<b>12</b>
<b>2 Background Information .....</b>	<b>14</b>
2.1 Explosive Eruptions .....	14
2.2 Plinian Eruptions .....	15
2.2.1 Plinian Eruption Plume and Cloud Dynamics .....	16
2.2.2 Pyroclastic Density Currents.....	18
2.2.3 Hazards .....	18
2.3 Pyroclastic Deposits .....	19
2.3.1 Fall Deposits .....	19
2.3.2 Ignimbrite Deposits.....	20
2.4 Setting of the TVZ and Taupo Volcano .....	20
2.5 Taupo 232 CE Eruption.....	21
2.6 Y2 Deposit and its Characteristics .....	23
2.6.1 Ash Beds within the Y2 .....	25
<b>3 Methodology .....</b>	<b>28</b>
3.1 Reconnaissance Mapping .....	28
3.1.1 Identification of Key Sections for Downwind Variations .....	29
3.1.2 Identification of Key Sections for Cross Wind Variations .....	29
3.2 Sampling Procedures .....	29
3.2.1 Box Sampling.....	29
3.2.2 Incremental Sampling .....	29
3.3 Laboratory Work .....	30
3.3.1 Grain Size Analysis.....	30
3.3.2 Componentry Analysis.....	33
3.3.3 Thin Section and SEM Imaging.....	35
3.3.4 Density Measurements.....	36
3.3.5 Methodology Limitations.....	36
<b>4 Results.....</b>	<b>37</b>
4.1 Stratigraphic Profiles of Y2 and Their Downwind and Crosswind Variations .....	37
4.2 Grain Size Distributions .....	42
4.2.1 Vertical and Lateral Grainsize Variation .....	42
4.3 Componentry Descriptions.....	48
4.3.1 Juvenile Components .....	48
4.3.2 Non-Juvenile Components.....	55
4.3.3 Free Crystals .....	60

4.4	Vertical and Lateral Componentry Variations in Y2 .....	61
4.4.1	Componentry Variation with Grainsize.....	62
4.4.2	Vertical and Lateral Componentry Variations in the 1 Phi Size Class.....	65
<b>5</b>	<b>Discussion .....</b>	<b>74</b>
5.1	Deposit Types of the Y2 Eruption and Their Genesis .....	74
5.1.1	Timescales and Conditions of Pyroclasts Transport and Settling .....	75
5.2	Types of Pyroclast of the Y2 and Their Genesis .....	80
5.2.1	Characteristics and Formation of Juvenile Component Textures.....	81
5.2.2	Petrological Characteristics and Crustal Depth of Origin of Foreign Pyroclasts.....	87
5.3	Chronostratigraphic Markers of Synchronous Deposition in Plinian Fall Deposits.....	89
5.4	Y2 Eruption Evolution .....	91
<b>6</b>	<b>Summary and Conclusions .....</b>	<b>94</b>
	<b>References .....</b>	<b>98</b>
	<b>Appendix 1 .....</b>	<b>108</b>
	<b>Appendix 2 .....</b>	<b>118</b>

# List of Figures

Figure 2.1 Map of the Hikurangi margin.....	21
Figure 2.2 Distribution maps of ash beds within the Y2 eruption.....	27
Figure 4.1 ArcGIS Map displaying field localities.....	37
Figure 4.2 Photograph of Location 1 outcrop .....	38
Figure 4.3 Photographs of Location 2 outcrop .....	39
Figure 4.4 Photograph of Location 6 outcrop .....	41
Figure 4.5. Photograph of Location 8 outcrop.....	42
Figure 4.6 Grain size distribution histograms for each location .....	44
Figure 4.7 Scatter plot displaying graphic standard deviation. Histograms displaying selected fall lapilli samples .....	45
Figure 4.8 Vertical graphs comparing the mean values in phi plotted against normalised vertical height.....	46
Figure 4.9 Vertical graphs comparing the main mode values in phi against normalised vertical height .....	47
Figure 4.10 Vertical graphs comparing the <63 µm fraction in weight percent plotted against normalised vertical height .....	48
Figure 4.11 Macroscopic photographs of juvenile pumice classes .....	50
Figure 4.12 Microtextural SEM images of juvenile pumice components.....	51
Figure 4.13 Photographs of C5.....	52
Figure 4.14 SEM image of C5.....	53
Figure 4.15 Photographs of thick bubble walled, transperent, glassy pumice .....	54
Figure 4.16 Photographs displaying the range of ‘shallow’ non-juvenile clast types identified.....	56
Figure 4.17 Thin section photographs of the non-juvenile clasts.....	57
Figure 4.18 Photographs displaying the range of ‘intermediate’ non-juvenile lithologies. ....	59
Figure 4.19 Photographs of the ‘deep’ non-juvenile group.....	60
Figure 4.20 Photographs of free crystals .....	61



Figure 4.21 Individual componentry point count number percents against grain size (phi) .....	63
Figure 4.22 Location 8 tephra profile.....	64
Figure 4.23 Vertical graphs comparing combined point count number percent and normalised height .....	65
Figure 4.24 Vertical graphs displaying vertical variations in the 1 phi componentry .....	66
Figure 4.25 Vertical graphs displaying vertical variations in the 1 phi componentry. ....	67
Figure 4.26 Vertical graphs displaying C1:C2 ratio values for the 1 phi componentry .....	70
Figure 4.27 Vertical graphs displaying vertical variations in the 1 phi Non-Juvenile lithic components .....	72
Figure 5.1 Graph displaying terminal fall velocities with distance from vent.....	77
Figure 5.2 Graphs of terminal fall velocity against grain size .....	78
Figure 5.3 Graphs plotting surface area against <math><63 \mu\text{m}</math> .....	79
Figure 5.4 Schematic demonstrating particles settling out of plume through a dusty lower atmosphere .....	80
Figure 5.5 Tentative conduit model .....	86
Figure 5.6 Vertical profiles of Locations 5, 2 and 8 showing chronostratigraphic markers. ....	90

# List of Tables

Table 3.1 Tephra size classes in relation to grain size.....	28
Table 3.2 List of localities where box samples were taken .....	30
Table 3.3 List of localities where incremental samples were taken. ....	30
Table 3.4 List of sieve mesh sizes (phi and mm) .....	31
Table 3.5 Combined half and full grain size fractions used for componentry analysis .....	33
Table 3.6 Table of component classes and their descriptions. ....	34
Table 4.1 Summary of the average values ( $\rho_{ave}$ ), minima ( $\rho_{min}$ ), maxima ( $\rho_{max}$ ), 10th ( $\rho_{10}$ ) and 90th ( $\rho_{90}$ ) percentiles of the clast density distributions of the C1, C2, C3 and C4 componentry classes.....	55



# Acknowledgements

I would sincerely like to thank my supervisors: Assoc Prof. Gert Lube for all his time, ideas and continued guidance and support through the duration of this thesis. Prof. Colin Wilson for his extensive knowledge of the Taupō area and the Taupo 232 CE eruption as well as his help in the lab, ideas, and edits.

I would like to also thank the ECLPISE endeavour programme for funding this research project; Assoc Prof. Gert Lube and the VRS department at Massey, and the Graduate Women Manawatū (GWM) Charitable Trust for their financial help and support.

I would also like to thank New Zealand Forest Managers, Bubs Smith, Ngati Tūwharetoa, Wairakei Estate and Aaron Church, and Michelle McLeod from Timberlands Limited for their assistance and providing land access enabling me to undertake field research.

I would like to thank Dr Anja Moebis for all her help and support in the lab and especially SEM image acquisition, and James Ardo for all his work in the lab, of which I could not have done alone. I would also like to thank Matthew Irwin for his technical help during and after Covid-19.

I would like to thank Ermanno Brosch for the use of his sieving compilation datasheet and his additional technical support with Grapher and production of graphs.

I would also like to thank Dr Kate Arentsen for helping to organise fieldwork outings and booking accommodation.

I would also like to thank the Massey University Ecology department for the use of the microscope for componentry imaging.

I would like to make a special thank you to my friend, field buddy and photographer, Sarah Tapscott, for all of her emotional support, technical support in ArcMap, creation of figures and being the voice of reason though the creation of this thesis. I would also like to thank her for the time and effort she has put into formatting and editing.

I would like to make a big thank you to my friends for their continued support. Especially, a big thank you to Kayla Purvis and Shannen Mills for their help with reference formatting.

Last but not least, I would like to say a big thank you to my close family who have given me unconditional support for the duration of this thesis, and to whom have kept me going and encouraged me to pursue my dreams. I couldn't have done this without your love and support.

# 1 Introduction

Plinian eruptions are amongst the most powerful and most energetic phenomena associated with explosive volcanism on Earth (Walker, 1981b; Cioni et al, 2000). They produce eruption columns that eject more than one cubic kilometre of tephra into the stratosphere and are responsible for some of the most dangerous hazards caused by volcanoes on Earth. These eruptions are of particular interest due to the consequences that result, which have been witnessed frequently in human history, such as Pompeii 79AD, Pinatubo 1991, and Mt St Helens 1980 (Walker, 1980: 1981a; Carey & Sigurdsson, 1989). Plinian eruption plumes often fully or partially collapse, creating large pyroclastic density currents, which are one of the most devastating natural hazards known, propagating tens of kilometres from source (e.g. Wilson, 2001). Plinian eruption plumes reach heights in excess of 20 km, where stratospheric disturbances may affect global climate years after an eruption has ceased and where they pose a high risk to aviation safety. Stratospheric tephra dispersal over hundreds to thousands of square kilometres and their settling to the ground and loading onto infrastructure cause the most wide-spread primary volcanic hazard.

New Zealand is home to the world's most frequently active rhyolite volcano, the Taupo Caldera Complex, which has produced a number of large-scale Plinian eruptions in recent history. The 26.5 ka caldera forming Oruanui super-eruption ejected a total of  $\sim 530 \text{ km}^3$  magma, including a fall deposit of  $430 \text{ km}^3$  (Wilson, 1993; Sutton et al., 2000; Wilson, 2001; Manville et al, 2009). The youngest eruption from the Taupo Caldera Complex is the 232 CE Taupo eruption. This was a multi-stage event that comprised two large magmatic Plinian phases, three phreatomagmatic phases, one ignimbrite flow and a post-eruptive dome building event (Wilson & Walker, 1985; Wilson, 1993; Houghton et al 2010). The pyroclastic fall deposit produced by the smaller of the two Plinian phases, the Hatepe Plinian (Y2), is extremely well-preserved and provides a great opportunity to characterise and better understand the dynamics of Plinian eruption plumes.

Until now, the dynamics of high-magnitude volcanic plumes have been investigated by two different and not strictly complementary approaches: traditionally, bulk eruption properties, such as the eruption volume, plume dispersal, eruption mass discharge, approximate plume

height, and relative plume stability are estimated from detailed fieldwork on well-preserved pyroclastic fall deposits (Walker, 1980: 1981b). However, attempts to use vertical and lateral variations in Plinian fall deposits in order to reconstruct the eruption and deposition history remain sparse. Recently, and due to the advancement of computational power, plume dynamics, dispersal and sedimentation are also increasingly modelled computationally to simulate past and future events. Major obstacles exist today to successfully marry these two independent research strands: the measurable characteristics of natural deposits and numerically simulated fallout events use different physical characteristics that are not readily compared; the textures and facies of natural fall deposits reveal complex temporally (vertical) and spatially (lateral) variable characteristics; however, we cannot yet quantitatively translate and use this wealth of field data to attest to parental eruption dynamics; computational models need a variety of input and boundary conditions to allow realistic simulation results. Deriving these for past events is challenging.

In order to better characterise the processes associated with future Plinian events in New Zealand, this research was guided by the following objectives:

*Objective 1* encompasses the use of detailed tephrostratigraphic characterisation of proximal to medial tephra sequences of Y2 to add complexity to the eruption and deposition history of the Hatepe Plinian phase of the 232 CE eruption. This is achieved through characterising grain-size, pyroclast componentry, density and petrological variations in vertical profiles.

*Objective 2* is focused on deriving and testing concepts as to how vertical (time) and lateral (spatial) variation in the facies and textural characteristics of Plinian fall deposits can be used to reconstruct the eruption dynamics of their parental eruption plumes. To achieve this, detailed sampling and laboratory analysis of vertical profiles along the main plume dispersal direction and towards the fringes of the plume dispersal were conducted. If successful, the here targeted concepts and deposit characteristics may be used in future computational studies on Plinian eruption behaviour.

## 2 Background Information

### 2.1 Explosive Eruptions

Explosive eruptions are powered by rapid volatile exsolution in and fragmentation of rising magma producing primary ash, pumice, and ballistic pyroclasts. Bubbles nucleate and expand in rising magma that undergoes decompression, forming a low density foam that is fragmented upon eruption, creating pyroclastic material that is ejected at high speeds to feed convective volcanic plumes (Cashman et al., 2000; Gould, 2012), which can exceed heights of 40 km (Pyle, 2015). Explosive eruptions that produce sustained convective columns are typically influenced by the magma ascent rates and fragmentation determining the amount of thermal energy released. This controls the vigor of mixing of the plume with the surrounding atmosphere and thus controlling plume height. Deposition and dispersal of tephra is strongly controlled by eruption duration, temperature of the erupting pyroclasts, atmospheric winds and localized weather events (Pyle, 2015). Large explosive plumes can be sustained for many hours, provided the source magma and fragmentation continues to power the eruption. However, it is common for these columns to undergo partial or total column collapse, producing gravity driven, ground hugging pyroclastic density currents. These are a characteristic feature of many Plinian eruptions (see Section, 2.2.2)

Explosive eruptions can also include those that are driven by the interaction of external water (groundwater, lake, glacial meltwater, sea, etc.) and magma, triggering violent fragmentation as the cold water encountering hot magma expands into water vapour (steam) leading to explosions. These phreatomagmatic eruptions typically create finer-grained pyroclasts due to the violent fragmentation, leading to ash dominated deposits (Valentine, 1987; Morrissey et al., 2000; Druitt et al., 2007).

Fragmentation is the distinguishing factor of an explosive eruption and is the transformation of either liquid or solid magma into a mixture of gas and particles. Fragmentation typically accompanies rapid acceleration of magma to the surface during decompression of the magmatic system (Cashman et al., 2000; Cashman & Scheu, 2015). Fragmentation depths can be constrained by foreign lithic clasts observed in the deposits if the basement geology

is known, and can also be indicators of changes in the vent area or fragmentation region (Eichelberger & Koch, 1979; Wilson & Hildreth, 1997; Houghton & Carey, 2015).

Bubble nucleation and vesicularity provide insights into magma ascent and fragmentation conditions (Houghton & Wilson, 1989; Cashman, 2004; Houghton et al., 2010; Mitchell et al., 2018). The predominant volatiles in magma are water and carbon dioxide but also include sulphur, chlorine and fluorine, plus various compounds including these elements. As the magma rises, the melt becomes supersaturated, volatiles exsolve and bubbles grow and expand. With the growth of bubbles, coalescence also occurs, producing a permeable network through collapsed bubbles and stretched/sheared bubbles (Cashman, 2004).

## **2.2 Plinian Eruptions**

Plinian eruptions are amongst the most powerful of explosive volcanic events, ejecting mixtures of gas, and fragmented pyroclastic material into the atmosphere, producing eruptive columns and plumes reaching heights between 20 and 55 km (Walker, 1981b; Sigurdsson et al., 2015).

Plinian eruptions, which have occurred during the historic period, have been able to be observed and documented (Thorarinsson, 1950, 1954; Thordarsson & Einarsson, 1950; Carey & Sigurdsson, 1989; Walker, 1981b). However, these opportunities only present themselves on occasion, and the preserved plinian deposits have been studied in order to obtain information into the conditions surrounding these eruptions and to allow for a knowledge base to be built to reconstruct them, as seen in this thesis.

Plinian events are typically associated with “highly evolved calc-alkaline (high-silica) and alkaline (trachyte and phonolite)” magmas (Cioni et al., 2000), which eject pyroclastic material very rapidly and at high energies, reaching velocities between 100 and 400 m/s on leaving the vent. The resulting buoyant plume causes widespread tephra fallout over hundreds or thousands of square kilometres, influenced by interaction with atmospheric winds (Walker, 1980; Walker 1981a; Walker, 1981b; Carey & Sigurdsson, 1989; Sigurdsson et al., 2015).

To be classified as Plinian, the eruption has to be sustained; that is, the eruption is “sustained for a time comparable to that needed for the eruptive plume to reach its maximum potential



height” (Wilson et al., 1978; Walker, 1980, 1981b; Sigurdsson et al., 2015). Although these eruptions are known to contain different eruptive styles and depositional mechanisms they are defined by the intensity and volume of their dominant phase (Cioni et al., 2000).

The most important attributes by which to characterize these eruptions and their deposits are judged by Walker (1981b) to be a high content of juvenile pumiceous material; high discharge rates (increasing dispersal range); coarseness of pumice and continuity of discharge (producing a relatively homogenous deposit).

The deposits produced by Plinian eruptions are predominantly tephra fall deposits, which are typically characterised by their highly vesiculated pumiceous pyroclasts and well-sorted fall lapilli layers. These deposits usually contain blocks and bomb-sized (>64 mm) pyroclasts close to source with deposits becoming thinner and finer with distance from vent (Walker, 1981a, b). During eruptions of large magnitude, eruptive columns tend to become partially or fully unstable resulting in collapse and generating pyroclastic density currents (PDCs). Large magnitude eruptions are known to generally produce high intensity pyroclastic flows, linked to the potential for formation of calderas (Walker, 1984; Carey & Sigurdsson, 1989). However, small and frequent instabilities within the plume form intra-plinian PDCs that produce localised deposits within hundreds of metres, or kilometres, from vent (e.g Houghton et al., 2004).

### **2.2.1 Plinian Eruption Plume and Cloud Dynamics**

During Plinian eruptions, mixtures of gas and pyroclastic material are ejected from the vent into the atmosphere to form a high plume. Particles are transported in, then sedimented from plume producing tephra fall deposits. The motion in the atmosphere of a Plinian plume can be described in terms of three mechanically different regions, as outlined by Wilson (1976), Wilson et al. (1978, 1980) and Wilson & Walker (1987).

1. Gas- or jet-thrust region: where the gas-particle mixture rapidly loses its initial momentum due to turbulent entrainment of air at its margins, with the top of region typically not exceeding more than a few kilometers above the vent.
2. Convective or plume region: where incorporated air is heated, and the bulk density of the mixture is less than that of the surrounding atmosphere.

3. Umbrella cloud region: where the mixture, after having reached the height of neutral buoyancy ( $H_b$ ) continues to rise due to its momentum to a maximum height and then expands laterally due to density currents, atmospheric stratification and winds. The base of this section can be in the order of tens of kilometers high, but it is lower than the maximum height of the convective region (estimated through measurements of maximum clast size). This contrast has particularly been noted in the case of the 1991 Pinatubo eruption as documented by Fero et al. (2009) and Suzuki et al. (2016).

Tephra is the term given to all pyroclastic material ejected from the vent during an eruption (Cioni et al., 2000; Sigurdsson et al., 2015), and is characteristically dominated by three main components: pumice (shards), free crystals (phenocrysts liberated from magma in the volcanic explosion) and lithics (fragments of pre-existing solid rocks). Dense juvenile clasts are also produced and genetically related to pumice, but due to their greater densities they fall out of the plume closer to vent (Walker, 1981b). All ejected pyroclasts differ in shape, size and density, thus influencing the transport potential, time of transport, terminal velocity and ballistic potential. Ballistic clasts are those of a size and density that are little affected by air currents and land close to vent. Whereas pumiceous material of block and bomb ( $\geq 64$  mm), lapilli (2 – 64 mm) and ash ( $< 2$  mm) sized particles are readily transported into the plume and umbrella regions. From the umbrella cloud, the larger particles with higher terminal fall velocities fall out closer to vent, whereas the smaller particles can be carried up to hundreds of kilometres away from vent aided by the jet stream and atmospheric wind dispersal. The accumulation of this material causes a range of impacts on infrastructure, communities, and agriculture. The fine ash portion ( $< 63$   $\mu\text{m}$ ) has an effect on aviation transport and can affect the health of humans and animals (Bonadonna et al., 2015).

Transport and sedimentation of clasts from the plume are strongly dependent on the physical dynamics of the plume, as well as the terminal velocities and grain size distributions of clasts within the plume (Carey & Sparks, 1986).

The strength and duration of an eruption is controlled by the mass eruption rate and the continuity of magma and fragmentation from source. While the height of the plume largely relies on transfer of heat from particles to entrained air to create buoyancy by which the plume rises (Cashman & Rust, 2016; Bursik et al., 1992; Baines & Sparks, 2005)

### **2.2.2 Pyroclastic Density Currents**

PDCs consist of mixtures of hot volcanic ash, rocks and gas moving at high velocities across the ground surface aided by the force of gravity. These currents are a highly destructive and dangerous product of explosive volcanism (Druitt, 1998; Burgisser & Bergantz, 2002; Lube et al., 2020 and references therein). These phenomena have been the cause of thousands of deaths and constitute one of the greatest hazards associated with volcanoes. The survival rate for a person caught in a PDC is <20 % , compared to other volcanic hazards such as a major tephra fall for which there is a survival rate of >90 % (Blong, 2013). PDCs can be produced by a variety of volcanic eruption processes, such as the gravitational collapse of eruptive columns and plumes, lava dome collapse, as well as directed hydrothermal or magmatic blasts and phreatic or phreatomagmatic eruptions. These multiphase flows consist of a mixture of particles of varying sizes and densities plus gas, forming ground hugging flows that are often strongly controlled by the topographic relief of the landscape (Burgisser & Bergantz, 2002; Lube et al., 2020). These flows tend to segregate into two regions: the basal flow region, dominated by higher particle concentrations and a less dense, overriding turbulent ash cloud region (Druitt, 1998; Gladstone & Sparks, 2002; Lube et al., 2011), and in some cases a zone of intermediate turbulence and concentration can occur (Breard et al., 2016). Where PDCs are dominated by the basal concentrated part they are often termed pyroclastic flows. Where the less dense turbulent material dominates, PDCs are often referred to as pyroclastic surges (Sparks, 1976; Burgisser & Bergantz, 2002).

### **2.2.3 Hazards**

Volcanoes represent one of the major constituents of geohazards globally. Hazards associated with silicic volcanoes and silicic caldera systems in particular, such as Taupo volcano in New Zealand, result from explosive plinian and phreatoplinian eruption styles. These hazards are mainly related to PDCs and tephra fall. Understanding volcanic eruptions and their dynamics, as is the objective for this project, helps to create hazard maps and plume models that are necessary for the assessment and mitigation of volcanic hazards for future eruptions (e.g. Biasse et al., 2014; Barker et al., 2019; Bebbington, 2020).

Plinian eruptions are a major producer of PDCs, which are the primary cause of death during volcanic eruptions. PDCs result in the burial of communities and infrastructure, causing asphyxiation of humans and animals, damming and contamination of water sources, and on

occasion creating outburst floods (Bao et al., 2011). Tephra fall is the second major hazard represented by ballistic fall of hot ejecta close to vent, as well as widespread lapilli and ash fall, with impacts on infrastructure and aviation, as was experienced during the 2010 Eyjafjallajökull eruption in Iceland (Bonadonna et al., 2012). Fine ash can cause cardio-respiratory effects in humans and animals, as well as having severe impacts on agriculture. Tephra transported into the stratosphere and dispersed by wind currents can impact local and global climates for months to years after eruptions have ceased.

## **2.3 Pyroclastic Deposits**

### **2.3.1 Fall Deposits**

Fall deposits are produced as a result of sedimentation of pyroclastic material from atmospheric clouds, principally buoyant plumes and umbrella clouds, but also as buoyant plumes associated with PDCs (see previous Sections 2.2 and 2.2.2 for processes). Fall deposits are predominantly characterised, especially those of plinian style, by their well-sorted deposits that display exponential thinning and fining with distance from vent (Pyle, 1989; Sparks et al., 1992; Bonadonna & Houghton, 2005). The dispersal of material is influenced by the following factors: total mass, median diameter and standard deviation of material erupted, height of the eruption column, wind velocity and direction, and the nature of particle diffusion from the eruption column as well as the fragmentation of magma (Suzuki, 1983).

The homogeneity of tephra fall deposits is dependent on pyroclast sizes, densities, and consequent fall velocities. Ballistic clasts (little affected by wind) and coarse clasts such as those of block or bomb size (>64 mm) fall out closest to vent, as do smaller but denser clasts which have the same fall velocities (Walker, 1981a). However, fine ash and lapilli can be transported further by atmospheric winds and settle with slower terminal velocities. Changes in wind strength, wind direction, conditions at vent or atmospheric disturbances are reflected in the deposit through changes in grain size, lithologies and influxes of fine ash, that can be interpreted to reflect processes other than simple sedimentation from a buoyant plume. Influxes of fine ash into the deposits have been well documented and can occur as responses to atmospheric rainstorm events, or instabilities in the plume or eruptive column, and are deposited as density currents (collapses) or rain flush beds (atmospheric rainstorm) (Walker,

1981c; 1981d; Wilson & Walker, 1985). The density current deposits generally have better sorting (Brown & Andrews, 2015) whereas rain flush beds have poorer sorting as the ash and lapilli occur together (Talbot et al., 1994) Another major producer of ash beds in proximal tephra fall deposits is due to a change in eruptive style from ‘dry’ plinian to ‘wet’ phreatomagmatic, such changes are seen in the Taupo 232 CE sequence, described in Section 2.5.

### **2.3.2 Ignimbrite Deposits**

Ignimbrites are the deposits produced by concentrated PDCs (Section 2.2.2). Archetypically, ignimbrites are massive and thick deposits dominated by juvenile pumice and ash (Wilson et al., 1980). Upon deposition these flows can still be extremely hot reaching temperatures up to 800 °C, of which can result in welding of the deposit (welded ignimbrites) yielding a hard, rock-like deposit once cooled, e.g. the 350 – 340 ka Whakamaru Group ignimbrites in the Taupo area (Briggs, 1976a,b; Downs et al., 2014). PDC’s that are deposit with cooler temperatures (<550 – 600 °C) form unconsolidated ignimbrites (Walker, 1983), such as the Taupo ignimbrite during the 232 CE eruption considered in this thesis.

## **2.4 Setting of the TVZ and Taupo Volcano**

The North Island of New Zealand is marked by the Hikurangi subduction margin, where the Pacific plate subducts beneath the Indo-Australian plate, giving rise to the Taupo-Hikurangi arc-trench system of which the Taupo Volcanic Zone (TVZ) is the southernmost part (Figure 2.1: Cole, 1990; Wilson et al., 1995; Spinks et al., 2005). The TVZ is a c. 300 km long and c. 60 km wide volcanic zone (Wilson et al., 1995) that has been active for the last 2 Ma and dominated by rhyolitic volcanism for the past 1.84 Ma. The central segment of the TVZ is one of the world’s most vigorously active regions for Quaternary silicic volcanism, containing at least eight caldera volcanoes, some of them representing multiple caldera collapses (Figure 2.1: Cole et al., 1998; Wilson et al., 1995, 2009; Milicich et al., 2020). Taupo volcano is one of the two active rhyolitic volcanic centres in the TVZ (Wilson et al., 1995; Cole et al., 1998) producing 28 eruptions (labelled  $\Psi$ ,  $\Omega$ , A through Z), in the last 23 ka (Wilson, 1993; Barker et al., 2020). The youngest explosive eruption was the Taupo 232 CE eruption (eruption Y: Wilson, 1993) involving c. 35 km<sup>3</sup> of magma (see below) (Wilson & Walker, 1985; Wilson, 1993).

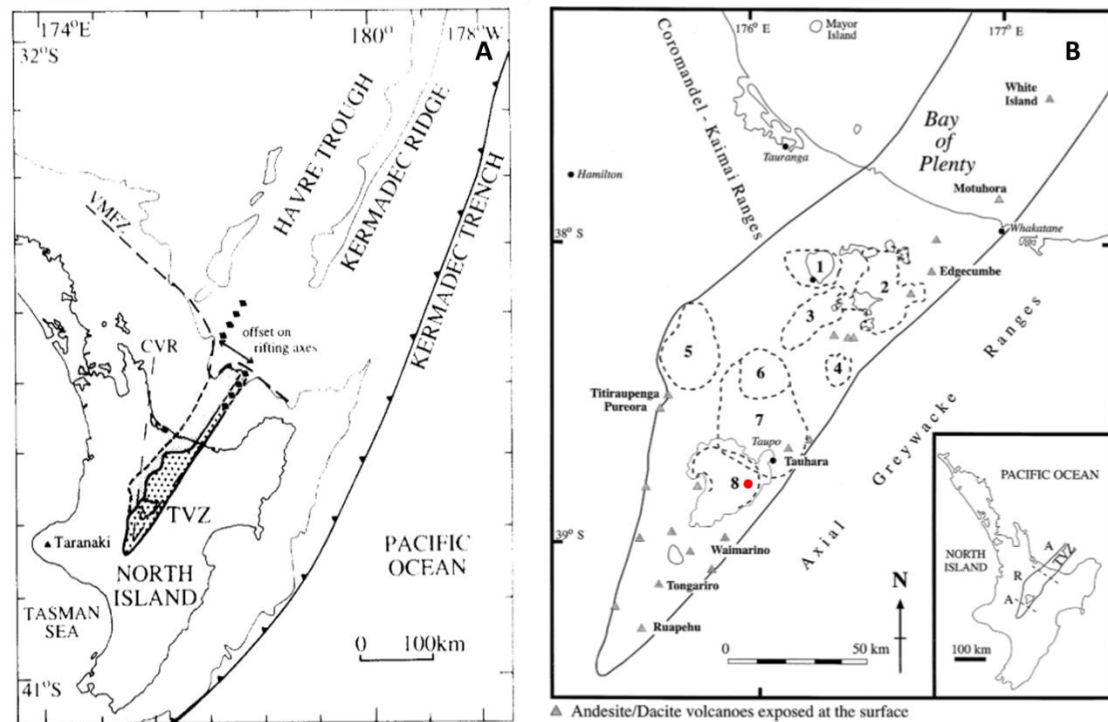


Figure 2.1 A) Map of the Hikurangi margin (Wilson et al., 1995); B) Map of the Taupo Volcanic Zone with known calderas indicated by dotted lines (modified by Cole et al., 1998) with red dot indicating vent position of the Taupo 232 CE eruption (Walker 1981a).

## 2.5 Taupo 232 CE Eruption

The Taupo 232 CE eruption is the youngest explosive event at Taupo volcano and occurred from multiple events from a lineation, now submerged in the north-eastern area of the lake, over which the Horomatangi Reefs and Waitahanui Bank (both related to the shortly later eruption Z) have since been constructed (Smith & Houghton, 1995; Houghton et al., 2010). The Taupo eruption (as originally conceived: Wilson & Walker, 1985) produced six explosive phases (labelled Y1-Y6) and one eruptive phase after a short hiatus (eruption Z of Wilson, 1993). The Y eruption produced three phreatomagmatic ash deposits (Y1, Y3, Y4), two plinian fall deposits (Y2, Y5), the latter accompanied by minor volumes of ignimbrite, and one exceptionally widespread ignimbrite (Y6) (Healy, 1964; Walker, 1980, 1981a,c; Walker et al., 1980, 1981; Froggatt, 1981; Froggatt et al., 1981; Wilson, 1985; Wilson & Walker, 1985; Wilson, 1993; Houghton et al., 2010, 2014; Mitchell et al., 2018).

Unit Y1 (Initial ash) was the first deposited phreatomagmatic ash, with a volume of  $0.015 \text{ km}^3$  and a plume height of  $<10 \text{ km}$  (Wilson & Walker, 1985; Houghton et al., 2010).

Y1 is narrowly dispersed on the eastern side of the lake reaching a maximum distance of c. 25 km from inferred vent and reaching a maximum thickness of 65 cm. Y1 is a uniformly fine grained, near white pumiceous ash deposit (Wilson & Walker, 1985; Nisbet, 2019). This deposit's upper boundary is marked by the coarse Y2 plinian fall pumices, reflecting the transition from a phreatoplinian style eruption to a Plinian style eruption. The boundary between Y1 and Y2 is important to note in this thesis (Sections, 4.1, 4.2 and 4.3).

Y2 (Hatepe Plinian Pumice) is the second eruptive phase, and the subject of this thesis. Y2 is a characteristically uniform, non-graded, well-sorted pumice fall deposit, produced by a 30 km high Plinian plume, discharging an estimated bulk volume of 2.3 to 6 km<sup>3</sup> (Walker, 1981a, b; Wilson & Walker, 1985; Wilson, 1993). This deposit reaches thicknesses of >2 m close to vent and is dispersed as far as the east coast of the North Island (c. 140 km) (Talbot, 1989; Wilson & Walker, 1985). Intraplinian ash beds have been identified in the northern section of this deposit and have been attributed to emplacement by rain flush and dilute gravity current mechanisms (Wilson & Walker, 1985; Talbot, 1989; Talbot et al., 1994) further detailed in Section 2.6.1.

The Y2 unit grades into the Y3 (Hatepe ash) phreatoplinian phase suggesting an influx of water into the vent. Unit Y3 is a 2.5 km<sup>3</sup> phreatoplinian deposit that reaches thicknesses of >2 m close to source. This deposit is pale grey, fine-ash-rich and poorly bedded, dominated by fine ash and highly vesicular pumice with minor amounts of wall-rock lithics (Walker, 1981c; Wilson & Walker, 1985; Smith, 1988; Houghton et al., 2010). Following a period of erosion, Y3 transitions into Y4 (Rotongaio Ash), a dark grey phreatomagmatic ash, with a volume of 1.3 km<sup>3</sup> (Wilson & Walker, 1985). Unit Y4 is an unusually fine-grained ash with poorly developed, fine-scale plane-bedding and a maximum thickness of 6 m (Wilson & Walker, 1985)

Following unit Y4 there is a marked change in eruption style to a vigorous Plinian phase (Y5). Unit Y5 (Taupo Plinian Pumice) is a large c. 23 km<sup>3</sup> (calculated by crystal concentration method: Walker, 1980) eruption with an estimated plume height of c. 50 km (although see Houghton et al., 2014), depositing coarse pumice interbedded with intraplinian ignimbrite flows (the Early Flow units) proximal to source (Walker, 1980; Wilson & Walker, 1985) Y5 differs from Y2 in its coarser grain size and its greater volume of intraplinian PDC deposits.

A drastic change in the eruption condition then led to production of a voluminous blast-like event that deposited the widespread ignimbrite unit Y6 (Taupo ignimbrite) (Wilson, 1985; Wilson & Walker, 1985). This deposit extends to c.  $80 \pm 10$  km from vent and has a bulk volume of c.  $30 \text{ km}^3$  (Wilson, 1985; Wilson & Walker, 1985). Following a hiatus of c. 10 years (Barker et al., 2016), magma was extruded onto the lake floor during eruption Z, forming the Horomatangi Reefs and Waitahanui Bank. Large pumiceous blocks of dome carapace material broke off these forming domes and floated to the lake surface then were wind-drifted to deposit on the edges of the contemporaneous lake to heights of 8 – 10 m above the modern level (Wilson & Walker, 1985; Von Lichten et al., 2016)

For the purposes of this study, particular focus is placed on the Hatepe Plinian Pumice (unit Y2) and its general characteristics (such as grain morphology and density) and emplacement mechanisms.

## **2.6 Y2 Deposit and its Characteristics**

Unit Y2 (Hatepe Plinian Pumice) deposit, the subject of this thesis, was produced by a ‘dry’ sustained, moderately powerful gas blast, producing a Plinian phase that lasted c. 10 – 30 hours (Walker, 1981a; Wilson & Walker, 1985; Houghton et al., 2003; Mitchell et al., 2018). Unit Y2 is characteristically a uniform, non-graded and well sorted pumice fall deposit, dominated by highly to extremely vesicular pumices that are low in crystal content (c. 3 wt %). The deposit also exhibits minor amounts of dense juvenile clasts (Wilson & Walker, 1985; Houghton & Wilson, 1989). Internal stratifications are seen and reflected by variations in grain size and vesicularity. The latter have been studied and show that the pumices textures range from sheared to equant shaped bubbles with minor coalescence, where lower density pumices display markedly less bubble deformation than higher density pumice (Ewart, 1963; Houghton & Wilson, 1989; Walker, 1981a; Houghton et al., 2010; Mitchell et al., 2018).

A vent position for the Y2 eruption has been identified and located by Walker (1981a) through the use of isopach and isopleth maps, off the eastern shore of Lake Taupo under an area that is now occupied by the Horomatangi Reefs (see below Figure, 2.1; Walker, 1981a; Smith & Houghton, 1995; Houghton et al., 2010). This Location was determined using grain sizes presented in the isopleth maps of maximum pumice and maximum lithic diameters



(Walker, 1981a). These maps show that the deposit dispersal axis is to the east (west-southwest prevailing wind) and shows exponential thinning with distance from vent towards the east coast of the North Island, reaching distances of >140 km (Walker, 1981a; Wilson & Walker, 1985; Talbot, 1989). The Y2 deposit becomes coarser and thicker towards Lake Taupo, but no ballistic lithics have been reported from available exposures, implying that the vent lies some distance (>3 km) beyond these exposures.

Isopach maps created by Walker (1981a) were used to calculate an initial eruptive volume of c. 2.3 km<sup>3</sup>. The method used analysed the deposit area within the outermost isopach line to estimate the thickness of the deposit at multiple intersections on a map grid. The thickness values were then averaged and multiplied by the “enclosed area” (Walker, 1981a). The mass for the deposit was obtained using the same isopach data and the volume was multiplied by the average bulk density. The bulk density for the Hatepe Plinian pumice was calculated as 0.5 g/cm<sup>3</sup> for near vent and 0.68 g/cm<sup>3</sup> for far-distal sections; the average was taken as 0.6 g/cm<sup>3</sup> therein yielding a mass of  $1.12 \times 10^{15}$  g (Walker, 1981a) on the basis of demonstrable fall material.

There are limitations in using this method, however, due to the significant amount of fines “lost” through atmospheric transport during the eruption and dispersed over the Pacific Ocean, although the exponential decay model does try to account for this “lost” material. To account for this fines loss, Walker (1980) proposed an alternative method, termed the crystal concentration method, to re-calculate the eruptive volume, giving a value of 6 km<sup>3</sup> (Walker, 1981a). In the Walker (1980) method it is noted that crystal abundances at any given point in the deposit vary due to the free crystals (crystals released when magma is fragmented) being preferentially deposited from the eruptive cloud closer to the vent. The following assumptions for this method are made:

1. The same percentage of lithics (juvenile and foreign) are also “lost”, equating to a loss of c. 17%. Using the same bulk density these values are added to the on-land values in order to obtain the total volume; previously noted as 6 km<sup>3</sup>;
2. Pumice is representative of the “original magma”;
3. The free crystal content within the deposit is not representative of that of the crystals within the pumice. Crystals are freed when during the eruption, magma is fragmented

and large phenocrysts segregate from pumice and ash fragments. It is also noted that the size of free crystals is equal to or finer than the largest phenocryst (2 mm sieve fraction; Walker, 1980, 1981a).

Walker (1981a) reported a crystal weight percentage of 3.3 wt %. From this, the mass of the deposit was re-calculated, giving a value of 6 km<sup>3</sup>, using calculations outlined in Walker, (1981a).

### **2.6.1 Ash Beds within the Y2**

Talbot (1988) and Talbot et al. (1994) expanded on Walker's (1981a) field observations with the documentation of several poorly sorted, ash-rich beds within the Y2 fall deposit northeast of Lake Taupo. These beds were separated into three groups (A, B, and C) and were predominantly observed north of the main dispersal axis. Group A consists of two ash beds (A1 and A2) with a maximum cumulative thickness of 13 cm, deposited up to 45 km to the north-east of vent and covering an area of 290 km<sup>2</sup> (Figure, 2.2a). They are fine-grained, massive, and vesiculated beds (Lorenz, 1970, 1974; Walker, 1971; Talbot et al., 1994) which lack accretionary lapilli, erosive bases, grading, cross-bedding or gas escape pipes (Talbot et al., 1994). In southern sections the group A beds are separated by a thin fall lapilli layer labelled as Group B (Figure, 2.2b). Group C beds range in ash content and contain up to 7 beds (Talbot et al., 1994) reaching a cumulative thickness of 35 cm. The thickness and number of beds vary in relation to distance from the vent (Figure, 2.2c). Each of these groups were proposed by Talbot et al (1994) to be emplaced by varying processes, as follows:

- Group A: emplaced very rapidly, indicated by lack of cross bedding, and interpreted as dilute gravity currents produced from the collapse of the outer margins of the Plinian plume;
- Group B: fall lapilli deposited synchronously with Group A; where Group B is present, it occurs between A1 and A2;

Group C: attributed to deposition by rain-flushing. Group C beds exhibit poor sorting compared to Groups A and B through the incorporation of finer ash and coarser pumice lapilli. Most localities contain one or two Group C beds, this decreases to only one near vent.

It was noted that deposits of Group A and B thin with distance from the vent and are can be correlated throughout Y2 exposures. Group C deposits vary greatly in thickness as they were inferred to have been controlled by atmospheric conditions (rain and wind) as rain showers flushed ash from the buoyant eruption plume causing it to fall in aggregates.

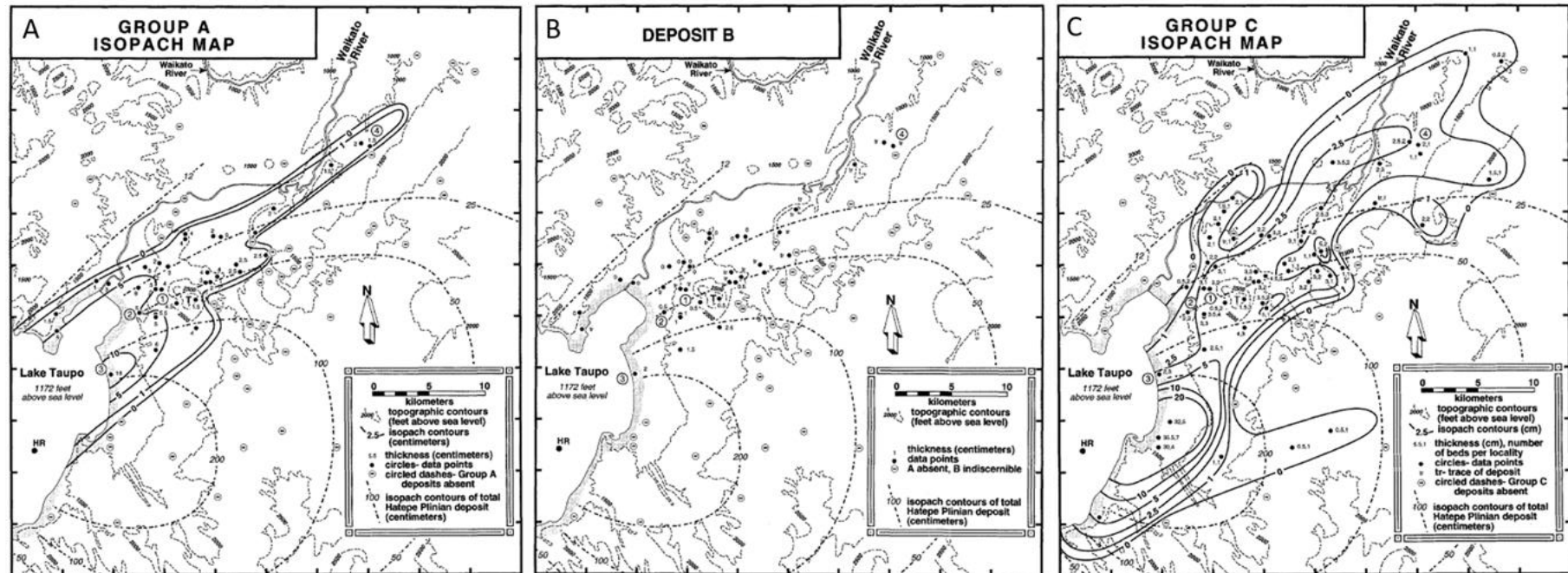


Figure 2.2 Distribution maps of ash beds within the Y2 eruption produced by Talbot et al. (1994). A) Isopach map of the Group A beds, B) Locations Deposit B was identified, C) Isopach map of the Group C beds.

### 3 Methodology

The data suite presented in Chapter 5 has been produced in the field and laboratory from the Taupo 232 CE Hatepe plinian (Y2) deposit. Observations were made in the field, recording general grain size properties (using grainsizes presented in Table, 3.1) changes in lithological characteristics, layers visible in the deposit, boundary characteristics and thicknesses. Field sketches, vertical logs and photos were taken at each site.

Table 3.1 Tephra size classes in relation to grain size (phi and mm; Thordarson, 1990)

Grain Size ( $\phi$ )	Grain Size (mm)	Tephra Size Class
< -6	> 64	Blocks and Bombs
-5 – -6	32 – 64	Coarse Lapilli
-4 – -5	16 – 32	Medium Lapilli
-1 – -4	2 – 16	Fine Lapilli
0 – -1	1 – 2	Coarse Ash
4 – -0	0.064 – 1	Medium Ash
> 4	> 0.064	Fine Ash

#### 3.1 Reconnaissance Mapping

Reconnaissance mapping was conducted in order to acquire field stratigraphic sections to sample, analyze and explain the complex stratigraphy within the Y2 deposits. These units were selected after scouting approximately 1,370 km<sup>2</sup> of the main deposit area, bounded between the eastern edge of the lake and the western edge of the Axial Ranges (see below Figure 4.1). The units described in full detail in Section 4 were selected so as to form two transects, one proximal to medial along the plume dispersal axis, and one lateral: perpendicular to the plume dispersal axis.

The Hatepe plinian deposit was mapped extensively by Walker (1981) to produce a set of isopach and isopleth maps. The isopach data was taken into consideration when scouting and picking the best places to search for exposures to be able to construct downwind and crosswind sections. A total of eight sections are described in this thesis, all of which were

sampled. Of these twelve, four have been extensively sampled and are the main source of data discussed in this thesis.

### **3.1.1 Identification of Key Sections for Downwind Variations**

Key sections on the downwind transect (see below Figure, 4.1) were selected on the basis that they were as close to the dispersal axis as possible, easily accessible, had no visible slumping or tilting of the deposits, and the upper and lower layer boundaries were visible. These localities were ordered from the most proximal section closest to the inferred vent location proposed by Walker (1981a) to the most medial section furthest from the vent in line with the dispersal axis, following the proposed downwind transect direction.

### **3.1.2 Identification of Key Sections for Cross Wind Variations**

The identification of sections for the crosswind profiles differs from those outlined above as these were selected to generate profiles in a line perpendicular to the deposit's main dispersal axis (see below Figure, 4.1). These sections were selected using the same criteria as the downwind transect sections.

## **3.2 Sampling Procedures**

### **3.2.1 Box Sampling**

Samples taken at the following sections (Table 3.2) were sampled using a top down box sampling method, where the upper layers were sampled first in attempts to minimise the degree of contamination from collapsing material.

This sampling method was used for the outcrops that demonstrated variation in the units. These samples were chosen based on the macroscopic bedding characteristics, i.e. ash beds, coarser beds, lithic layers, etc.

### **3.2.2 Incremental Sampling**

The following localities have been sampled incrementally, in 2 cm portions successively from the top downwards (Table 3.3.). This method was utilized for the exposures that lacked discernable variations in components and grain size to the naked eye.

Table 3.2 List of localities where box samples were taken.

Locality Name/ Number	Latitude (S) WGS84	Longitude (E) WGS84	UTM 60S (X)	UTM 60S (Y)
Waitahanui (1)	S 38°48'03.6"	E 176°04'38.0"	419870	5704903
Waimahia (5)	S 38 ° 49' 36.5 "	E 176 ° 8' 37.9 "	425685	5702095
Bypass Ash (6)	S 38°42'41.9"	E 176°06'35.5"	422609	5714846
Rotokawa (8)	S 38°38'23.1"	E176°11'38.5"	429857	5722891
Aaron's Farm (7)	S 38 ° 42' 57.7 "	E 176 ° 13' 21.9 "	432428	5714449
Type Section (2)	S 38°44'51.0"	E 176°11'58.9"	430455	5710938

Table 3.3 List of localities where incremental samples were taken.

Locality Name	Latitude (S) WGS84	Longitude (E) WGS84	UTM 60S (X)	UTM 60S (Y)
SH5 Hill (3)	S 38°54'27.4"	E 176°26'57.4"	452249.9	5693332
SH5 Ranges (4)	S 38°55'44.6"	E 176°29'09.3"	455440.1	5690971

## 3.3 Laboratory Work

Samples from Locations 2, 3, 5 and 8 were processed using the following techniques to acquire grain size and componentry on all samples. Textural and density analyses were also performed on selected samples.

### 3.3.1 Grain Size Analysis

Grain size analysis used a combination of wet sieving, dry sieving and laser particle analysis to attain the overall grain size distributions. These individual processes are outlined below.

#### Wet Sieving

Wet sieving is used prior to dry sieving analysis on samples containing an ash content of c. >10% ash (<250 µm) to reduce the risk of ash becoming airborne and reduce the risk of manual generation of fines. The sample was passed through a stack of mesh sieves over a large container. using reverse osmosis water. Sieves are arranged in decreasing order of

aperture size, with a maximum of -2 phi and a minimum of 2 phi. Phi increments were originally defined by Krumbein (1934, 1938) and are presented in Table 3.4. When water runs clear through the sieve, the >250 µm fraction was transferred to a container and dried at c. 80 °C prior to dry sieving, whilst the <250 µm fraction was left for a week to settle until water was clear. The water was then drained and the <250 µm fraction was dried, labelled and weighed and analysed by use of the laser particle analyser (described below).

*Table 3.4 List of sieve mesh sizes (phi and mm)*

Sieve mesh size (φ)	Sieve mesh size (mm)	Sieve mesh size (φ)	Sieve mesh size (mm)
<b>-6</b>	64	<b>-1.5</b>	2.8
<b>-5.5</b>	44.8	<b>-1</b>	2
<b>-5</b>	31.5	<b>-0.5</b>	1.4
<b>-4.5</b>	22.4	<b>0</b>	1
<b>-4</b>	16	<b>0.5</b>	0.710
<b>-3.5</b>	11.2	<b>1.0</b>	0.500
<b>-3</b>	8	<b>1.5</b>	0.355
<b>-2.5</b>	5.6	<b>2.0</b>	0.250
<b>-2</b>	4		

### Dry Sieving

Dry sieving was used for the coarse fraction (>250 µm) of all samples. A series of mesh sieves in decreasing order of aperture size by half phi increments (max -5.5 phi and min 2 phi) were stacked on top of a catching dish. Samples were carefully brushed through the stack ensuring material fell through to the appropriate size fraction, where the grains intercepted by each sieve size is controlled by the intermediate axis for the grains. The material in each sieve size were labelled, bagged and weighed (Blott & Pye, 2001) including that in catching container (<250 µm). For samples that were originally wet sieved, the <250 µm fractions were added together and reweighed.

The <250 µm fractions of all samples were split using dry split using a riffle splitter in order to get a smaller representative sample prior to analysis on the laser particle analyser. Representative samples used weighed between 10 mg and 10 g, depending on the coarseness of the sample.



## Laser Particle Analysis

The <250 µm fractions of all sample were analysed using the Horiba Partica LA 950V2 Laser Scattering Particle Size Distribution Analyser: LPA or PSDA. This instrument uses lasers to measure particle sizes from 3000 µm to 0.01 µm. In order to measure such a range in particle sizes, two light wavelengths are used. A long wavelength is used to measure coarse particles and a short wavelength to measure smaller particles. Due to volcanic ashes, particularly rhyolites, having a unique makeup as opposed to other ashes or sediments, the samples were analysed using the Fraunhofer method. These samples were analysed using the slurry sampler and dry feeding method. Coarseness of the sample is a factor here as well; if the sample is coarse the amount of sample put into the machine will be greater than a sample with finer particles. Each subunit sample was analysed 4 times to get a representative distribution and was then averaged.

## Gradistat Calculations

The weight percentages of sieved data and the averaged LPA data for each sample was consolidated using software from a compilation program (Pers comm; E. Brosch, 20/10/2019) and inserted into the Gradistat program (Blott & Pye, 2001). Gradistat gives an overall grain size distribution and the relevant descriptive statistics used in this study in both geometric and logarithmic scale. The grain size statistics are based on those proposed by Folk & Ward (1957), and only the logarithmic statistics were used in this study i.e:

Graphic mean (Folk & Ward, 1957):

$$M_z = \frac{\phi_{16} + \phi_{50} + \phi_{84}}{3}, \quad (\text{Eqn. 1})$$

Graphic standard deviation (Folk & Ward, 1957):

$$\sigma_1 = \frac{\phi_{84} - \phi_{16}}{4} + \frac{\phi_{95} - \phi_5}{6.6}, \quad (\text{Eqn. 2})$$

Median =  $\phi_{50}$

Mode(s) = Most frequently occurring grain size or grainsizes, representing a range from the sieve size that retained the most weight to the phi of the next larger sieve.

### 3.3.2 Componentry Analysis

Throughout this study the ratios of juvenile to foreign components are of great interest to help interpret the nature of the vent and the eruption dynamics. In order to make these interpretations detailed componentry analysis was undertaken.

Following the completion of grain size analysis, the full and the above half phi grain size fractions needed to be combined (Table 3.5). The components within each full phi size fraction were then identified and separated into the groups outlined in Table 3.6 (see results Section 4.3 for component images). To obtain the componentry across the full range of grain sizes, samples from Location 8 were analysed for all components within all full phi grain size bins. Location 2 and 5 were used as comparative sections, where selected grainsizes -2 phi and 1 phi were analysed.

The coarse fraction was dependent on the abundance of clasts in the  $-2\phi$  size in each subunit. Size classes coarser than  $-2\phi$  generally had less than the 300 grains required to be fully representative of the layer's componentry. The  $1\phi$  size fraction was chosen as a representative size for the fine fraction and was easier to analyse under a binocular microscope than the  $2\phi$  size fraction. A minimum of c. 300 grains and a maximum of c. 2000 grains were counted from each size fraction to provide a representative componentry count due to the absence of change in componentry variations after 300 grains. Samples containing more than c. 300 grains were evenly split using a riffle splitter to obtain a minimum of 300 individual grains.

*Table 3.5 Combined half and full grain size fractions used for componentry analysis.*

Combination ( $\phi$ )	Combination (mm)	Resulting full $\phi$ class
-5.5 + -5	44.8 + 31.5	-5
-4.5 + -4	22.4 + 16	-4
-3.5 + -3	11.2 + 8	-3
-2.5 + -2	5.6 + 4	-2
-1.5 + -1	2.8 + 2	-1
-0.5 + 0	1.4 + 1	0
0.5 + 1	0.710 + 0.500	1
1.5 + 2	0.355 + 0.250	2

Table 3.6 Table of component classes and their descriptions.

Component Class	Visual Estimated Vesicularity (%)	Colour	Composition/ Description
C1 Dense Juvenile Pumice	>40	White/pale cream	Clasts are rhyolites, little discolouration, vesicles are mostly small and rounded ranging in size from microns to tens of microns.
C2 Vesicular Juvenile Pumice	>40	White/pale cream	Very vesiculated, vesicle size and shape range from round to elongated, tens to hundreds of microns, appear glassier than C1, no weathering
C2* Vesicular Juvenile Pumice *	<40	White/pale cream	Thick bubble walled pumices ranging from fibrous to equant, glassy surfaces, transparent in colour. Some have spherical bubbles equant in shape, round vesicles.
C3 Grey Juvenile Pumice	>20	Light to medium grey	Range from glassy grey rhyolites/grey microlitic rhyolites to foamy grey rhyolites.
C4 Dense Juvenile Rhyolites (Banded Pumices)	~10 – 20	Banded grey and black	Dense juvenile rhyolites, banded black grey or dark/light grey. Bands of white vesiculated pumice and bands of dense glass are observed.
C5 Obsidian	0 – 5	Smokey brown, grey, black, bottle brown	Dense glass, very little vesiculation, crisp/shiny/sharp edges and surfaces, no ash coating, angular, conchoidal fractures.
C6 Foreign Lithic 'Shallow' (cf. below section 7.2)	-	Pink, grey, orange, brown, light green.	Shallow lavas, foreign rounded obsidian, volcanic breccias and ignimbrite fragments, hydrothermally altered, green pumices.
C6 Foreign Lithic 'Intermediate' (cf. below section 7.2)	-	Light to deep creams, grey	Sedimentary rocks, grey lacustrine sediments, hydrothermally altered sandstone
C6 Foreign Lithic 'Deep' (cf. below section 7.2)	-	White, grey,	Plutonic material, generally fractured, contains abundant small black and orange crystals in a fine white crystal matrix.
C7 Crystals	-	Black, green, transparent	Foreign (xenocrysts) and juvenile (phenocrysts). Plagioclase, Fe-Ti, Pyroxene,

Macroscopic features of componentry classes C1 – C7. Vesicularity percentages have been estimated visually

### **3.3.3 Thin Section and SEM Imaging**

#### **Thin Section Preparation**

Thin-section grain mounts were prepared from the  $-2\phi$  size fraction in order to look at the macroscopic textures of selected juvenile and non-juvenile clasts under a petrographic microscope and a Scanning Electron Microscope (SEM: Section 4.3.1.) to gain insights into the fragmentation, expansion and cooling processes. Seven grains from component class C1, ten grains from C2, five grains from C3, four grains from C4 and three grains from C5 were selected to be representative of the range in textures from each juvenile class. Three representative grains from each lithic class were also prepared using the following method for analysis under the petrographic microscope.

Samples were primarily impregnated in low viscosity epoxy (Epotek 301) under vacuum (0.2 bar in the Struers CitoVac) for 4 hours and left to cure for a further 24 hours. Impregnated samples were then prepared for mounting. The samples were sliced on one side and polished using grit powder down to 800 grit. This surface was then impregnated with a small amount of epoxy under vacuum (0.2 bar) and left to cure. The excess epoxy was then removed using grit powder up to 1000 grit. The cut surface of the clast was then mounted on a thin section slide with a ground surface using epoxy and placed on a hotplate heated to 70°C. These were left to cure for 24 hours before the grain was thinned to 30 $\mu$ m using 800 to 1600 grit powder and polished using 1  $\mu$ m diamond paste. Each grain was prepared using the above method in preparation for analysis on the SEM. Following preparation, the samples were carbon coated using a BAL-TEC SCD sample coater/sputter coater, prior to being photographed in the SEM.

#### **SEM Imaging**

A FEI Quanta 200 Environmental SEM with EDAX module was used to acquire backscattered electron images of microscopic textures of the juvenile pumice and dense juvenile classes that were mounted on to thin sections. The instrument was operated with an accelerating voltage of 20 kV with a beam of 3  $\mu$ m, where the sample stage height was set at an operating distance of 10 mm. Using the imaging function, photos were taken in greyscale backscatter mode of the entire grain at the same magnification. The zoom magnification function was used to take closer images of selected interesting features within

grains. Special features were characterised based on changes in the bubble morphology, sections of excess fracturing or shearing, etc.

### **3.3.4 Density Measurements**

The  $-2\phi$  size fraction was used for all the juvenile classes from Location 2 using the upper samples 1 and 2A to analyse their density. The instrument used to process these samples was the GeoPyc 1360 Envelope Density analyzer in order to obtain density measurements of porous grains larger than 2 mm, particularly those of irregular size and shape. This instrument is equipped a cylindrical tube attached to a revolving plate on each end. A single grain from the sample is embedded in a cylinder half filled with the dry flo powder. As the plates compress the powder compacts around the grain and records the displacement into a density measurement.

### **3.3.5 Methodology Limitations**

Throughout the course of field and laboratory work the following limitation was encountered:

- During thin section preparation, the thin sections were cleaned in an ultrasonic bath between polishing stages. As a result, some of the grains that were mounted on the slide peeled off, limiting the number of grains able to be used for textual analysis. This meant that the number of grains from each of the juvenile pumice classes were unequal, and thus may not be fully representative of the juvenile pumice textures.

## 4 Results

### 4.1 Stratigraphic Profiles of Y2 and Their Downwind and Crosswind Variations

To examine vertical and lateral facies variation within the Y2 Plinian deposit, macroscopic field observations on vertical variations in grain-size, based on a visual estimate of maximum grainsize, using size ranges outlined in Table, 3.1, and componentry were documented for locations aligning roughly parallel and perpendicular to the deposit axis (Figure, 4.1).

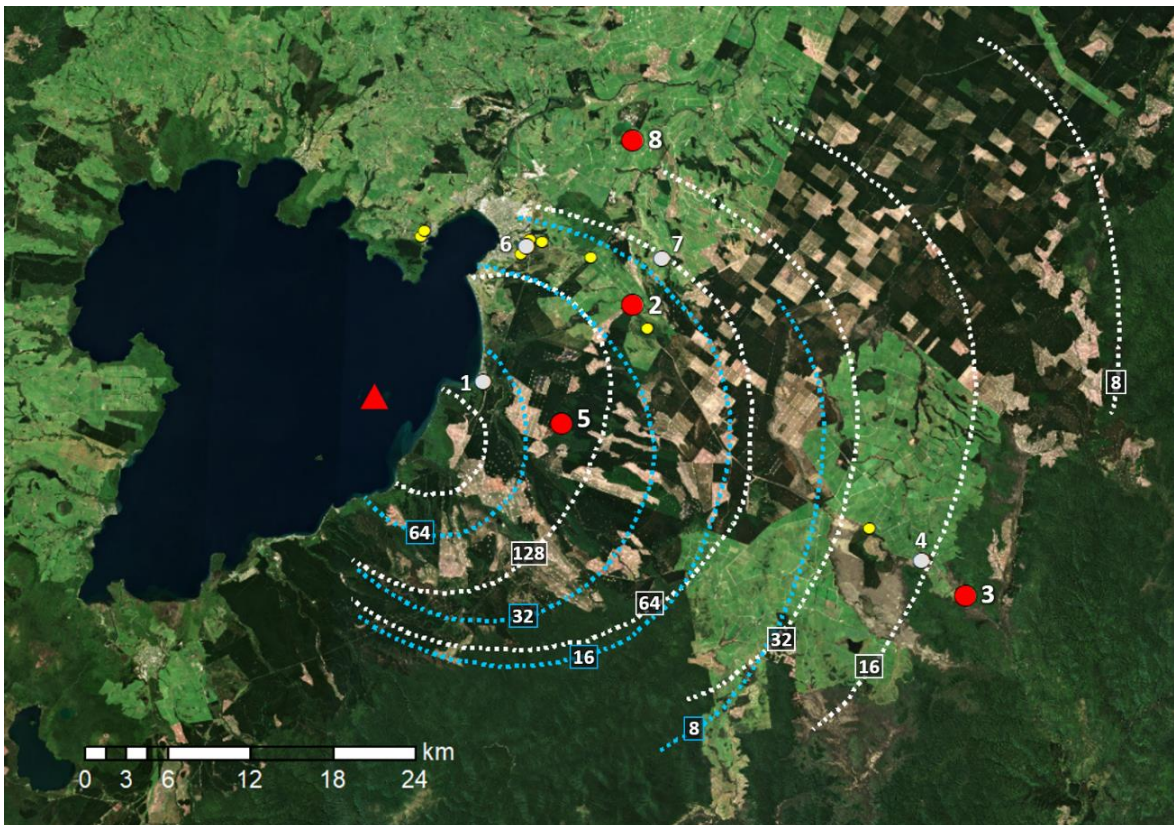


*Figure 4.1 ArcGIS Map displaying field localities (numbers corresponding to Tables, 3.2 and 3.3); red dots are localities processed with laboratory analysis and discussed in the results; grey dots are localities sampled but not processed; yellow dots are localities documented during field work. The red triangle indicates inferred vent position (Walker, 1981a); dotted blue and white lines indicate isopleth boundaries for maximum lithic and pumice sizes, respectively (sizes in cm indicated in black boxes; modified from Walker, 1981a).*

The deposit characteristics for locations parallel to deposit axis are as follows:

*Location 1* on SH1 (S 38°48'03.6", E 176°04'38.0") is the most proximal of the studied locations, at a radial distance of 8 km from inferred vent position (Figure, 4.1; Walker, 1981a) and where Y2 has a thickness of 223 cm. Here, Y2 is predominantly a massive, reverse-graded pumice-dominated, poorly sorted, very coarse lapilli bed (see Appendix, 1; Location 1), with a 3.5 cm lithic rich, coarse lapilli layer at its base, resting with a sharp contact on Y1. The upper boundary with Y3 is also sharp. The lower 1/3 of Y2 has 6 ash rich layers (4.5, 5, 8, 5, 3 and 4 cm thick, from base to top, respectively: Figure, 4.2) intercalated with the lapilli-rich material, but these are absent from the upper 2/3 of the unit. The ash intercalations are all similar, poorly sorted, massive, fine ash with admixed coarse-to-very coarse lapilli pumice. These ash beds correlate, respectively, to samples 3, 5, 7, 9, 11 and 13 in Appendix, 1; Location1.

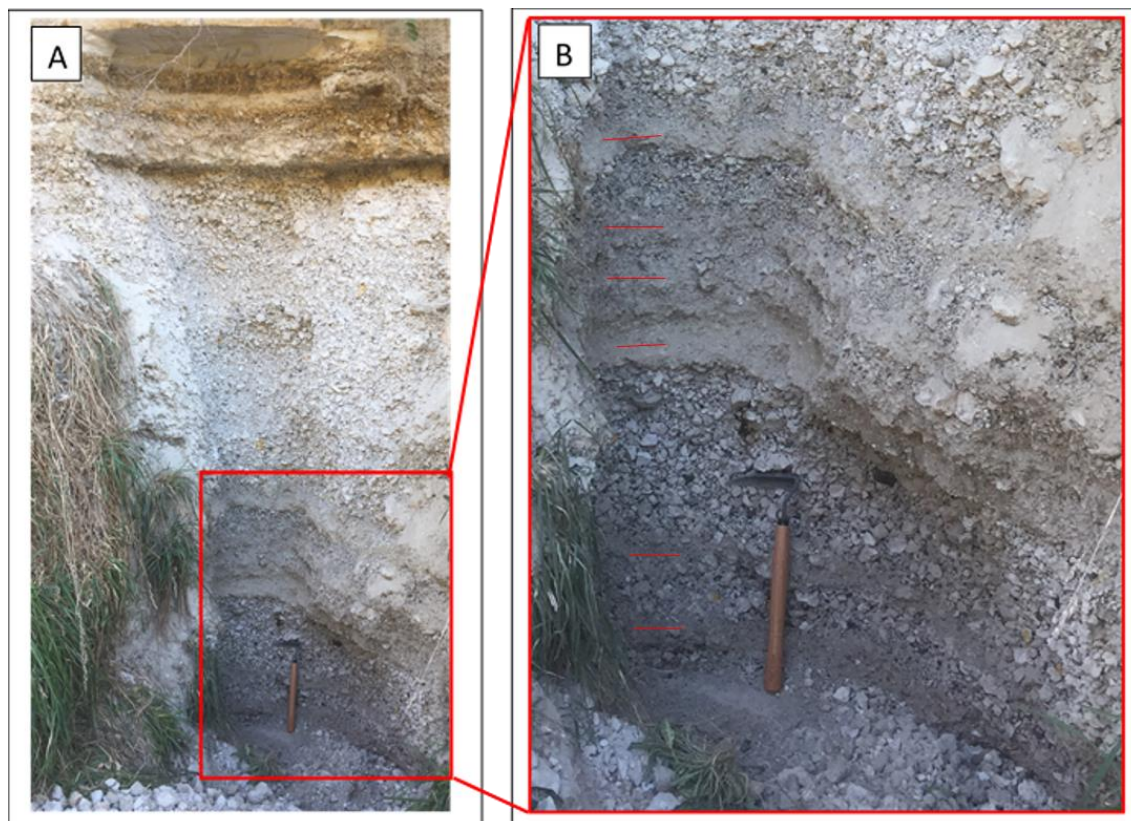


*Figure 4.2 Photograph of Location 1 outcrop with focus on intraplinian ash beds, scraping tool for scale. A) Full outcrop B) Inset showing intraplinian ash deposits marked by red lines with thickness of 4.5, 5, 8, 5, 3, and 4 cm from base to top, respectively.*

*Location 2* is on SH5 (S 38°44'51.0" E 176°11'58.9") at a radial distance of 20 km from vent. All Taupo 232CE eruptive units are observed at this location where Y1 is at the edge of its dispersal limit and is sharply overlain by Y2 which has a thickness of 146 cm, with a sharp upper contact into unit Y3, and is a moderately to poorly sorted, mostly massive, pumice-dominated medium lapilli unit (Appendix, 1; Location 2). However, in the upper 60 % of the unit, and above a distinctive 3 cm lithic-rich, moderately sorted, medium lapilli layer, Y2 shows a general reverse coarse tail grading. While this profile does not contain any pronounced ash beds or bedding structures, weak and laterally continuous banding occurs at several heights. These bands are associated with subtle local fining and coarsening over thickness intervals of several centimetres (Figure, 4.3).

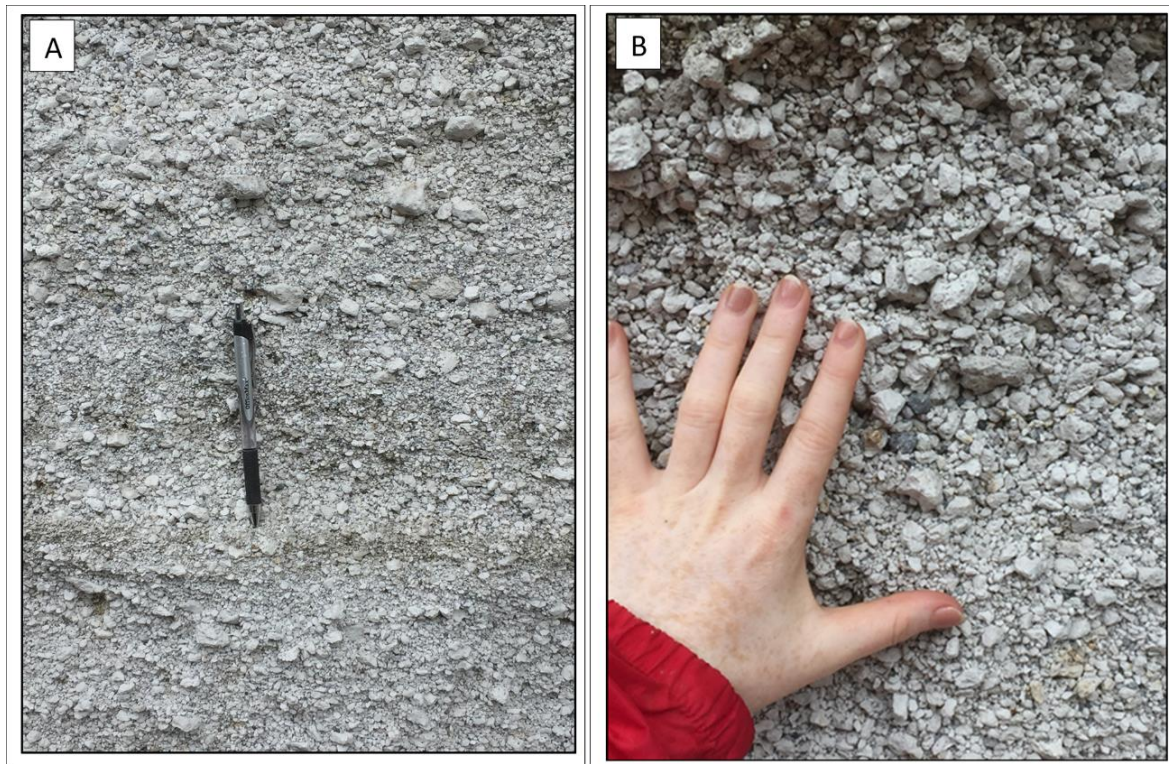


*Figure 4.3 Photographs of A) Weak coarser-finer banding seen in the middle to top portion of Location 2, pen as scale; B) The general reverse coarse tail grading seen in the top portion of Location 2, hand as scale.*

*Location 3* (S 38°54'27.4" E 176°26'57.4") is located on SH5 at a radial distance of 41 km from vent. Above an undulating contact on a dark grey paleosol (unit Y1 was not deposited to this distance), unit Y2 has a thickness of 31 cm, while the upper contact to the 26 cm thick unit Y3 is gradual over ~ 1 cm. At this location, Y2 is generally a moderately to well sorted, massive, pumice-dominated, fine to very fine lapilli (Appendix, 1; Location 3). The Y2 bed



at this location is characterised by a coarse tail reverse grading up to 16 cm above base, where the coarsest pumices occur, then a normal grading trend to the upper contact. Evidence of this cyclic grading is further explained in Section 4.2.1

*Location 4* on SH5 (S 38°55'44.6" E 176°29'09.3"), is the most distal location studied, at a radial distance of 45 km from vent. All Taupo 232 CE eruptive units except Y1 are seen here (Y6 >10 m, Y5 ~40 cm, Y4 ~2 cm, Y3 ~32-35 cm, Y2 ~24 cm). Here, unit Y2 is 24 cm thick, and is a well-sorted, massive, pumice-dominated, fine lapilli to coarse ash unit (Appendix, 1; Location 4), resting with an undulating contact on a dark grey paleosol, and with a gradual upper boundary to Y3. This Y2 location lacks ash beds and shows no obvious grading. The upper 2 cm of Y2 is finer grained towards the Y2-Y3 contact where the transition is gradual.

The following descriptions are the field characteristics for the locations (including Location 2: Figure, 4.1) aligned approximately perpendicular to the deposit axis direction.

*Location 5* is on Rotoakui Road (Kaingaroa Forest: S 38°49'36.5", E 176°08'37.9") at a radial distance of 14 km from vent. Unit Y2 here is a moderately sorted, predominantly massive, pumice-dominated coarse lapilli unit with a thickness of 234 cm (Appendix, 1; Location 5). At the base, it has an undulating contact on unit Y1 and is sharply bounded at the top by unit Y3. The lowest lapilli layer (refer to Appendix, 1; Location 5) is a lithic rich, moderately sorted, massive, pumice-dominated coarse lapilli. There is a 1 cm-thick bimodal ash rich bed 21.5 cm from the base of Y2 that is a poorly to very poorly sorted, massive, fine to very fine ash with coarse lapilli pumice (refer to Section 4.2.1).

*Location 6* is located on the SH1 Taupo Bypass road (S 38°42'41.9" E 176°06'35.5") at a radial distance of 16 km from vent. Above an undulating contact on a dark grey paleosol (Y1 is absent), Y2 has a thickness of 56 cm, with a sharp upper contact with Y3. Y2 contains both fall lapilli beds and ash rich beds (Appendix, 1; Location 6). The lapilli beds form the upper 2/3 of the unit and are moderately sorted, massive, pumice-dominated medium-to-fine lapilli units. The lower 1/3 of the unit contains a series of three ash beds intercalated with the lapilli material (Chapter 4.2). The uppermost ash beds with thicknesses of 4 cm and 5 cm (sample numbers 4 and 6, respectively) are moderately sorted, massive, fine ash-rich beds that contain fine lapilli pumices (Figure 4.4). The lowermost ash bed (sample 8) is a 7 cm-thick, well-sorted, massive, fine to medium ash bed.



*Figure 4.4 A) Photograph of Location 6 outcrop with ash beds 5 and 7 outlined in red, which are separated by a lapilli fall, scraper for scale. B) Zoomed in photograph of beds 5 (upper ash), 6 (middle lapilli), and 7 (lower ash).*

*Location 7* is located on the Wairakei Farms Estate land, in the former Tauhara, Forest (S 38°42'57.69" E 176°13'21.904") at a radial distance of 23 km from vent. Above a sharp contact on a dark grey paleosol, unit Y2 is 34 cm thick and is sharply overlain by unit Y3. Y2 is a well-to-moderately sorted, massive, pumice-dominated, medium lapilli fall deposit (Appendix, 1; Location 7) with an overall normal grading. The base of Y2 here has a 3 cm thick, poorly sorted, massive, coarse ash that contains coarse lapilli pumice.

*Location 8* is located on Broadlands Road (S 38°38'23.1" E 176°11'38.5") at a radial distance of 23 km from vent. Above an undulating contact on a dark grey paleosol, unit Y2 has a thickness of 19 cm and has undulating upper contact with unit Y3. This unit Y2 section contains alternations of ash-rich beds bounded by coarser lapilli-rich beds (Appendix, 1; Location 8). The lapilli beds are generally moderately sorted, massive, pumice-dominated medium to coarse lapilli units. The middle to upper portion of unit Y2 contains four ash beds that have thicknesses of 1.3, 0.7, 0.6 and 2.3 cm (samples 3, 5, 7 and 9, respectively; Figure, 4.5). The uppermost three of these ash beds show an overall poor sorting and are massive, medium-coarse ash with medium-to-coarse lapilli pumices. The lowermost ash bed is a well sorted, massive fine-medium ash bed. These beds have previously been identified and described by Talbot et al. (1994).



Figure 4.5. A) Photograph of Location 8 outcrop. Red boxes are insets of: (B) upper ash beds, and (C) lower ash bed.

## 4.2 Grain Size Distributions

### 4.2.1 Vertical and Lateral Grainsize Variation

In order to characterize vertical (representing relative time) and lateral (downwind and crosswind) variations in the Y2 deposit, continuous vertical samples were obtained for grainsize (and componentry) analyses from four Locations (2, 3, 5 and 8). Due to the dominantly monotonous character of the lapilli-dominated deposits, these samples were taken as box samples at approximately constant height intervals in such a way as to yield around ten samples per location. The exceptions to this constant-thickness-sampling procedure are the ash-rich layers, which were box-sampled from their top to bottom contacts. In the following descriptions, downwind variations in grainsize are described with data from Locations 5 (14 km from vent) and 3 (41 km from vent). These two locations are approximately aligned with the main dispersal direction, as estimated from existing isopach data (Figure, 4.1; Walker, 1981a). Crosswind variations in grainsize are examined using data from Locations 5 (14 km from vent), 2 (20 km from vent) and 8 (26 km from vent), oriented approximately perpendicular to the main dispersal axis of unit Y2.

## Grain Size Distributions

The characteristics and vertical variations in grainsize histograms of the vertical profiles of Locations 5, 2, 3 and 8 are shown in Figure, 4.6. These histograms can be subdivided into two main groups. The first, and most abundant, group 1 constitutes poorly to well-sorted lapilli to coarse ash-dominated distributions. These are characterized by a (mostly) unimodal and approximately symmetrical coarse-tail part, and a long fine-tail part that extends to c. 8 phi (4 microns). Coarser and finer-grained varieties of group 1 have main modes that range from 16 mm to 1 mm, while their contents of very fine ash (<63 microns) vary from 8 wt % to 0.1 wt %. The second (group 2) constitutes ash-rich fine lapilli and lapilli-bearing ashes, with very poorly sorted and strongly bimodal grainsize distributions. Accordingly, their main modes can either occur in the lapilli sizes (such as Location 5, sample 8) or in the ash sizes (Location 8, with samples 5 and 9 being medium- and very fine-ash varieties). Group 2 samples were recovered only from the lowermost part of the proximal Location 5 (samples 8 and 10) and throughout Location 8 situated at the northern margin of the Y2 dispersal. Samples of Locations 2 and 3 are entirely of group 1 (note that sample '0 cm' of Location 3 is contaminated by the underlying soil).

## Mean Grainsize Versus Sorting

The subdivision of the Y2 samples of the four locations into two distinct grainsize distribution groups is also well displayed in a mean particle diameter versus sorting coefficient graph (Figure, 4.7a). As explained in chapter 3.3.1, the grain size parameters of Folk & Ward (1957) are used in this thesis to allow comparison to previous analysis by Walker (1981a). In this graph, group 1 samples are characterized by sorting coefficients lower than c. 2.2 phi and mean diameters larger than 1.5 phi. They show a pronounced pattern of improving sorting (smaller values for standard deviation) with decreasing mean particle size. This trend is also a clear function of the radial distance from vent of the locations, with proximal Location 5 having the coarsest and most poorly sorted lapilli samples and distal Location 3 displaying the most fine-grained and best-sorted lapilli samples. There are systematic changes in grainsize distributions associated with this proximal to distal trend, for example, see Figure, 4.7b–d for mid-unit samples of Locations 5, 2 and 3. With radial distance from vent, the coarse-tail modes of the histograms become increasingly narrower and perfectly unimodal (better sorted), while the main mode decreases (finer grained).

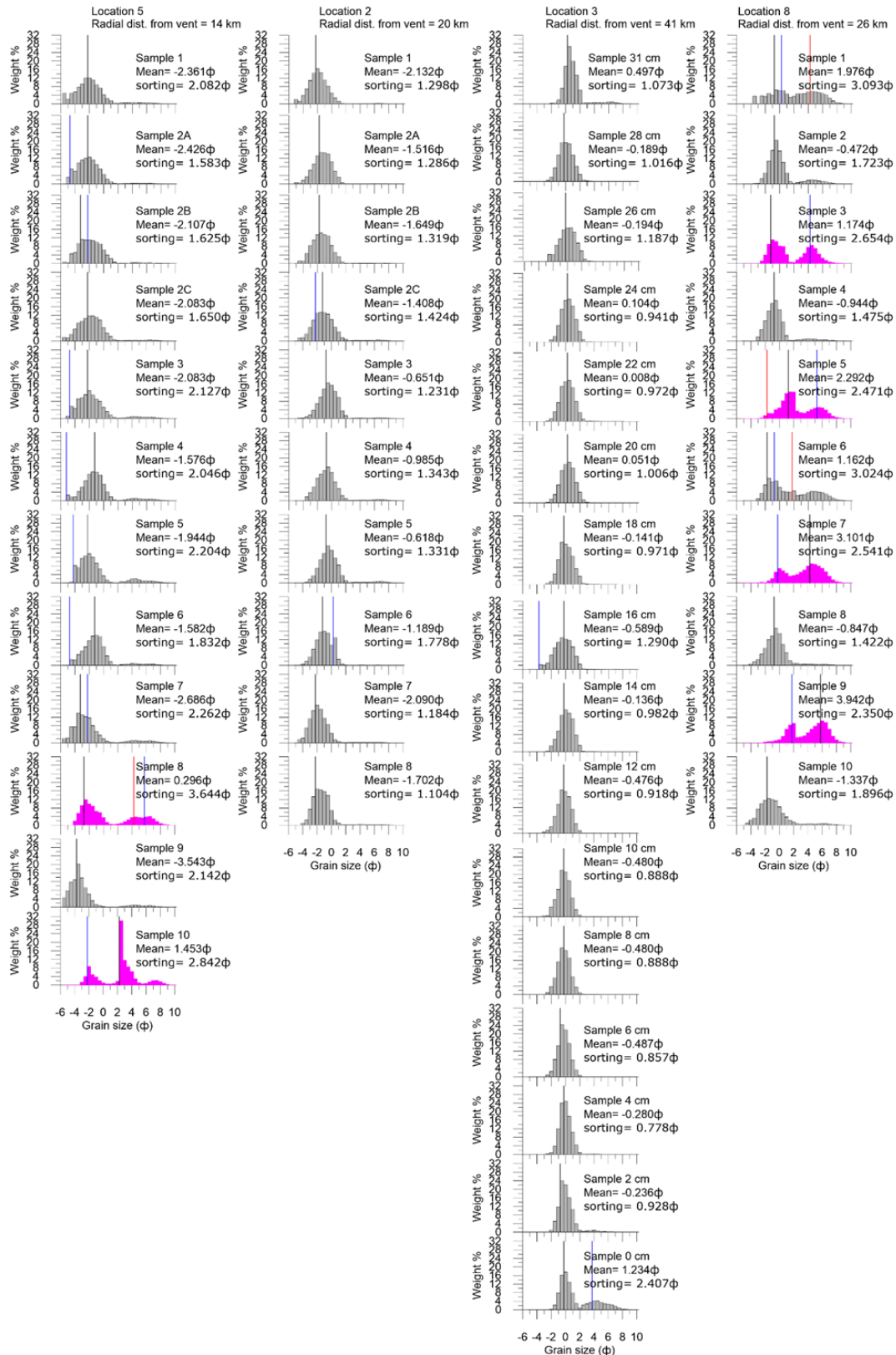


Figure 4.6 Grain size distribution histograms for each location, full profile, showing vertical grain size variations in downwind and cross wind profiles. Pink histograms outline identified ash beds. Vertical lines on histograms display modes for each histogram. Black lines = mode 1, Blue lines = mode 2, Red lines = mode 3.

Furthermore, the proportions of medium to very fine ash that make the fine-tail of the grainsize distributions systematically decreases with distance.

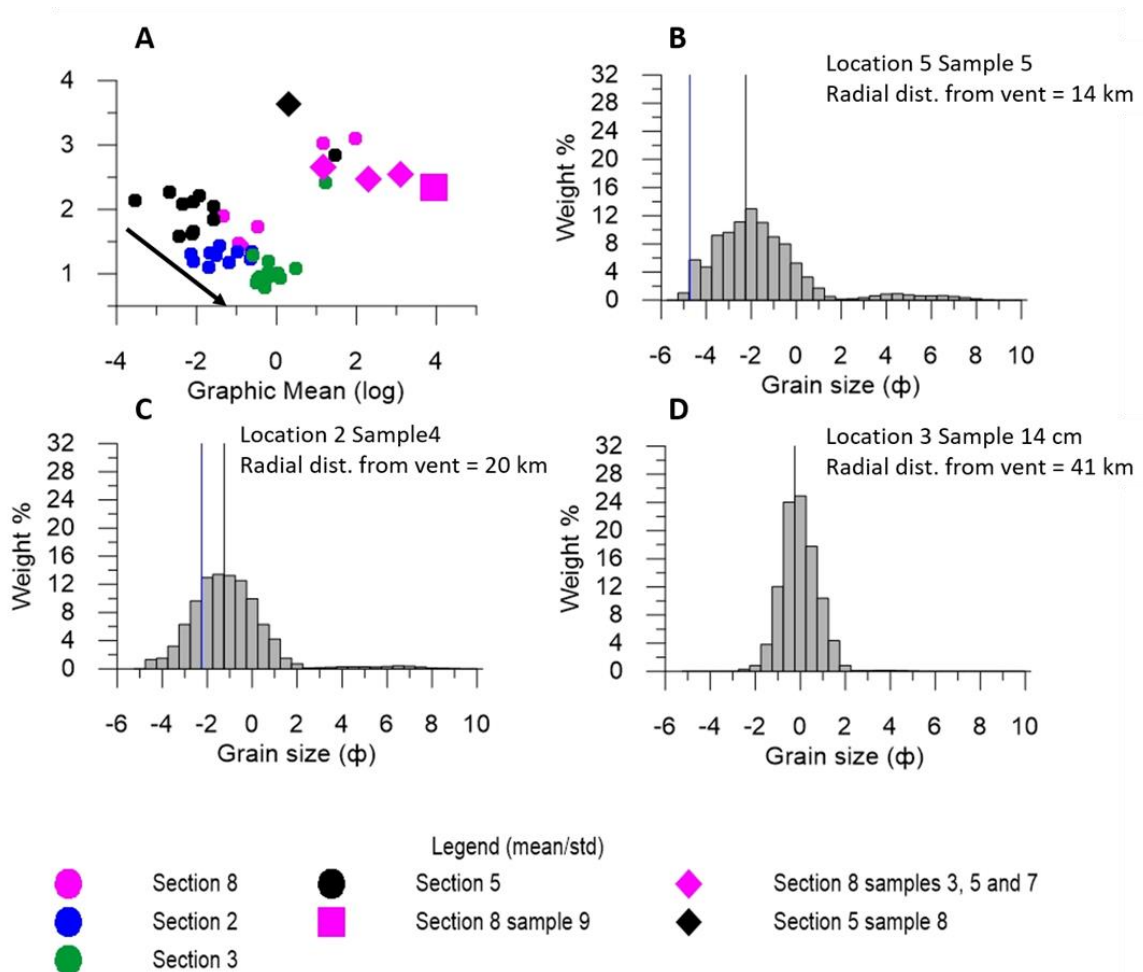


Figure 4.7 A) Scatter plot displaying graphic standard deviation, defined using Eqn 2 (Folk & Ward, 1957), against graphic mean, defined using Eqn.1 (Folk & Ward, 1957) for Locations 2, 3, 5 and 8. Round points identify fall samples from each location; black (Location 5), blue (Location 2), green (Location 3), pink (Location 8). Diamond points identify upper ash beds from Location 8, samples 3, 5 and 7, respectively, interpreted as rain-flush beds. Square points identifies sample 9 from Location 8, interpreted as dilute gravity current (see Talbot et al., 1994). Black arrow indicates increasing distance from vent B, C and D: Histograms displaying selected fall lapilli samples from Location 5(B), Location 2 (C) and Location 3 (D), note distance from vent in km. Black lines on histograms represent primary modes and blue lines represent secondary modes.

In contrast to group 1, group 2 samples have sorting coefficients greater than 2.2 phi and mean grainsizes smaller than 0 phi (Figure, 4.7a). This includes the following types of samples: At Location 8, samples 3, 5 and 7 come from layers that have been previously interpreted as rain-flush beds, and sample 9 interpreted as the deposit of a dilute gravity current (Talbot et al., 1994). Of these, sample 9 is distinct in group 2 by being the most fine-

grained and best-sorted. In Location 8, group 2 also includes samples 1 and 6 that have been characterized as ash-rich lapilli samples by their macroscopic field appearances (cf. section 4.3). The basal samples of proximal Location 5 and distal Location 3 also plot into the group 2 field. However, the histograms of both samples need to be considered cautiously, as at least their very fine ash proportion is likely contaminated by the underlying Y1 (Location 5 sample 10) and paleosol (Location 3 '0 cm'). The prominent lapilli-bearing ash bed of proximal Location 5 sample 8 is distinct in group 2 by being the most poorly sorted and coarsest sample. The histogram of this ash bed is similar in form to that of the 'rain-flush' beds of Location 8.

### Mean Particle Diameter and Main Mode

The general fining-with-distance trends of the Y2 deposit is also displayed by graphs of vertical profiles of the mean particle diameter and main mode for Locations 5, 2, 3 and 8 (Figures, 4.8 and 4.9). Considering the lapilli samples (group 1) only, decreases in mean and main mode with radial distance from vent are considerably more pronounced than their variation with stratigraphic height in each location. Location 5 shows a pronounced fining upwards in the lower 20% of the tephra profile associated with the macroscopically coarse-tail normal grading identified in the field. The upper four-fifths are relatively uniform with only a very subtle reverse grading towards the top. Similar features are seen in medial Location 2, but the reverse grading in the upper part is slightly more pronounced.

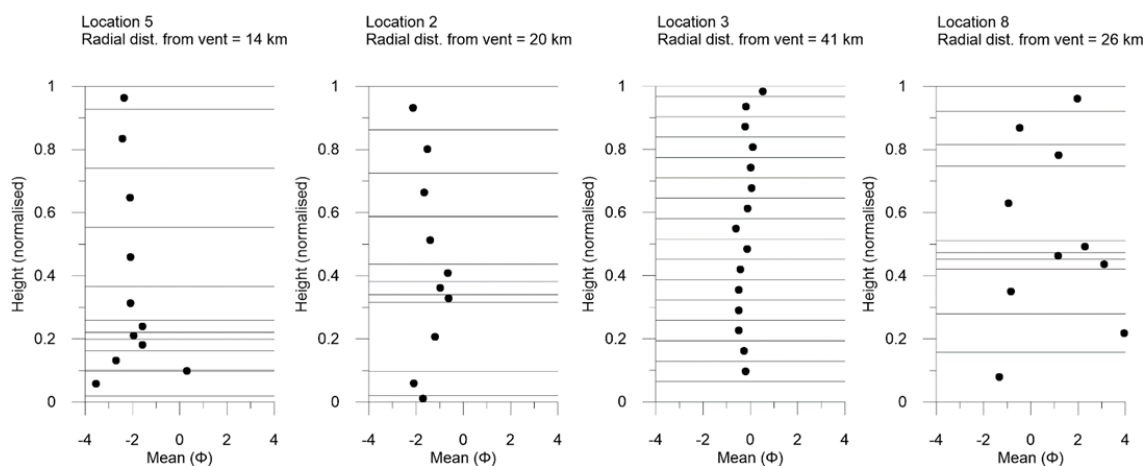


Figure 4.8 Vertical graphs comparing the mean values in phi, defined using Eqn 1 (Folk & Ward, 1957) for Locations 5, 2, 3, and 8 plotted against normalised vertical height. True height for Locations 5, 2, 3, and 8 are 234, 146, 31 and 19 cm, respectively. Black horizontal lines indicate upper boundaries for samples. Note distance from vent in km.

Furthermore, it is notable that here the transition from normal to reverse grading occurs relatively higher in the sequence at only 40% from the base (Figure, 4.8). In distal Location 3, such grading trends are absent, and group 1 samples show a subtle normal grading throughout the section.

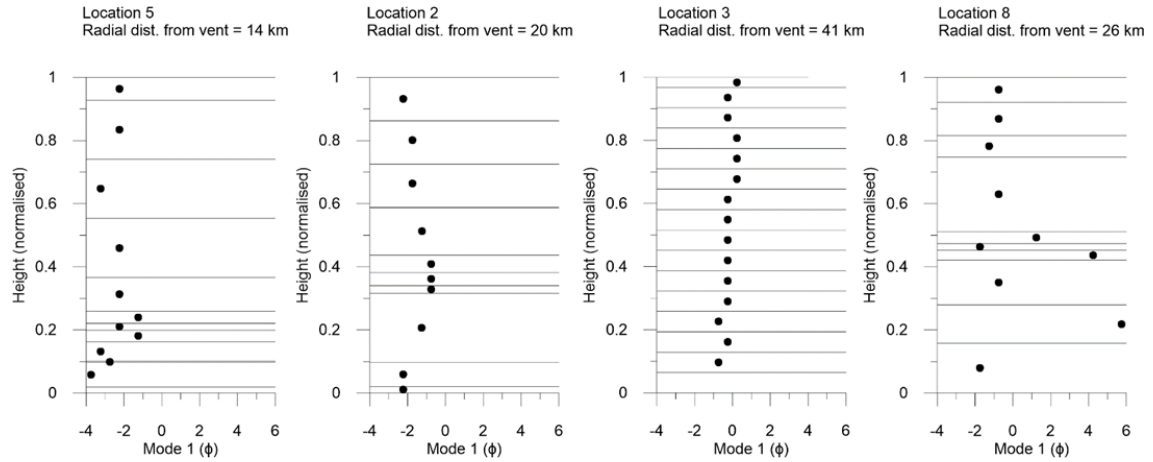


Figure 4.9 Vertical graphs comparing the main mode values in phi, for Locations 5, 2, 3, and 8 plotted against normalised vertical height. True height for Locations 5, 2, 3, and 8 are 234, 146, 31 and 19 cm, respectively. Black horizontal lines indicate upper boundaries for samples. Note distance from vent in km.

### Very Fine Ash Content

Group 1 beds are generally poor in very fine ash (<63 microns). However, there is a very clear trend of decreasing very fine-ash with radial distance from vent (Figure, 4.10), proximal Location 5 having 2 – 8 wt %, medial Location 2 1 – 4 wt % and distal Location 3 <0.5 wt %. Group 1 (lapilli) beds of Location 8 do not obey this trend, but show slightly higher contents of very fine ash than in the more proximal Location 2. Interestingly, in Locations 5 and 2, the (group 1) samples with the highest amounts of very fine ash occur at the same stratigraphic heights where the aforementioned shifts from normal to reverse coarse-tail grading are found (Figure, 4.10). Thus, main mode, mean particle diameter and very fine ash content potentially identify a compositionally distinct phase in the unit Y2 deposition. The occurrence of this ‘phase’ lower in the deposit at Location 5 than at Location 2 will be further discussed later.



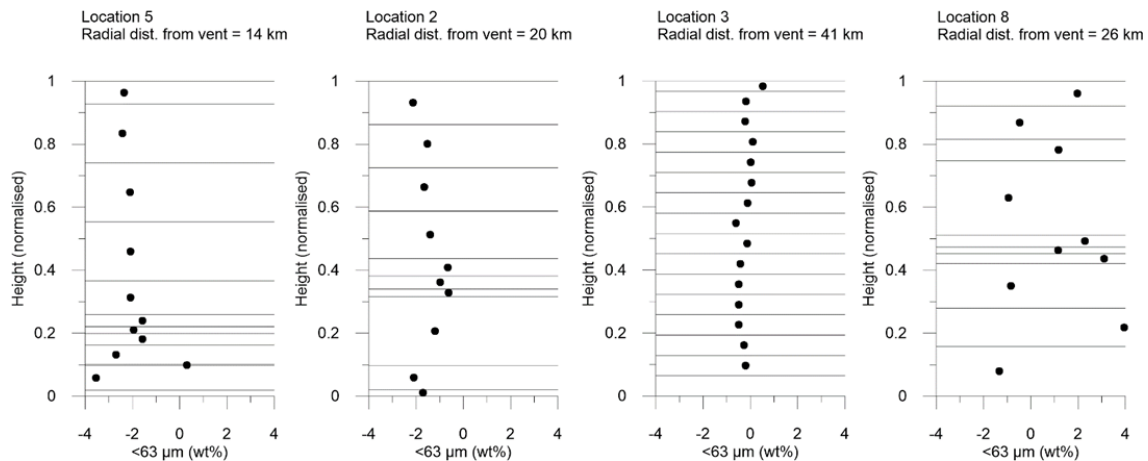


Figure 4.10 Vertical graphs comparing the  $<63 \mu\text{m}$  fraction in weight percent, for Locations 5, 2, 3, and 8 plotted against normalised vertical height. True height for Locations 5, 2, 3, and 8 are 234, 146, 31 and 19 cm, respectively. Black horizontal lines indicate upper boundaries for samples. Note distance from vent in km.

## 4.3 Componentry Descriptions

The sieved samples from Locations 5, 2 and 8 were carefully inspected to define distinct componentry classes, which can be identified and distinguished unambiguously in all three tephra profiles and thus systematically point counted. In this location, the characteristics of the defined componentry classes and the rationale behind their definitions are described and illustrated. For clarity, this section is grouped into three parts describing pumiceous and dense juvenile components, followed by non-juvenile components and finally free crystals.

### 4.3.1 Juvenile Components

There is a wide range of juvenile components that differ in their macroscopic and microscopic textures, surface properties, clast density distributions and colour. In this study, five main classes of juvenile components that occur in all samples were defined (C1, C2, C3, C4 and C5). These span from pumiceous low-density classes (C1, C2 and C3) via intermediate density class 4 (banded rhyolites) to high density class 5 (obsidian). For classes C1 to C4, thin sections from a number of representative clasts of the 4 – 8 mm ( $-2 \phi$ ) size range were prepared. Their microscopic textural characteristics were documented using a petrographic microscope and a scanning electron microscope. In each case, at least one thin section cut in the direction of any elongated fabric and one thin section perpendicular to that direction were examined. Furthermore, in order to characterize the number density

distributions of componentry classes C1 to C4, a large number of particle density analyses were conducted via envelope density measurements (see methodology section 3.3.4) on the 4 – 8 mm (-2 phi) size fraction using the upper two samples of unit Y2 at Location 2. During point counting it was noticed that an additional low-density componentry class (C2\*) occurs in the uppermost part of unit Y2 at Location 5. This component class is distinct from the other five classes and was not found in samples from Locations 2 and 8.

The six juvenile component classes that were defined on the basis of their textural and density characteristics and whose abundances were determined in the vertical profiles of Locations 5, 2 and 8 in the 1 phi and -2 phi size fractions are described below.

### Componentry Class C1

C1 is the most abundant component class in the majority of the point-counted samples. C1 is white, microvesicular pumice that contains c. 1% of microlites by visual estimate (Figure, 4.11a). Equant, spherical and ovoidal bubbles dominate the vesicle population (Figures, 4.11b, 4.12a), but more stretched and slightly fibrous types can also be recognized (Figure, 4.12b). The majority of bubbles are small and only a few tens of microns in diameter and remarkably uniform in size by visual appearance. Larger bubbles of up to c. 200 microns occur also but are sparse. The pumiceous glass has a very even and frothy appearance and bubble walls appear largely undeformed (Figure, 4.12a and b).

In several SEM images pumice structures were noticed that appear like two C1 pumice clasts had collided when still hot and deformable and sintered together. In these sintered C1 clasts strong local deformation textures mark the collision and sintering region (see Appendix, 2; Image 1).

### Componentry Class C2

C2 is typically the second most abundant juvenile (and overall) component. C2 is white, macrovesicular pumice that is, like C1, sparse in microlites (Figure, 4.11c, d). Varieties of C2 occur with equant and more elongated bubbles. In contrast to C1, C2 has a considerably higher proportion, c. 30 % by visual estimates, of larger (several hundred microns to millimeter-sized) bubbles. While small (tens of microns) bubbles still occur frequently, they are notably less abundant than in C1 (Figure, 4.12d, e). Bubble walls of C2 are notably more deformed than those in C1 and show curvilinear forms with microscopic textures usually associated with bubble coalescence (Houghton et al., 2010).

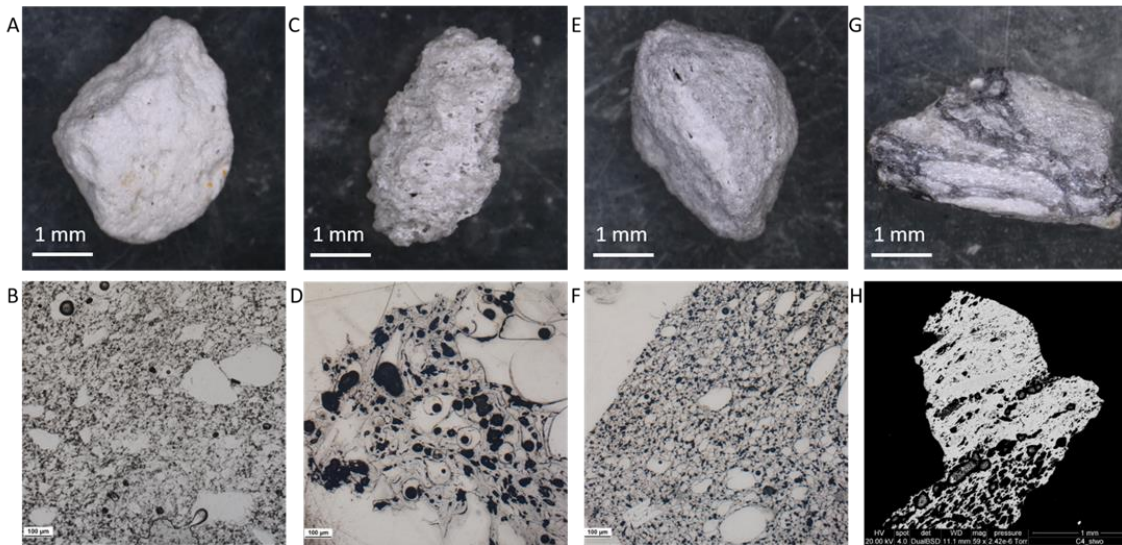


*Figure 4.11 Macroscopic photographs of juvenile pumice classes C1 (A), C2 (C), C3 (E) and C4 (G) taken on an optical microscope, note scale bar in mm. Microtextural photographs of thin sectioned juvenile pumice classes C1 (B), C2 (D), C3 (F) and C4 (H); images B, D and F were taken under 5x magnification using a petrographic microscope, note scale bar (bottom left of image) is 100  $\mu\text{m}$  in length. Image H taken on the SEM, note scale bar is 1 mm.*

These density measurements of the above two classes are consistent with those performed by Mitchell et al, (2018) using both microvesiculated pumice and macrovesiculated pumice from the 16 – 32 mm pumice from the upper 0.5 m of a proximal section of the Y2, where mean density values were reported to cluster between 600 to 700  $\text{kg}/\text{m}^3$ .

### Componentry Class C3

C3 is light grey macrovesicular pumice, which in contrast to C1 and 2 shows c. 10 – 15 % of microlites (Figure, 4.11e, f). Particularly, an abundance of microlites of titanomagnetite is a likely explanation for the distinct light grey pumice color. Bubbles are dominantly equant in form (spherical to ovoid), but domains with more elongated varieties are also seen. There is a high abundance of small bubbles tens of microns in size. Large bubbles of several hundreds of microns to millimetre-size also occur and are even slightly more abundant (c. 40 % by visual estimate) than in C2, and much more abundant than in C1, suggesting more extensive bubble coalescence. In contrast to classes C1 and C2, bubble walls are extremely thin (Figure, 4.12g). A common feature of C3 clasts is the occurrence of spectacular expansion textures. These are most apparent in the vicinity of crystals where the expansion stress is seen to have caused breakage of crystals along cleavage planes and fracture planes oblique to cleavage (Figure, 4.12h).

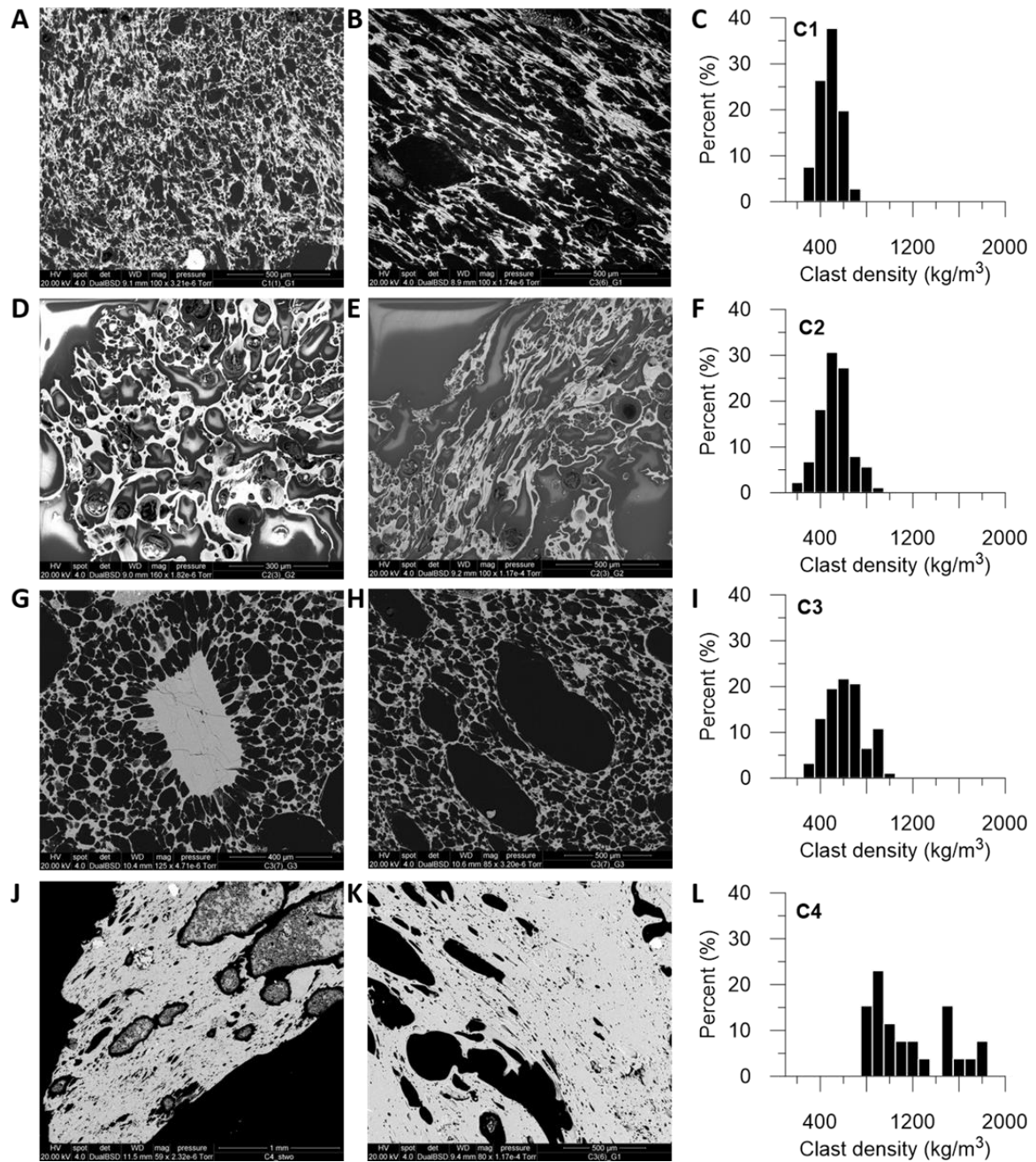


Figure 4.12 Microtextural SEM images of juvenile pumice components C1 (A and B), C2 (D and E), C3 (G and H), C4 (J and K) and their corresponding density histograms C, F, I and L, respectively. A, D and J are cut perpendicular to elongated fabric. B, E, H and K are cut along the elongated bubble fabric. Note G shows a large c. 400  $\mu\text{m}$  crystal with bubbles expanding out from the edges. Density histograms plotting pumice densities in  $\text{kg/m}^3$  (bin size 100  $\text{kg/m}^3$ ) against number percent.

### Componentry Class C4

C4 is banded clasts. C4 is characterized by alternating bands of white microvesicular to macrovesicular pumice and dark grey, less-vesicular glassy material. The widths of the bands range from around a hundred microns to several millimetres (Figure, 4.11g, h). Thin

section images of C4 clasts reveal a wealth of textures within the white bands. These include: bands with strongly sheared, very elongated and small (tens of microns) bubbles, bands with moderately sheared, elongated, smaller and larger (up to hundreds of microns) bubbles; and bands/domains where bubbles of several tens of microns in diameter have equant (spherical to ovoid) forms and surrounding bubble walls appear non-sheared (Figure, 4.12j, k). The dark-grey bands show markedly fewer bubbles than the white bands but are not here quantified. They are characterized by a very strong planar texture of sheared and partially to fully collapsed elongated bubbles. The range of high-vesicular, low-density to extremely low-vesicular, high-density textures in C4 appears to be continuous. While C4 is the least abundant of all juvenile components it occurs at a remarkably constant concentration of c. 0.5–1 % in all profiles, with one marked exception (see Section, 4.4).

### Componentry Class C5

C5 is obsidian, which occurs in black, dark grey, light grey and brown varieties (Figure, 4.13a, b). The most abundant clast type is blocky obsidian with sharp edges and conchoidal fracture surfaces. Other types include curved shards, very thick (50-100 microns) bubble walls and dense obsidian with ellipsoidal imprints from large bubbles.

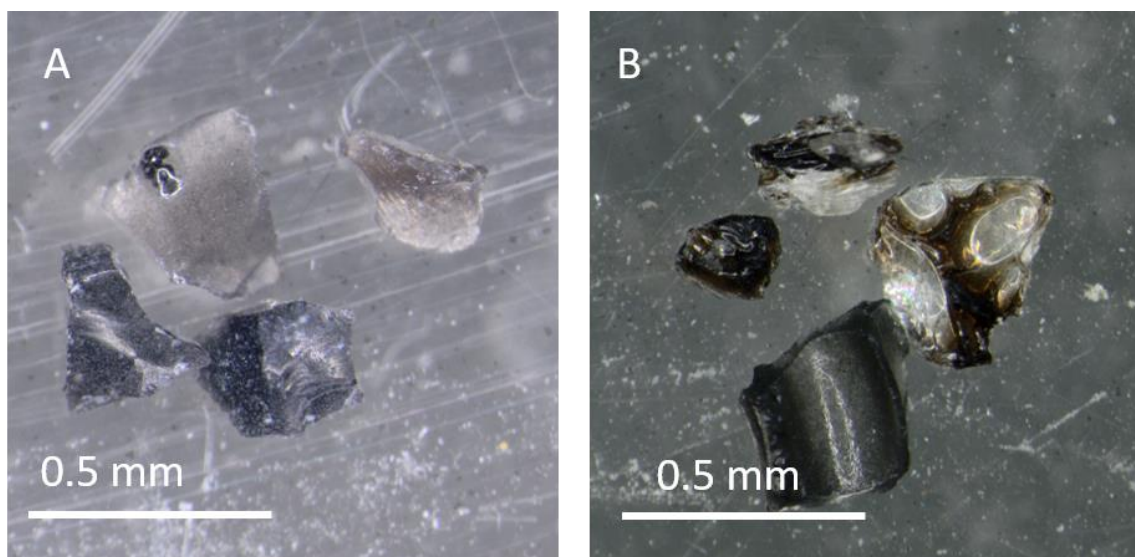


*Figure 4.13 A) Photograph of C5 at the 0.5 mm fraction displaying glass colours from transparent grey to black. Images taken on an optical microscope with a camera attachment at 2.5x magnification. B) Photograph of dark brown to black C5 with bubble impressions. Images taken on an optical microscope with a camera attachment at 2.5x magnification*

In thin section, C5 shows to be predominantly dense vesicle free glass with irregular shaped, hundreds of microns- to millimetre-wide and millimetres- to centimetres-long schlieren

zones. These schlieren zones contain clastic fresh glass shards and broken crystal fragments and comprise non-distinct contacts to the obsidian glass (Figure, 4.14). Irregular fractures through these grains are also seen to cut glass and schlieren domains (Figure, 4.14).

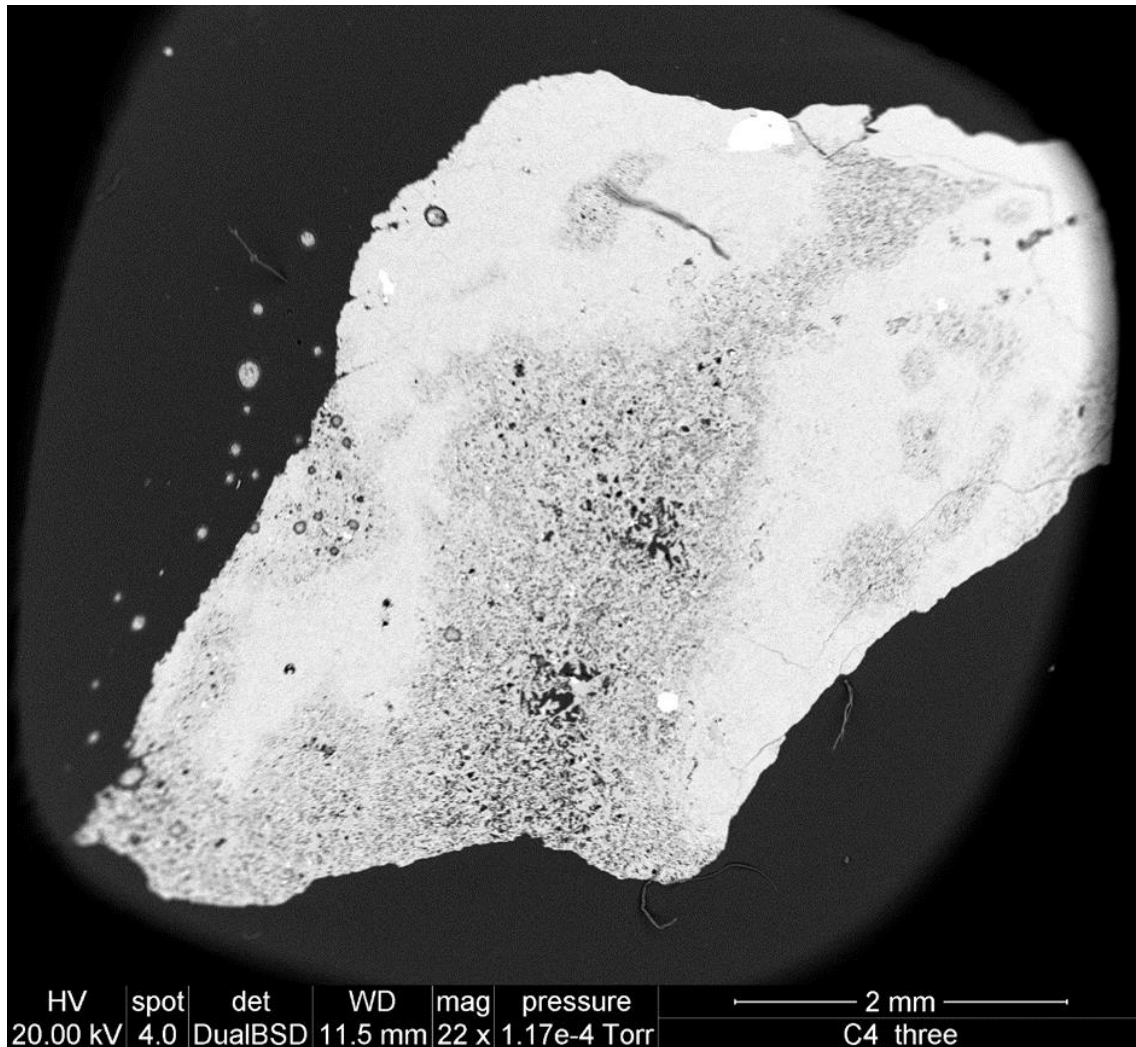


*Figure 4.14 SEM image of C5 (obsidian) displaying fracture planes around the edges, and schlieren zones in the middle of the clast.*

#### Componentry Class C2\*

C2\* is white, macrovesicular pumice (Figure, 4.15a, b). This class has only been identified in the upper part of Y2 at Location 2. Class C2\* is distinct from classes C1-C3 by its marked high transparency and the occurrence of very thick bubble walls. Bubbles are strongly stretched and deformed. Highly fibrous varieties of class C2\* also occur.

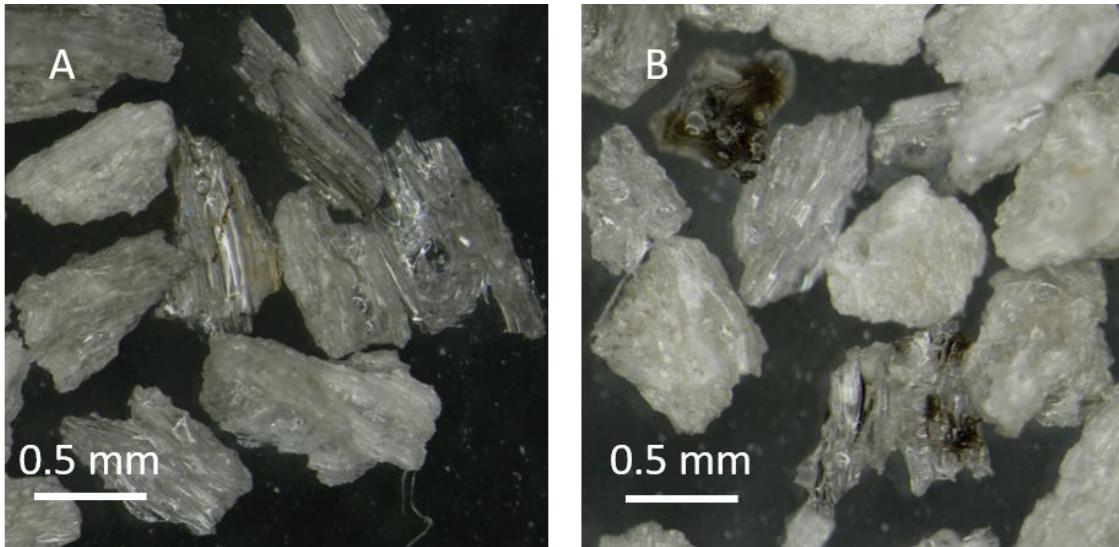


Figure 4.15 A) Photograph of thick bubble walled, transparent, glassy pumice with an elongated fabric. B) Photograph of thick bubble walled, transparent, glassy pumice with spherical to elliptical bubbles. Images taken on an optical microscope at a 5x magnification.

### Pumice Densities

Figure 4.12 shows histograms of the clast density distributions for C1, C2, C3 and C4. The average density, minima, maxima, the tenth ( $\rho_{10}$ ) and ninetieth ( $\rho_{90}$ ) percentiles of the distributions for each class are reported in Table 4.1.

- C1 shows the lowest average clast density of  $453 \text{ kg/m}^3$  and the narrowest clast density distribution ( $\rho_{90} - \rho_{10} = 261 \text{ kg/m}^3$ ) of all pumice classes with a well-defined mode at  $400 - 500 \text{ kg/m}^3$  (Figure, 6.3.2c).
- C2 has a markedly higher average density than C1 at  $482 \text{ kg/m}^3$ . The unimodal density distribution is broader than that of C1 clasts, extending further towards both the low-density and high-density tails, with  $\rho_{90} - \rho_{10} = 365 \text{ kg/m}^3$  (Figure, 6.3.2f). C3 has a markedly higher average density than C1 and C2 of  $596 \text{ kg/m}^3$ . The main mode of the roughly bimodal density distribution coincides with the average density. The distribution is significantly broader than that of C1 and C2 with  $\rho_{90} - \rho_{10} = 473 \text{ kg/m}^3$  and with the low-density and high-density tails shifted towards larger densities than in the C1 and C2 distributions (Figure, 6.3.2i).
- Due to the concurrence of light pumiceous and dense glassy domains, C4 has a very broad density distribution at intermediate densities ranging from c.  $800 - 1,800 \text{ kg/m}^3$

(Figure, 6.3.2 1). The average density of 1,119 kg/m<sup>3</sup> is considerably higher than that of the other pumice classes and  $\rho_{90} - \rho_{10} = 761 \text{ kg/m}^3$ .

*Table 4.1 Summary of the average values ( $\rho_{ave}$ ), minima ( $\rho_{min}$ ), maxima ( $\rho_{max}$ ), 10th ( $\rho_{10}$ ) and 90th ( $\rho_{90}$ ) percentiles of the clast density distributions of the C1, C2, C3 and C4 componentry classes.*

<b>Class</b>	<b><math>\rho_{ave} \text{ (kg/m}^3\text{)}</math></b>	<b><math>\rho_{min} \text{ (kg/m}^3\text{)}</math></b>	<b><math>\rho_{max} \text{ (kg/m}^3\text{)}</math></b>	<b><math>\rho_{90} \text{ (kg/m}^3\text{)}</math></b>	<b><math>\rho_{10} \text{ (kg/m}^3\text{)}</math></b>
<b>C1</b>	453.3	211.7	915.3	318.3	579.3
<b>C2</b>	482.3	180.0	807.9	303.8	668.9
<b>C3</b>	596.0	259.1	1608.5	355.7	829.2
<b>C4</b>	1119.4	760.7	1767.6	784.3	1570.5

These density measurements are consistent with those performed by Mitchell et al, (2018) using both microvesiculated pumice and macrovesiculated pumice from the 16 –32 mm pumice from the upper 0.5 m of a proximal section of the Y2, where mean density values were reported to cluster between 600 to 700 kg/m<sup>3</sup>.

### **4.3.2 Non-Juvenile Components**

The term non-juvenile components (foreign lithics) is here used to describe pyroclasts that are ejected during the eruption but are not derived from the fresh magma. These are thought to be derived from, for instance, broken-off fragments of wall rock in the sub-surface such as parts of the conduit, pre-existing hydrothermal systems, older buried rock formations and other crustal lithologies that exist between the source mush and the surface. For selected clasts, thin sections have been prepared and photographed on a petrographic microscope to analyse their microscopic textural characteristics. The dominant non-juvenile lithology in the Y2 is rhyolite lavas (c. 80 %), followed by volcanoclastic breccias and ignimbrites (c. 10 %), pumice (c. 2 %), obsidian (c. 3 %), hydrothermally altered clasts (c. 1 %), non-volcanic (clastic) sediments (c. 1 %) and intrusive rocks (c. 2 %). In this study the non-juvenile components, regardless of their lithology have tentatively been grouped into ‘shallow’, ‘intermediate’ and ‘deep’ based on their relative depths of origin, further interpreted in discussion section 7.2.



## Componentry Class C6 'Shallow'

C6 'shallow' is the most abundant non-juvenile component in all the point-counted samples. C6 'shallow' clasts consist of rhyolitic lavas, welded ignimbrites, volcanogenic breccias, obsidians and altered pumices. The 'shallow' fraction of the non-juvenile component accounts for c. 90 – 100 % of all non-juvenile clasts. The macroscopic and microscopic textures observed are displayed in Figure, 4.16 and 4.17 a, b to show the variability in lithologies for this category.

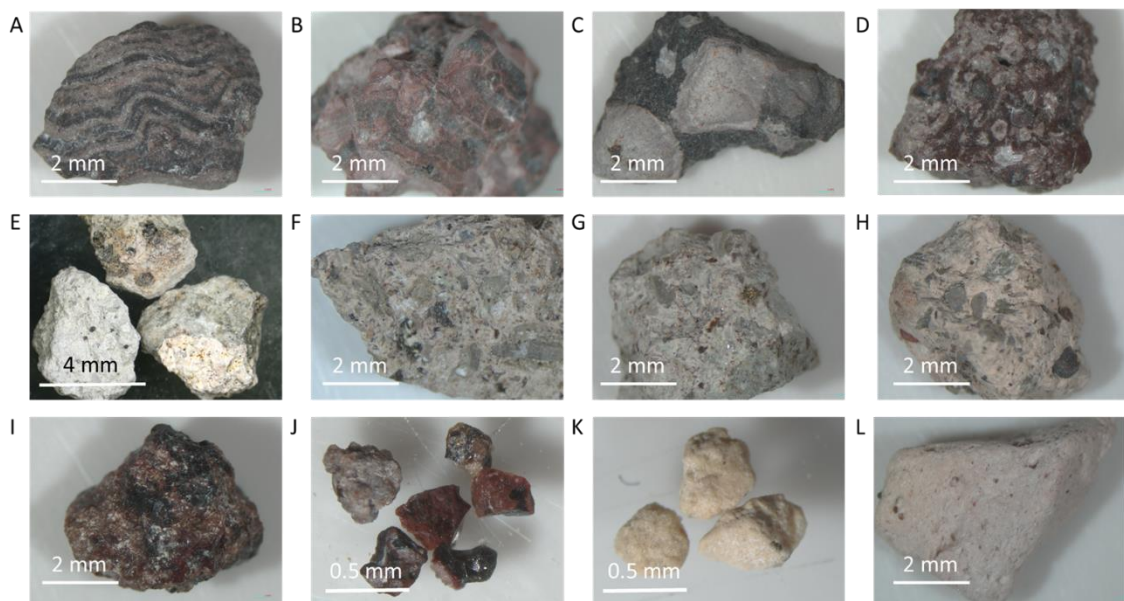


*Figure 4.16 Photographs displaying the range of 'shallow' non-juvenile clast types identified. A-D display the range of rhyolite lavas, inclusive of flow banding (A), oxidation (B and D) and spherulite growth (C and D). E-H display the reange of ignimbrite ad volcanigenic breccia fragments. I and J display the non-juvenile oxidised glass (obsidians)identified, note the white ash adhering to the particles. K and L display the non-juvenile pumice clasts identified. Images taken on an optical microscope with a camera attachment.*

*Rhyolite lava:* (relative abundance c. 80 %) Rhyolitic lavas are seen in all samples and are commonly spherulite-bearing (Figure, 4.16c, d) and/or flow-banded (Figure, 4.16a, b; Appendix, 2; Image 2). They characteristically range in colour from reddish pink to grey and black (Figure, 4.16a-d). These lavas are fine grained, ranging in shape from angular to sub-rounded with fractured plagioclase phenocrysts (Figure, 4.16b, c). Thin sections show these grains to have a fine-grained porphyritic texture with a plagioclase microlite-dominated groundmass (Figure, 4.17a). Plagioclase phenocrysts commonly appear euhedral in shape,

and are from tens to hundreds of microns long (maximum c. 500  $\mu\text{m}$ ). Minimal opaques observed, and are magnetite displaying euhedral shapes (Figure, 4.17a).

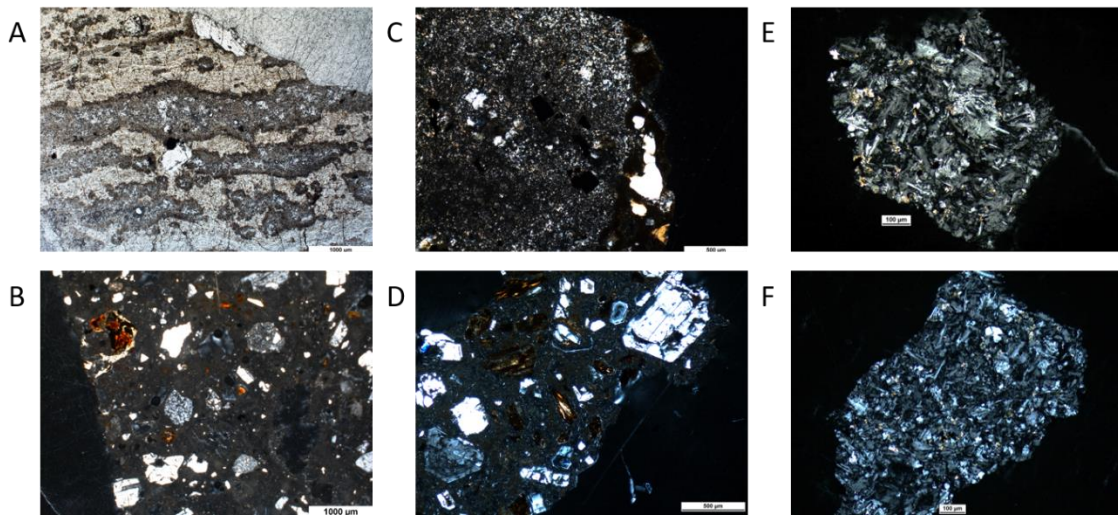


Figure 4.17 Thin section photographs of the non-juvenile clasts. A) photograph of a 'shallow' flow banded lava, B) photograph of a 'shallow' volcanigenic breccia/ignimbrite (note photographs were taken at 2.5x magnification), C) photograph of a quartzite grain from the 'intermediate group' D) photograph of an andesite from the 'intermediate' group (note these respective photographs have been taken at 5x magnification), E) photograph of a microdiorite 'Type 1' plutonic fragment from the 'deep' group, F) photograph of a microdiorite 'Type 2' plutonic from the 'deep' group (note photographs taken at 10x magnification).

*Welded Ignimbrite and Volcaniclastic Breccia:* (relative abundance c. 10 %) The welded ignimbrite and volcaniclastic breccia clasts are seen in at least some samples at all locations. These clasts range in colour from light brown to light creamy salmon pink (Figure, 4.16f, h) and light greenish grey (Figure, 4.16e, g) and are comprised of angular to sub-angular country rock fragments and plagioclase phenocrysts in a fine grained matrix (Figure, 4.16 e-h). In thin section these grains present rock, lava and crystal fragments embedded in a fine-grained, glassy, vesicle-poor to -free vitroclastic matrix. These grains crystal fraction are dominated by euhedral shaped, weak lamellar twinned plagioclase phenocrysts, ranging in size from tens to hundreds of microns long (maximum c. 500  $\mu\text{m}$ ). Altered pyroxenes and platy minerals are also observed (Figure, 4.17b) and appear brown to yellow in colour. Very few opaque minerals are observed in these grains. The rock and lava fragments incorporated into the groundmass are angular and irregular in shape and size, and appear to be predominantly microcrystalline fragments (Figure, 4.17b).

*Obsidian:* (relative abundance c. 5 %) Foreign obsidians are observed in all sections in minor abundance. These obsidians are defined as non-juvenile mainly due to their colour alteration. Non-juvenile obsidians are primarily red and black (Figure, 4.16i, j) which is evidence of oxidation, not seen in juvenile obsidians (clast type C5, above). These grains also display rounded edges and rough abraded surfaces, which fine ash has stuck to.

*Altered pumice:* (relative abundance c. 5 %) Altered pumice is a minor component seen in at least some samples at all locations. These pumices are microvesicular to macrovesicular and range in colour from a light green, to iron-stained yellow/brown (Figure, 4.16k) and light pink (Figure, 4.16l). These pumice grains are differentiated from juvenile pumice grains based on their colour and shape. Non-juvenile pumice tends to be noticeably rounded in shape. The green pumice is noticeably glassy with ash filled vesicles predominantly occurring in the 1 phi size fraction.

#### Componentry Class C6 'Intermediate'

C6 'intermediate' is the least abundant of all non-juvenile components and is not present in all point-counted samples, and accounts for an average abundance of 1 % or less of the non-juvenile components. These are typically grains that are clastic sedimentary in origin or hydrothermally altered clasts. There are only four types observed and occur at Locations 5 and 2. They are predominantly present in the -2 phi grain size fraction.

*Grey lacustrine sediments:* These sediments are fine grained, rounded to sub angular in shape and are grey to cream in colour (Figure, 4.18b), occurring mostly in the -2 phi size fraction although also present in the 1 phi fraction. These grains have an average abundance of c. <1 % and equate to c. 25 % of the 'intermediate' clasts. The genesis of these grains can be linked to lacustrine environments (see section 5.2.2).

*Green sandstone:* These grains have an average abundance c. <1% and predominantly occur in the -2 phi grainsize fraction. These grains are hydrothermally altered and appear green in colour due to the presence of chlorite (Figure, 4.18c). These grains are sub-rounded in shape and have a roughened surface. Black and dark brown alteration is seen on the outer surface.

*Quartz grains:* The quartz grain is of sedimentary origin and is most likely a fragment of quartzite and is very rare. There was only one grain found in the -2 phi size fraction and is a white fine-grained clast (Figure, 4.18a). In thin section (Figure, 4.17c) this grain displays a

fine-grained microcrystalline matrix with abundant euhedral shaped opaque minerals; predominantly magnetite and pyrite (identified by their black cube shapes under both cross polarised and plain polarised light), ranging from c. 100 – 200  $\mu\text{m}$  across. Higher amounts of brown to yellow alteration colours are seen on the outer edges of the grain relative to the centre, suggesting it resided at depth for the alteration to occur.

*Altered Andesite:* These grains are rare; only two were counted. These grains are grey, sub-angular to sub-rounded fragments of porphyritic andesite that are fragile and easily broken with rough outer edges. In thin section (Figure, 4.17d) these clasts display a fine grained microcrystalline felsic ground mass with feldspar phenocrysts that have strong oscillatory zoning, ranging from tens to hundreds of microns long. Abundant brown altered ferromagnesian minerals also occur that are tens to hundreds of microns long (Figure, 4.17d).

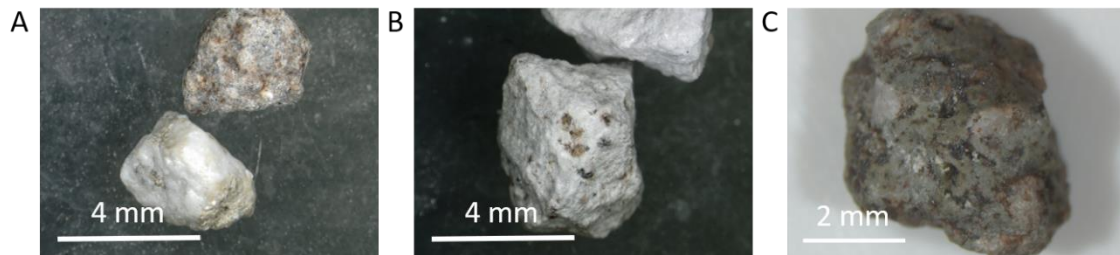


*Figure 4.18 Photographs displaying the range of ‘intermediate’ non-juvenile lithologies. A) Quartzite grain, B) grey lacustrine sediments, C) green hydrothermally altered sandstone. All clasts are from the -2 phi size range. Note scale in mm. Photographs were taken on an optical microscope with a camera attachment.*

### Componentry Class C6 ‘Deep’

Class C6 ‘deep’ is the second most abundant of the non-juvenile components with an average abundance of c. 2 %. These grains are predominantly identified in the 1 phi grainsize fraction and are plutonic in origin. Here this class has been split into two types based on the accessory minerals present. Type 1 (white microcrystalline matrix with black crystals) and Type 2 (white microcrystalline matrix with orange crystals).

*Plutonic Type 1:* These grains are fine grained, plagioclase dominated, microcrystalline clasts speckled with black crystals (Figure, 4.19b). They range in shape from angular to sub-angular and have rough surface textures. In thin section these grains appear to be microdiorites, displaying inter-fingered and interlocked textures of needle shaped plagioclase crystals (Figure, 4.17e) that have weak lamellar twinning. Moderate abundances

of yellow to light brown coloured alteration minerals are inferred to be altered micas and apatite.

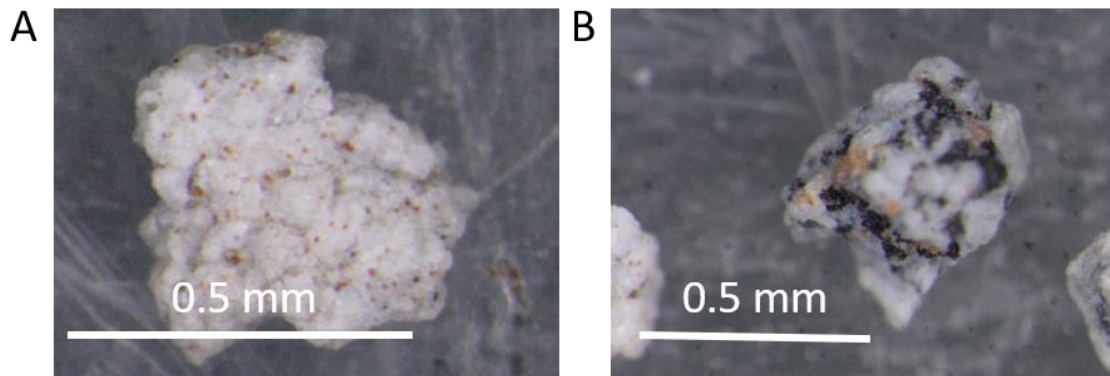


*Figure 4.19 Photographs of the ‘deep’ non-juvenile group. ‘Type 1’ (B) and ‘Type 2’ (A) plutonic fragments from the 1 phi size range of the . Photographs taken on an optical microscope with a camera attachment.*

*Plutonic Type 2:* These grains are also fine grained microdiorites, and are the most common of the ‘deep’ non-juvenile class. They are white to light grey and dominated by fine plagioclase crystalline textures and speckled with orange minerals. These grains are angular to sub-rounded (Figure, 4.19a), and in thin section display interlocked textures of needle shaped plagioclase crystals that range in size up to tens of microns long (Figure, 4.17f). Minor abundances of alteration minerals are observed, and minimal abundances of larger plagioclase crystals (up to 100 microns long).

### **4.3.3 Free Crystals**

#### **Componentry Class C7**

C7 is the free crystal component. In the 1 phi grain size fraction its abundance varies between c. 10 and 50 %, but it is rare in the -1 phi grainsize fraction and not present in coarser size fractions. Class C7 predominantly consists of plagioclase, pyroxene, quartz and titanomagnetite with relative abundances of c. 65 % plagioclase, c. 30 % pyroxene, and c. 5 % magnetite (Figure, 4.20a, b).

*Plagioclase:* Plagioclase is the most abundant crystal type observed. The plagioclase crystals are subhedral to euhedral in shape with a c. 90° cleavage and are light white to transparent crystals. These crystals appear at -1 phi and smaller. Most original growth surfaces display

smooth textures with the exception of c. 30% which show rough textures from adhering glass. Fractured crystal surfaces display rainbow reflectance.

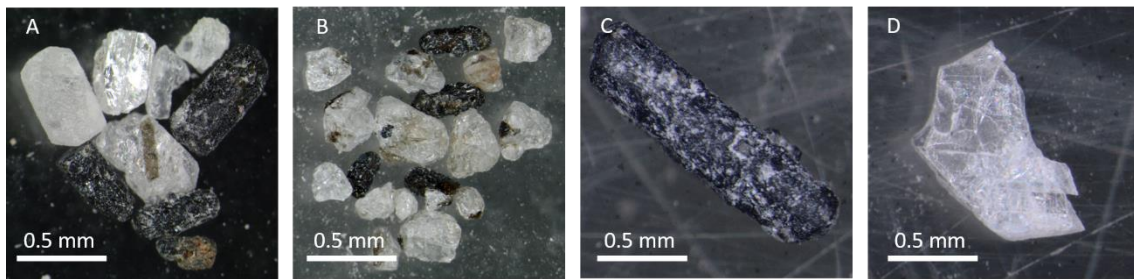


*Figure 4.20 Photographs of free crystals A and B display clusters or plagioclase (white/translucent), Pyroxene (brown and green) and magnetite (black cube) studded within the plagioclase crystals. C) euhedral pyroxene studded with black magnetite crystals, and D) fractured plagioclase. Photographs taken on an optical microscope with a camera attachment. Grains are from the -1 phi grain size fraction.*

*Pyroxene:* Pyroxene is the second most abundant crystal type. Dark brown to resinous brown orthopyroxenes with euhedral forms constitute the most abundant pyroxene type (Figure, 4.20c). Often pyroxenes are observed to be studded with small cubes of opaque black magnetite (Figure, 4.20c). Clinopyroxene is represented in minor abundances and is equant in shape and green in colour.

*Magnetite:* Magnetite has the lowest abundance with a relative class abundance of c. 5 – 10%. The magnetite component predominantly appears as small black octahedral phenocrysts, often grown on plagioclase and pyroxene crystals.

## **4.4 Vertical and Lateral Componentry Variations in Y2**

The clast components (both juvenile and foreign) introduced in section 6.3 were point-counted in all sub-unit samples from Locations 5, 2 and 8. For the Location 8 samples, componentry counts for all full phi grain-size classes 250 microns and larger was done. For Locations 5 and 2, componentry point-counts were conducted for the size classes 500 – 1000 microns (1 phi size class) and 4 – 8 mm (-2 phi size class). The rationale behind this focus on the 1 phi and -2 phi fractions was to choose two size classes that have sufficiently large numbers of clasts in the sieved size fractions, which are characteristic size fractions for the dominant coarse tail of the Y2 samples and which can be unambiguously

classified using a binocular microscope. The reason behind the more complete point counts for Location 8 samples was to characterize general patterns in the abundances of different components as a function of grain size (for instance free crystals, which typically are restricted to size ranges below  $-1 \phi$ ). Identification of such a pattern would aid interpretation of component abundances of the  $1 \phi$  and  $-2 \phi$  size fractions in vertical profiles and between profiles. In all samples, the clasts of each componentry class were counted, separated and weighed to allow for calculation of componentry percentages by both number and mass.

The results of the componentry point counts are presented in two parts. Grain-size dependent variations of componentry classes based on Location 8 samples are described in Section 4.4.1. Section 6.4.1 also highlights differences in vertical componentry variations in the  $1 \phi$  and  $-2 \phi$  size classes for Locations 2, 5 and 8 to demonstrate that the defined componentry classes are more completely present in the  $1 \phi$  size class. Section 4.4.2 then presents detailed results of vertical and lateral componentry variations at Locations 2, 5 and 8, based on the  $1 \phi$  size fraction.

#### **4.4.1 Componentry Variation with Grainsize**

Histograms of the abundance of componentry classes (by mass) against grain-size at Location 8 are shown in Figure, 4.21 (see also Figure. 4.22 for a comparison of componentry abundance by number and mass as per samples 10). Samples 2, 4, 8 and 10 are fines-poor coarse ash- to lapilli-dominated samples, which are comparable in granulometry and componentry to the remainder of fall samples studied at Locations 2 and 5. In these samples, clear patterns of variations in componentry abundances at different grain-size are present. The low-density components (classes C1, C2 and C3) constitute the dominant components (by number and mass) of the lapilli-range of the grain-size distribution (that is the coarse-tail of the roughly unimodal grain-size distributions). The ash-size range of the analysed grain-size classes (that is the fine-tail of the roughly unimodal distributions) is dominated by the high-density components (classes C5, C6 and C7). The abundant componentry classes C1 (microvesicular pumice) and C6 (foreign lithics) are good examples to show that their mass percentage against grain-size pattern have roughly unimodal distributions, with the mode and range of C1 tending towards the coarse sizes and that of C6 towards smaller sizes (Figure, 4.21). The occurrence and degree of aerodynamic equivalence, as a likely

explanation behind this pattern, will be discussed in Section 5. The same pattern of light components dominating coarse fractions and heavy components dominating fine size fractions is also seen in the lapilli-bearing ashes and ash-rich lapilli layers that occur at Location 8. Free crystals, due to their size spectrum, are generally limited to size classes  $\leq 0$  phi. The mode of the crystal population is somewhat variable among the Location 8 samples, but generally is between 0 – 1 phi.

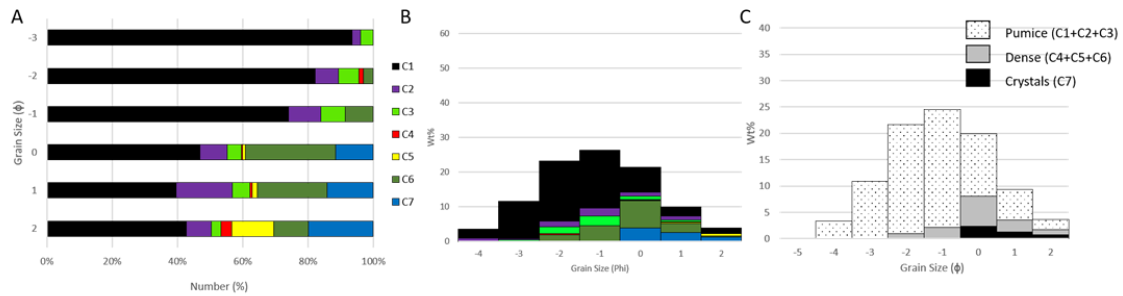


*Figure 4.21 A) Bar graph of individual componentry point count number percents against grain size (phi) from Location 8 sample 8. Componentry class colours as indicated by legend in the right of the graph. B) histogram displaying mass of individual components (weight percent) by grain size (phi) for Location 8 sample 8. C) histogram displaying mass of combined components (weight percent), see legend top right of graph, by grain size (phi) for Location 8 sample 8.*

Graphs of componentry variation by clast number percent and mass by weight percent (Figure, 4.22) highlight that the 1 phi grain-size material includes an abundance, number percent, of clasts in all of the defined componentry classes. By contrast, in the -2 phi size class, only classes C1, C2, C3, C4 and C6 occur, strongly dominated by C1. While this characteristic is important in order to interpret gas-particle transport in the umbrella cloud, componentry variations in the 1 phi size class, due to their complete and more similar abundances, provide more detail to interpret possible variations in magma vesiculation, fragmentation and interaction with the conduit walls and country rocks.

Figure, 6.4.3 compares vertical componentry variations of the -2 phi and 1 phi size classes at Locations 2, 5 and 8. For clarity, the eight componentry classes are sorted into four groups: low-density juvenile components (C1 + C2 + C2\* + C3); intermediate- to high-density juvenile components (C4 + C5); foreign lithics (C6) and free crystals (C7). In the -2 phi size class, the low density juvenile classes (C1-C3) strongly dominate in all profiles and constitute generally >95% of the clast population. Intermediate- to high-density juvenile



classes C4 and C5 and foreign lithics (C6) occur at less than a few percent, while free crystals are absent. In contrast, in the 1 phi class, all componentry classes C1 to C7 are well represented at statistically significant numbers (relative to the sample sizes). Furthermore, strong vertical variations of componentry abundance become apparent (next section).

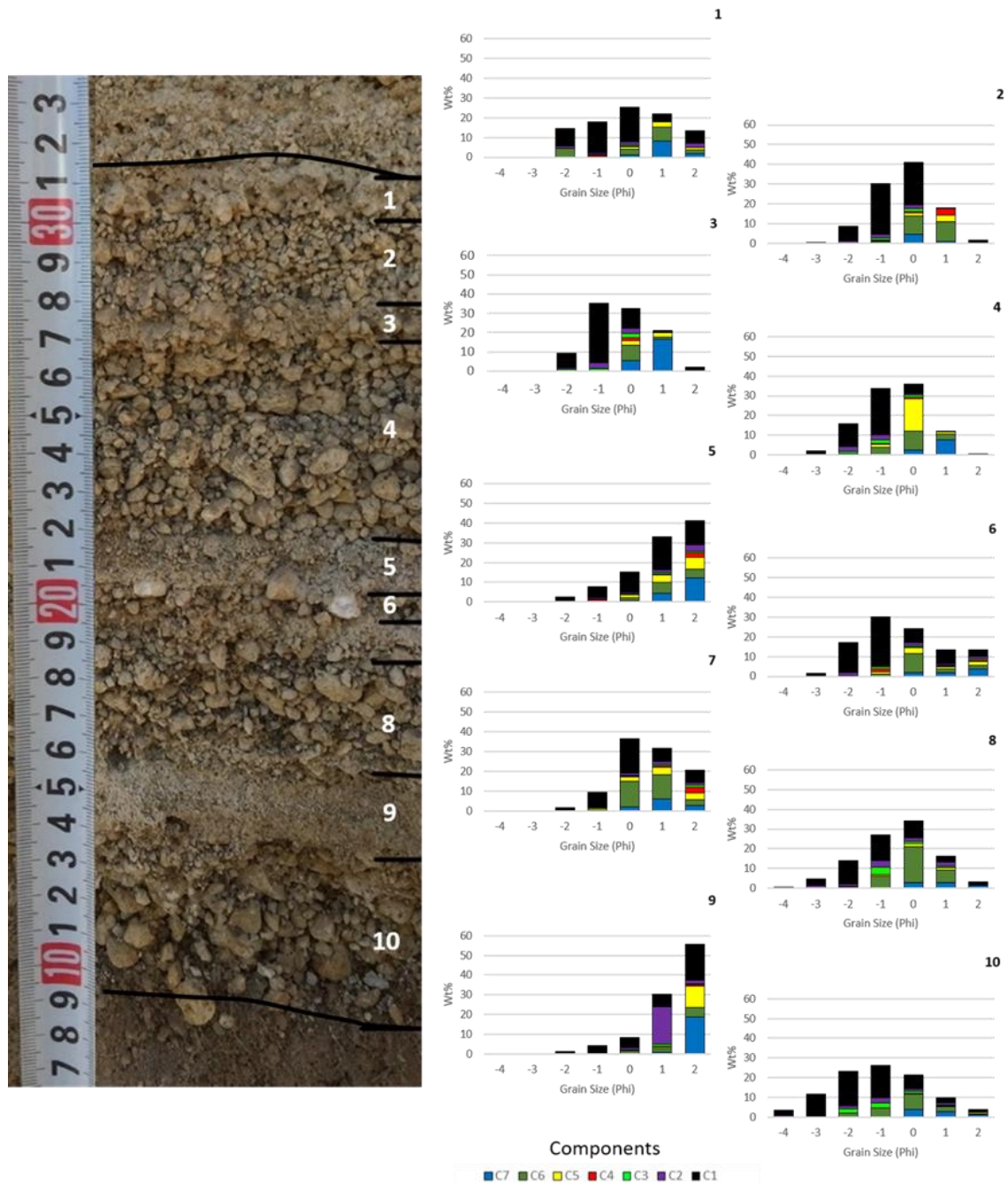


Figure 4.22 Location 8 tephra profile; white numbers are sample number and correspond to the samples histograms on the right. Histograms display mass of individual components(weight percent) by grain size (phi) for each sample at Location 8. Black line on photograph mark the upper and lower sample boundaries.

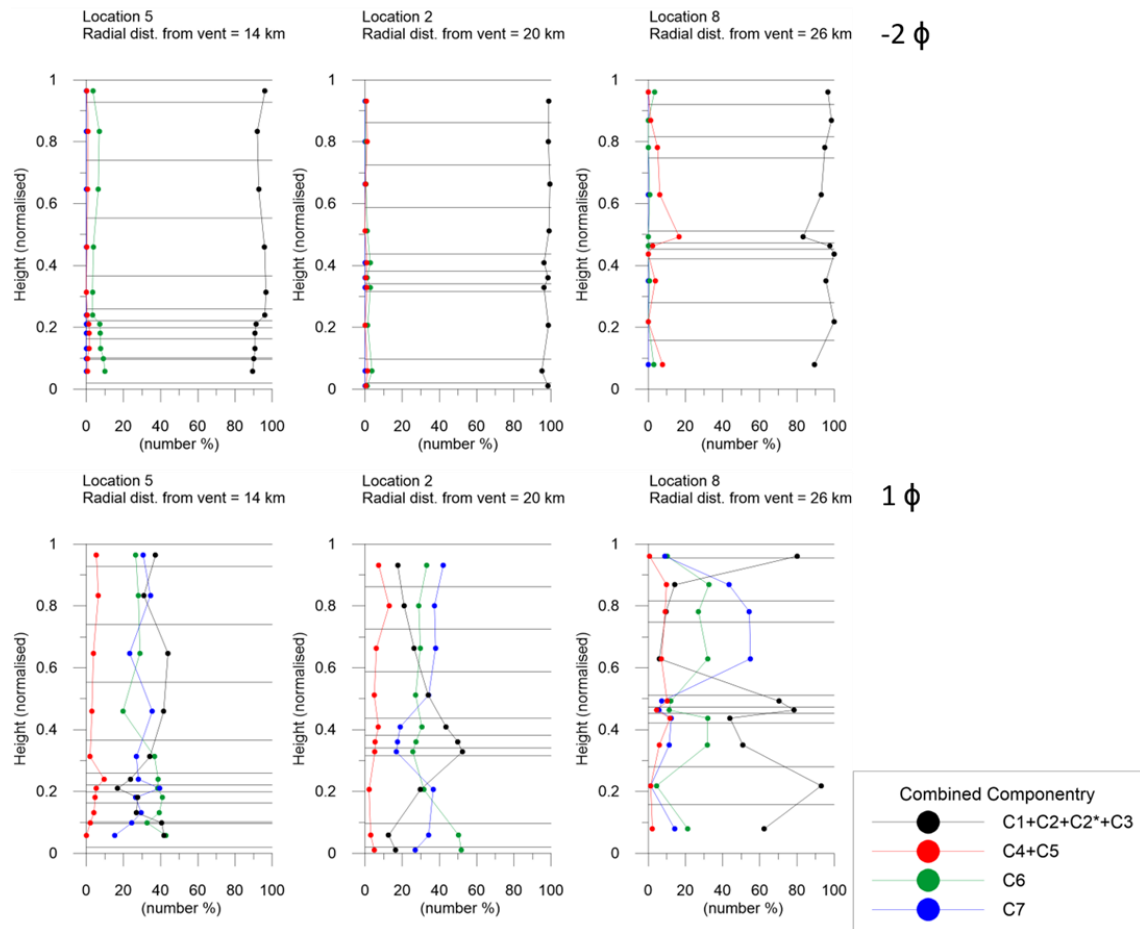


Figure 4.23 Vertical graphs comparing combined point count number percent and normalised height for Locations 5, 2, 3, and 8. True height for Locations 5, 2, 3, and 8 are 234, 146, 31 and 19 cm, respectively. Black horizontal lines indicate upper boundaries for samples. Note distance from vent in km..Upper Graph plots the  $-2 \phi$  componentry and Lower Graph plots the  $1 \phi$  componentry. Note colours are determined by class groupings as seen in legend

#### 4.4.2 Vertical and Lateral Componentry Variations in the 1 Phi Size Class

Figure, 4.24 and Figure, 4.25 shows the vertical variation of the number percentage of all eight componentry classes in the 1 phi size fraction for Locations 2, 5 and 8. Due to the normalization to 100 percent of the components of each sample, however, some ‘trends’ in vertical componentry variation need to be viewed with caution. For instance, a strong vertical variation in an abundant component class will cause apparently opposite variation in another abundant componentry class.

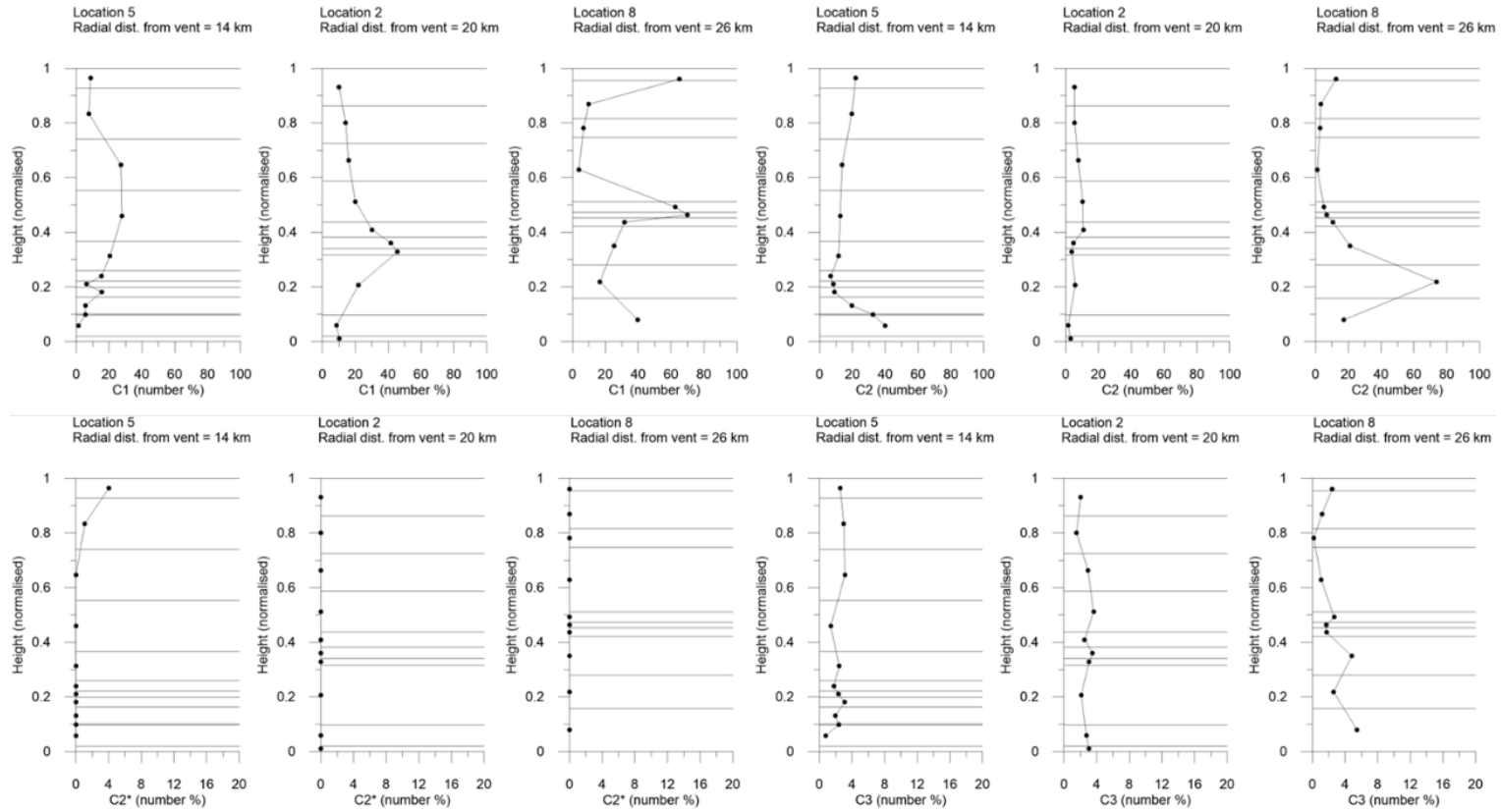


Figure 4.24 Vertical graphs displaying vertical variations in the 1 phi componentry for Locations 5, 2, 3, and 8 plotted against normalised vertical height. True height for Locations 5, 2, 3, and 8 are 234, 146, 31 and 19 cm, respectively. Black horizontal lines indicate upper boundaries for samples. Note distance from vent in km.

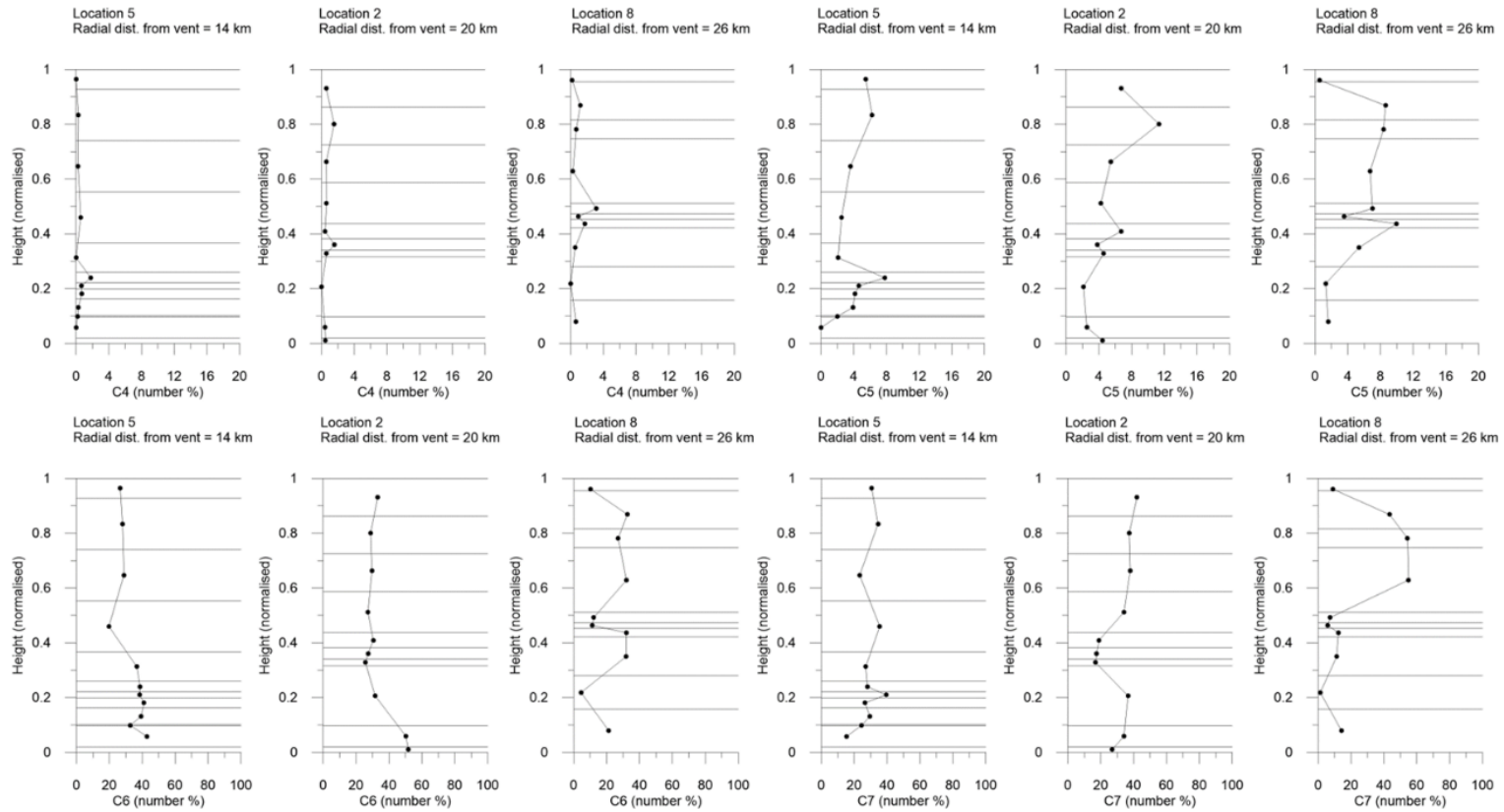


Figure 4.25 Vertical graphs displaying vertical variations in the 1 phi componentry for Locations 5, 2, 3, and 8 plotted against normalised vertical height. True height for Locations 5, 2, 3, and 8 are 234, 146, 31 and 19 cm, respectively. Black horizontal lines indicate upper boundaries for samples. Note distance from vent in km.

## Vertical Variation

In the following, the relative abundances of the eight componentry classes and their vertical (that is relative temporal) variations are described from Location 5 (Figures, 4.24 and 4.25). The Location 5 tephra profile, as will be demonstrated below, appears to record the most complete sequence of sedimentation from the Y2 umbrella cloud. At Location 5, the height-averaged number percentages of the eight componentry classes in order of abundance are: foreign lithics (C6; c. 34 %), free crystals (C7; c. 28 %), macrovesicular pumice (C2; c. 18 %); microvesicular pumice (C1; c. 13 %); obsidian (C5; c. 3.8 %); grey pumice (C3; c. 2.3 %); banded pumice (C4; c. 0.5 %); transparent pumice (C2\*; c. 0.4 %).

*Microvesicular pumice (C1)* starts at low abundances of c. 1 %, then increases strongly and continuously to values of c. 28 % at about 70 % of the deposit thickness and shows markedly lower values of around 8 % in the uppermost 30 % of the profile.

*Macrovesicular pumice (C2)* starts with a high abundance of c. 40 %, then decreases strongly and continuously to values of 6 – 9 % between 18 – 25 % of the total deposit thickness and increases continuously again towards the top of the profile where C2 clast proportions reach c. 26 %.

*Transparent (thick bubble-walled) pumice (C2\*)* is characteristically absent from the lower c. 75 % of the profile (and completely absent at profiles 2 and 8) and increases in the top 25 % of the section to maxima of c. 4 %.

*Grey (crystal-rich) pumice (C3)* has characteristically height-invariant abundances of c. 2.2 %  $\pm$  0.7 %.

*Banded pumice (C4)* has a characteristically very low abundance of c. 0.2 %. However, in the height interval of c. 18 – 25 % of the total profile thickness, C4 increases to maximum values of 1.8 %.

*Obsidian (C5)* is absent in the lowermost sample of the profile, but above that increases strongly to reach a maximum value of c. 8 % at 25 % of the total deposit thickness. Immediately above, C5 decreases strongly to around 2 % and then continuously increases again to the top where C5 occurs at c. 5.5 %.

*Foreign lithics (C6)* have their maximum abundance of c. 43 % at the base of the deposit. From there upwards C6 decreases relatively continuously to minimum values of c. 27 % at the top. Figures, 4.25 and 4.27 illustrate the vertical variation in the proportion of foreign lithics interpreted as being sourced from ‘shallow’, ‘intermediate’ and ‘deep’ subsurface levels (an explanation behind this interpretation is given in Section 5.2). The data show that 93 % (on average) of the lithics are of the ‘shallow’ type. ‘Intermediate’ lithics are rare at any level of the profiles. ‘Deep’ lithics start with relatively high abundances of up to c. 15 % at the base of the profile, then decrease upwards and show markedly low values (down to c. 1.5 %) in the interval from 18 – 25 % of the total height. Above this level, in the upper 75 % of the profile, ‘deep’ lithics have moderate and relatively uniform abundances of 5 – 10 %; except for the uppermost samples where they drop to c. 1 %.

*Free crystals (C7)* have minimum abundances of c. 15 % in the lowermost sample of the profile. Above, and for the remainder of the profile, class C7 is relatively uniformly abundant with a height-average value around 28 % and a tendency to show a slight overall increase with height to values of c. 30 %.

### Lateral Variations

In comparison to Location 5 at c. 14 km from source, vertical componentry variation at Locations 2 (c. 20 km from vent) and 8 (c. 26 km from vent) show a range of similarities and differences. In terms of height-averaged component abundances in number percent the following characteristics are observed (Figures, 4.24 and 4.25).

*Microvesicular pumice (C1)* strongly increases with increasing distance from vent from c. 12% at Location 5, through c. 22 % at Location 2 to c. 34 % at Location 8.

*Macrovesicular pumice (C2)* strongly decreases from c. 20 % at Location 5 to c. 6 % at Location 2 but increases again to c. 15 % at Location 8 (and c. 9% if samples 9 (interpreted as the deposit of a gravity current) is excluded).

The ratio of microvesicular pumice over macrovesicular pumice, C1/C2 shows similar trends with height in all three profiles and initially increases to a maximum value and then decreases again (Figure, 4.26). The heights of this C1/C2 maximum occurs at Location 5 at c. 20 % of the total profile thickness, at Location 2 at c. 35 % of the total thickness and at Location 8 at c. 60 % of the total thickness.

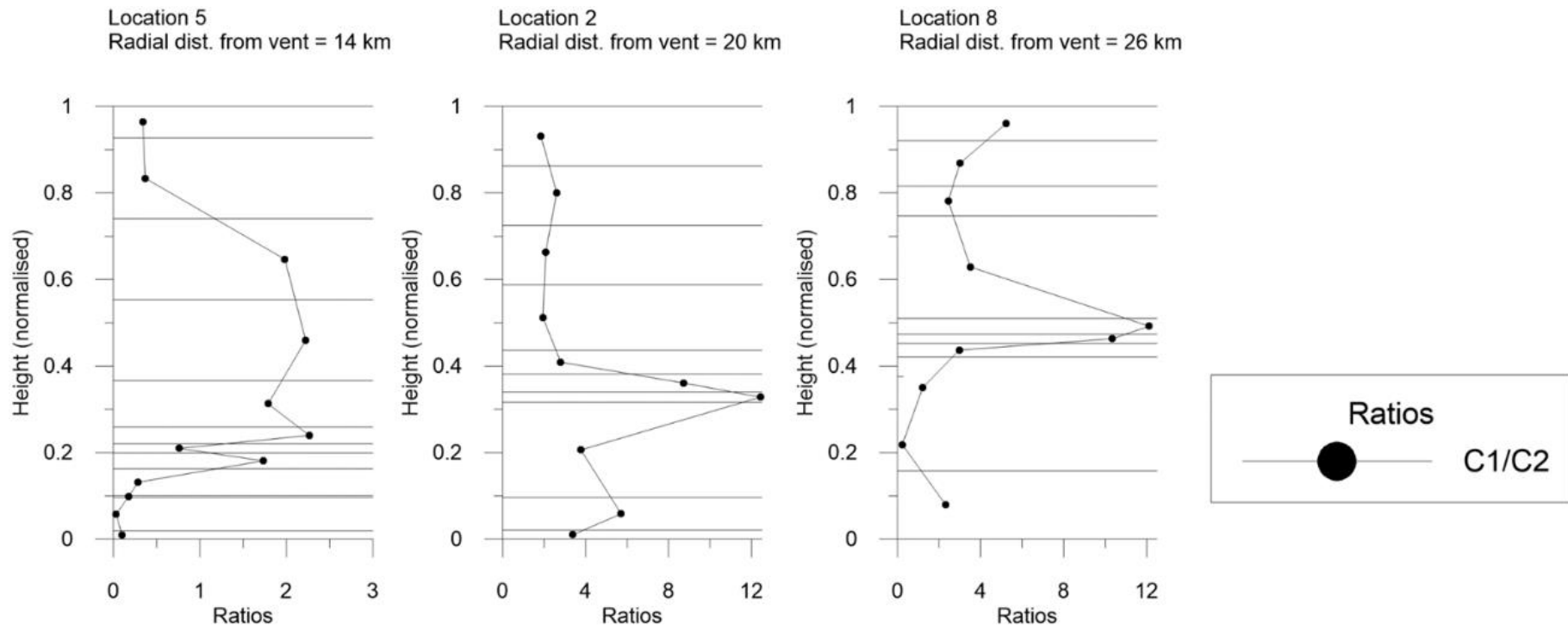


Figure 4.26 Vertical graphs displaying C1:C2 ratio values for the 1 phi componentry at Locations 5, 2, 3, and 8 plotted against normalised vertical height. True height for Locations 5, 2, 3, and 8 are 234, 146, 31 and 19 cm, respectively. Black horizontal lines indicate upper boundaries for samples. Note distance from vent in km.

*Grey (microlite-rich) pumice (C3)* shows low abundances and very similar height-averaged values at all three locations ( $2.3 \pm 0.7$  % at Location 5;  $2.4 \pm 1.3$  % at Location 2; and  $2.4 \pm 1.3$  % at Location 8). While at Locations 5 and 2, C3 is markedly height-invariant, at Location 8 there is an overall tendency for C3 abundances to slightly decrease with height.

*Banded pumice (C4)* shows a slight but systematic tendency to decrease in abundance with distance from vent. However, the largely height-invariant and very low abundances of C3 are seen in all three profiles. Markedly, and similar to Location 5, there is a narrow height interval where C4 increases abruptly to a few percent. At Location 2 this occurs at c.35 – 38% of the total thickness and at Location 8 at c. 55-60% of the total profile thickness.

*Obsidian (C5)* slightly increases in height-averaged abundance with distance from vent (c. 3.8% at Location 5; c. 5.2 % at Location 2; c. 5.8 % at Location 8). In all three profiles, there is also a slight tendency of obsidian to increase in abundance with height.

*Foreign lithics (C6)* have very similar height-averaged abundances of c. 33.9 % and 33.6 % in Locations 5 and 2 but show a much lower height-average of c. 21.5 % in Location 8. It is notable that, if the ash-rich beds are excluded, the value of the height-averaged abundance of C6 clasts at Location 8 amounts to c. 32 % and thus similar to the values for Locations 5 and 2. At Locations 5 and 2, C6 has the highest abundances (>40 %) in the basal part of the profile, then decreases upwards and tends to become more height-invariant in the upper half of the profile. At Location 8, very high values of >40 % as at Locations 5 and 2 do not occur. Instead, there is strong variation with height. Notably, the fines-poor coarse-ash- to lapilli-dominated samples show relatively height-invariant values of C6 clasts of c. 30 %, while the ash-rich beds typically have significantly lower abundances of between c. 4 and 12 %. Comparing the three different lithic groups shows that ‘shallow’ lithics invariably dominate the lithic components of all three profiles (Figure, 4.27). ‘Intermediate lithics’ are extremely rare in profiles 5 and 2 and do not occur at Location 8. ‘Deep’ lithics have low abundances of 3 to 10 % in all profiles. However, there is a particular height in all three profiles where the abundances of ‘deep’ lithics show minimum values. At Location 5 this occurs at 18 – 25 % of the total deposit thickness, at Location 2 at 38 – 42 % of the total thickness and at Location 8 at 54 – 60 % of the total thickness.



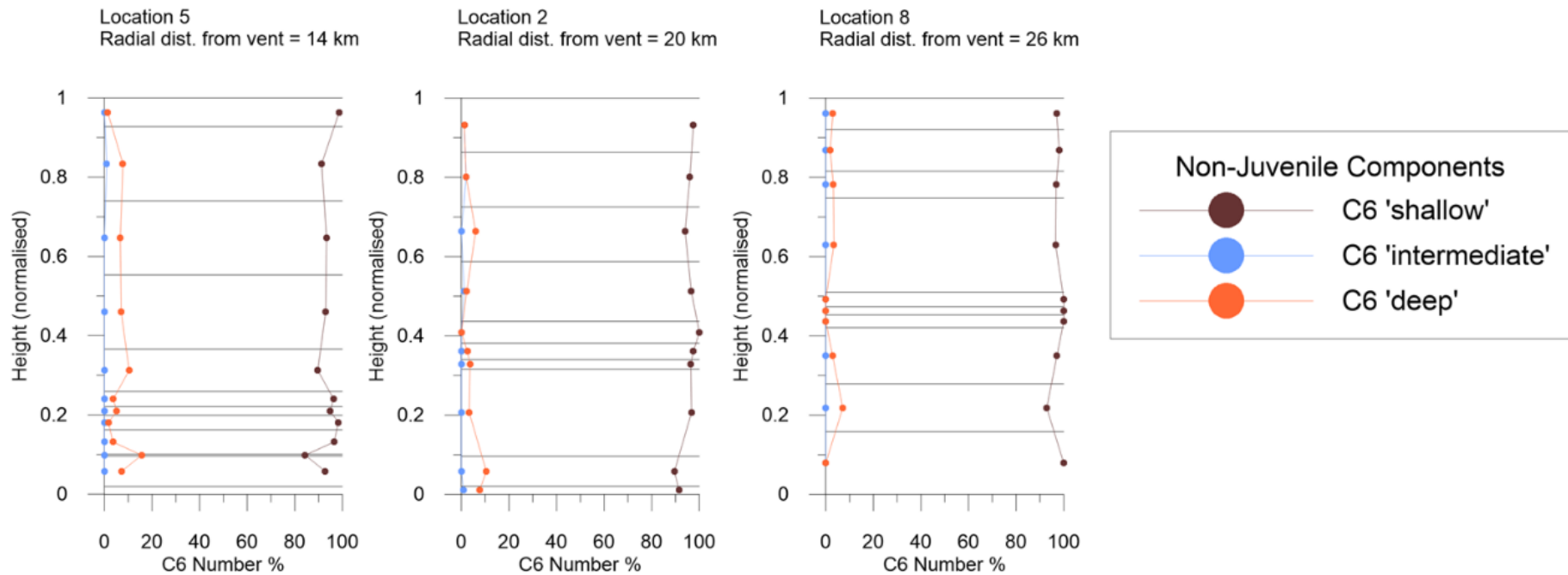


Figure 4.27 Vertical graphs displaying vertical variations in the 1 phi Non-Juvenile lithic components (normalised to 100) for Locations 5, 2, 3, and 8 plotted against normalised vertical height. True height for Locations 5, 2, 3, and 8 are 234, 146, 31 and 19 cm, respectively. Colours are determined by group, see legend. Black horizontal lines indicate upper boundaries for samples. Note distance from vent in km.

*Free crystals (C7)* have somewhat similar height-averaged abundances at all three locations (c. 29 % at Location 5, c. 30 % at Location 2 and c. 27 % at Location 8). However, while at Locations 5 and 2, the abundance of C7 is relatively height-invariant, Location 8 shows a markedly higher abundance of >30 % in the upper third of the profile.

## **5 Discussion**

### **5.1 Deposit Types of the Y2 Eruption and Their Genesis**

The first comprehensive field study of the Y2 Plinian deposit, which was undertaken by George Walker (Walker, 1981a), outlined the (vertically) relatively monotonous character of the deposit. The monotony of the lapilli-dominated fall sequence, together with its widespread occurrence on land, allowed Walker to derive one of the first comprehensive and high-resolution datasets for Plinian fall deposits based on bulk-deposit data of thickness, maximum pumice and maximum lithic clasts diameters.

Reconnaissance mapping by Talbot et al. (1994) identified and correlated a total of 9 ash-rich lapilli layers and lapilli-bearing ash layers that occur locally within the proximal to medial, E – NE part of the Y2 dispersal. The lower three of these beds occur together. They are characterized by the occurrence of accretionary lapilli as well as by deposit vesiculation and they show systematic thinning and fining trends with distance. Based on these features, Talbot et al. (1994) interpreted these lower beds as the deposits of very low-energy ground-hugging gravity currents that might have derived from the ambient air entraining peripheries of the ascending eruption plume. They also showed the upper seven ash beds occur discontinuously with a maximum number of seven of these upper ashes found at one location. Furthermore, the thickness of each bed is characteristically uniform with distance from vent. Talbot et al. (1994) interpreted the formation of the upper ash beds as rain-flush beds.

In the following, the reported data on the lapilli-dominated fall deposits, local rain-flush beds and low-energy dilute gravity current deposits are discussed along with previous information to interpret their genesis.

### 5.1.1 Timescales and Conditions of Pyroclasts Transport and Settling

For the later discussion of the eruption dynamics of the Y2 eruption phase, it is meaningful to estimate and contrast three different timescales that are relevant for the deposit genesis: the total eruption duration  $T_{tot}$ , the duration of pyroclasts transport in the umbrella cloud from the point of neutral buoyancy to the radial distance above studied tephra sections  $T_{umb}$ ; and the duration of pyroclasts settling to the ground  $T_{sett}$ . Previous estimates of deposit mass (c.  $1.12 \times 10^{15}$  g) and mass eruption rate (c.  $10^7$  kg/s) allow for approximation of a  $T_{tot}$  of around 11 hours (Walker, 1981a; Wilson & Walker; 1985; it should be noted that durations three times that long have been suggested following a different deposit mass estimate).

Minima of  $T_{umb}$  can be estimated as the ratio of the horizontal distance between vent and tephra section and the stratospheric windspeed at the level of neutral buoyancy. Using the existing estimate of the eruption column height of Y2 of c. 30 km and a speed of 30 m/s (Wilson et al., 1978) gives the following values:  $T_{umb}$  (Loc\_5 at 14 km) = 7.8 min;  $T_{umb}$  (Loc\_2 at 20 km) = 11.1 min;  $T_{umb}$  (Loc\_8 at 26 km) = 14.4 min; and  $T_{umb}$  (Loc\_3 at 41 km) = 22.7 min. These values should be regarded and inter-compared with another as minima, because the slow spreading of the umbrella cloud in a direction oblique to the dispersal axis (and thus from faster central to slower peripheral umbrella cloud regions) is not considered in the above estimate. Regardless, it is important to note that these durations are brief and a small fraction of the total eruption duration.

In order to compare these two timescales with the typical time scale of pyroclast settling, the radial distances from vent to the sample locations, where Walker measured a bulk sample median particle diameter, were digitized from the map in Fig. 7b of Walker (1981a). A bulk sample terminal velocity  $\omega$  was obtained for each sample site using the relationship of Dellino et al. (2005):

$$\omega = \frac{1.2065\mu(d^3g(\rho_s-\rho)\rho\Psi^{1.6}/\mu^2)^{0.5206}}{d\rho}, \quad (\text{Eqn. 3})$$

where  $\mu$  is the dynamic viscosity of air,  $d$  is here taken as the median particle diameter,  $g$  is acceleration due to gravity,  $\rho_s$  is particle-size variant average pyroclast density,  $\rho$  is the density of air, and  $\Psi$  is a non-dimensional shape factor here taken as 0.5. Values of  $\rho_s$  are

obtained from the well-constrained density measurements of a sample of layer 2A of the Taupo ignimbrite reported in Lube et al. (2015).

Data of  $\omega$  against radial distance from vent  $r$  collapse remarkably well onto a universal curve (Figure, 5.1). A best-fit powerlaw fitted to the data is given by the following equality ( $R^2 = 0.925$ ):

$$\omega = 19.493r^{-0.503}. \quad (\text{Eqn. 4})$$

The particle settling duration  $T_{sett}$  can be obtained as the ratio of the plume height and the terminal fall velocity. For the four sample locations the following durations result:  $T_{sett}$  (*Loc\_5 at 14 km*) = 96.7 min;  $T_{sett}$  (*Loc\_2 at 20 km*) = 115.7 min;  $T_{sett}$  (*Loc\_8 at 26 km*) = 132.1 min; and  $T_{sett}$  (*Loc\_3 at 41 km*) = 166.1 min. This shows that for the locations considered here, the typical pyroclasts settling time  $T_{sett}$  is approximately an order of magnitude larger than the typical timescale of umbrella cloud transport  $T_{umb}$  and, thus,  $T_{set}$  is more significant for the timescales of deposition.

On a side note it is interesting to compare terminal fall velocities of Y2 and Y5 at similar radial distances from vent. For instance, at  $r = 100$  km the median terminal fall velocity for Y2 is c. 1.9 m/s, while for Y5 it is as high as c. 5 m/s. These differences related to the strong differences in median pyroclasts diameter at same  $r$  highlights to extraordinary ‘dispersive power’ of the considerably more energetic Y5 eruption stage as originally proposed by Walker (1980).

When plotting the terminal fall velocities for all tephra samples from Locations 5, 2, 8 and 3 into Figure 5.1 the following observations are made: in all sections but section 8 there is a spread of  $\omega$  of c. 1 m/s displaying the vertical variability of the median particle diameter (and to a lesser extend the effect of decreasing average solids density with increasing grain-size); the highest  $\omega$  values are close to those obtained from the samples of Walker (1981a) suggesting that what he really systematically sampled was a bulk sample of the coarsest proportion of each section; at Location 8, only half of the vertical samples show  $\omega$  values close to those of the bulk sample of Walker (c. 3.9 m/s). The other half has  $\omega$  values as low as 1 m/s and thus about a quarter of that of the bulk samples. These ‘slowly settled’ samples correspond to the lapilli-bearing ash beds (three of Talbot’s rain-flush beds) and ash-rich lapilli layers.

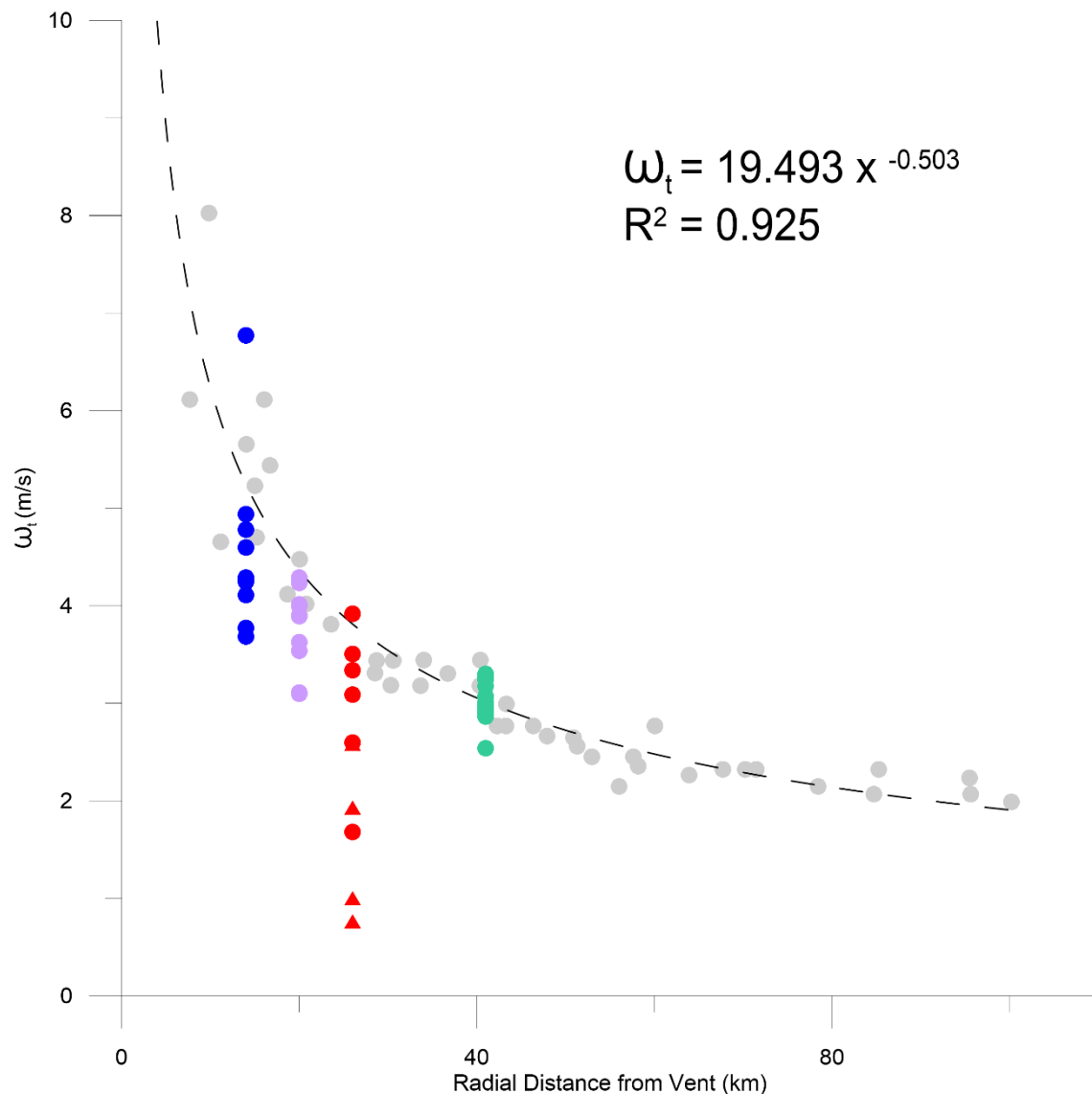


*Figure 5.1 Graph displaying terminal fall velocities ( $\omega$ ) with distance from vent (km). Grey points are terminal velocities ( $\omega$ ) calculated using points from Walker (1981a), blue points are  $\omega$  values from Location 5, purple points are  $\omega$  values from Location 2, red points are  $\omega$  values from lapilli samples from Location 8, red triangles are  $\omega$  values for ash beds at Location 8, green points are  $\omega$  values for Location 3.*

These calculations pose a fundamental question on how fine ash and coarse ash to lapilli particles settle to deposit synchronously on the ground. While the vast majority of samples show grain-size distributions that are dominated by a main mode of coarse ash to lapilli (Figure, 4.6), there is a considerably long fine-tail of very fine ash and dust. Given the caution taken during careful box-sampling, sample transport and wet-sieving procedures it is unlikely that the ash content is explained by sample handling. However, there is a systematic decrease in ash content with radial distance from vent and its virtual absence in the distal Location 3 at 41 km from vent.

To interrogate the conditions of synchronous lapilli, coarse-ash and fine-ash deposition, Figure 5.2 compares graphs of terminal fall velocity against grain-size for an fine-ash poor coarse-ash to lapilli-dominated sample that is characteristic for the majority of Y2 samples (sample 2 of Location 8), a lapilli-bearing fine-ash layer (sample 5 of Location 8) and the dilute gravity current deposit (sample 9 of Location 8). For the calculation of the terminal fall velocity for each sample and each full phi grain-size class, a bulk phi-size class-averaged particle density is computed using the componentry abundance and their mean componentry class particle densities. The fines-poor sample 2 shows an overall decrease in terminal fall velocity with decreasing grain-size.

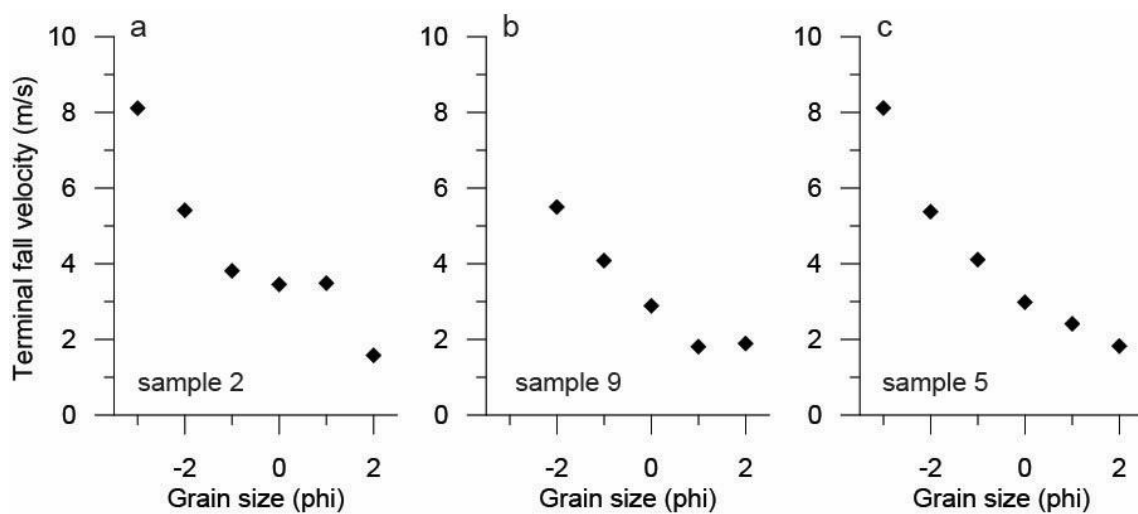


Figure 5.2 Graphs of terminal fall velocity against grain size for selected beds from Location 8. A) fine ash-poor bed, B) coarse ash bed, C) lapilli dominated bed

However, there is a broad plateau of approximately constant terminal fall velocities of c. 3.5–3.8 m/s that occurs over three full-phi size classes (that is -1, 0 and 1 phi; Figure 5.2a). This grainsize range corresponds to the dominant size classes of the sample that constitute its main mode. This size range also includes the main modes of the low-density components and high-density components and shows that low- and high-density particles settled in aerodynamic equilibrium. For the strongly bimodal sample 9, terminal fall velocity monotonically declines from -2 to 1 phi, but shows a plateau of approximately constant velocity for the 1 and 2 phi size classes (Figure 5.2b). These medium- to coarse ash sizes constitute the coarser-grained of the two modes of the sample. This observation is consistent with the interpretation of a fully turbulent and density-stratified gravity current where settling of the large particles would occur in aerodynamic equilibrium. In contrast, for the

bimodal ash-rich layer 5, the terminal fall velocity decreases monotonically with decreasing grain-size and there is no evidence for aerodynamic equilibrium in the settling of lapilli- and coarse ash-sized particles (Figure 5.2c).

A possible explanation for the high fine-ash content of the coarse-ash- to lapilli dominated fall in proximal to medial reaches is that the coarse particles settled out of the umbrella cloud and fell through lower atmospheric levels that were charged with a large proportion of fine ash originating from the vent and/or outer margin of the ascending eruption column. Dilute gravity currents and wind would have dispersed this fine ash for several tens of kilometres. In this situation, the fine ash accumulated as a background sedimentation to the umbrella cloud sedimentation. Under the condition of a moist atmosphere, fine-ash could have adhered to and coated coarse particles settling from the umbrella cloud. If that is the case, there should be a dependence of the surface area of the coarse particles settling from the umbrella cloud and the proportion of very fine ash present in the sample.

To test this idea, the cumulative surface area of all pyroclasts in the -5 to -1 phi grain-size range (making the main mode of the grain-size distributions) per cubic metre was computed from the grain-size distributions of all samples. This normalized surface area of the coarse-ash to lapilli size range,  $A_{SCT}$ , is plotted against the abundance of very fine ash in Figure 5.3.

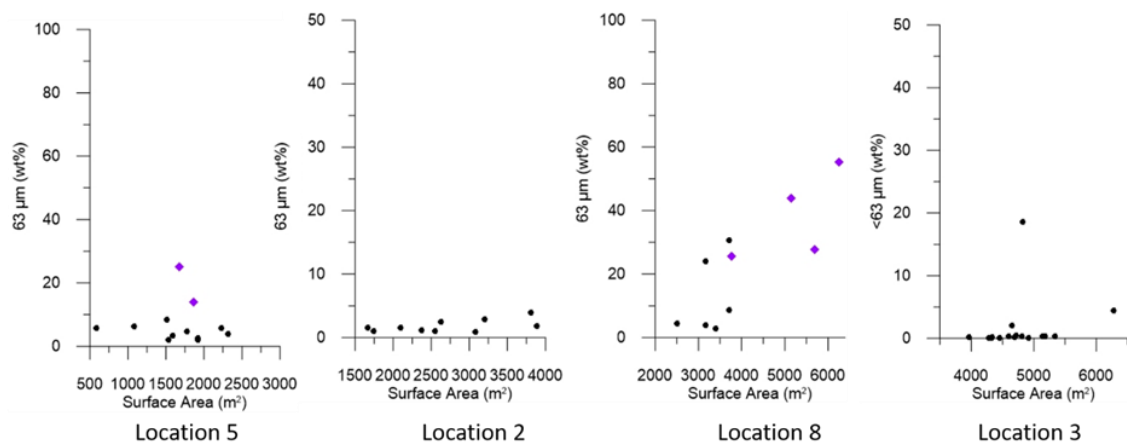
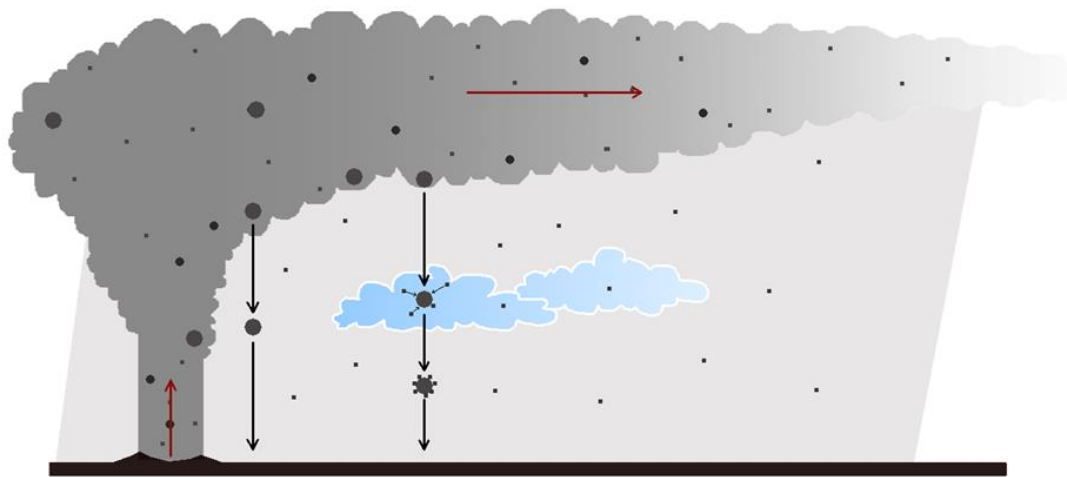


Figure 5.3 Graphs plotting surface area ( $m^2$ ) against  $<63 \mu m$  (weight %) for Locations 5, 2, 8, and 3. Black dots are lapilli samples, purple diamonds are ash samples. Location 5 is 14 km from vent, Location 2 is 20 km from vent, Location 8 is 26 km from vent, Location 3 is 41 km from vent.

This shows that for the majority of Y2 fall samples the amount of very fine ash present in the samples is independent of the surface area of coarse particles. Also, the content of very



fine ash decreases strongly with radial distance from vent. These findings agree with the interpretation that very fine deposits as a background sedimentation from a dusty lower atmosphere (Figure, 5.4). However, the ash-rich samples of Location 8 show a strong positive correlation of the abundance of very fine ash with ASCT (Figure, 5.3). This could indicate that a large proportion of fine ash present in the atmosphere adhered to the surface of large particles during their settling. The presence of a moist atmosphere, if for instance local rain showers or rain clouds were present, would have enhanced this process.



*Figure 5.4 Schematic demonstrating particles settling out of plume (dark grey) through a dusty lower atmosphere (light grey). Particles fall, indicated by arrows, through weather systems (blue clouds) creating a surface for ash to stick to (grey particles). Drawn by S. Tapscott for this thesis.*

## **5.2 Types of Pyroclast of the Y2 and Their Genesis**

At any level in the three studied tephra profiles, the componentry analysis revealed the presence of a wide range of pyroclast textures of juvenile clasts and a variety of petrologically distinct, foreign lithic material. In order to allow for a discussion of the temporally evolving dynamics of the Y2 eruption in Section 5.4, this section aims at using the textural characteristics and the relative abundance of the different component classes to provide an interpretation of their origin and formation. Section 5.2.1 examines the characteristics of the juvenile components to discuss and interpret differences and possible relationships of their formations. This is also reviewing the results of detailed textural studies

reported from other Plinian deposits. Section 5.2.2 provides a discussion of the variety of foreign lithic material present in the Y2 leading to an interpretation of the likely crustal depths of origin of different types of foreign lithics that are seen in the deposits.

### **5.2.1 Characteristics and Formation of Juvenile Component Textures**

Textural studies of juvenile pyroclasts formed during large-magnitude explosive eruptions have highlighted the concurrent deposition of clasts with a variety of macroscopic and microscopic characteristics. In combination with analogue experiments on magma vesiculation and fragmentation, geochemical analysis and theoretical modelling, these characteristics have been used to reconstruct the pyroclasts genesis with regards to:

- Decompression, volatile exsolution, vesiculation and acceleration of magma during its ascent (Sparks, 1978; Kaminski & Jaupart, 1997);
- Vesicle nucleation, bubble coalescence and the development of permeable pathways for pre-fragmentation magma degassing (Klug & Cashman, 1996);
- Development of laterally variable shear, brecciation, microlite crystallization and deformation of the ascending vesiculating magma due to frictional interaction with the conduit walls (Polacci et al, 2001; Shea et al., 2012);
- Strong changes in rheology and conditions of magma fragmentation (Hess & Dingwelt, 1996; Lejeune & Richet, 1995; Mourtada-Bonnefoi & Laporte, 1999); and,
- Post-fragmentation bubble expansion and contraction processes (Houghton et al., 2010; Rotella et al., 2014).

Houghton et al. (2010) presented a first systematic study characterizing different juvenile pyroclast textures in the Taupo 232 CE eruption products and examining their differences associated with the seven dry magmatic and phreatomagmatic eruption stages Y1 to Y7 (Eruption Z). They applied a combination of macroscopic and microscopic textural characterisations and pyroclast density measurements to distinguish five main classes of juvenile pyroclasts: (1) white, microvesicular pumice with dominant equant-shaped bubble shapes; (2) white, microvesicular pumice with dominant elongated bubble geometries, (3) white, coarsely vesicular pumice with dominant equant-shaped bubble geometries; (4) white,

coarsely vesicular pumice showing dominant elongated bubble geometries; and (5) dense (c. 700–2,100 kg/m<sup>3</sup>), grey clasts with sparse and deformed bubbles.

In this study, the occurrence of equant-shaped to elongated vesicle texture in white microvesicular and white coarsely vesicular pumice was also observed. However, due to the characteristically continuous variation of bubble shapes from equant to highly elongated end-members, the first four classes of Houghton et al. (2010) were combined into two readily distinguishable groups of white microvesicular pumice (C1) and white coarsely vesicular pumice (C2). Further, instead of one large group of grey juvenile pyroclasts with a wide range of particle densities, in this study, the ‘grey’ pyroclasts were subdivided into three individual groups. These are: grey, low-density (c. 360–830 kg/m<sup>3</sup>) pumice (C3); intermediate density (c. 800–1,600 kg/m<sup>3</sup>) banded pyroclasts (C4) with bands of white to light grey highly vesiculated, relatively undeformed vesicles alternating with grey bands of strongly deformed, variably vesiculated material and grey bands of relatively dense, vesicle poor glass; and light to dark grey and brown, dense obsidian (C5).

*White pumices* C1 and C2 are the most abundant pyroclasts by volume (together c. 70–80 vol%) and weight (together c. 45–55 wt%) in all of the three studied sections. Overall, and with the exception of the lowermost and uppermost proportions of the tephra sections, C1 is typically five to ten times more abundant (by weight) than C2. Both pumice types were observed to be markedly sparse in microlite content. Microscopic analyses showed that the microvesicular pumice C1 is dominated by small (tens of microns) and overall little-deformed vesicles. Larger bubbles (hundreds of microns) occur, showing deformed bubble walls, but are rare. In comparison, thin sections of C2 clasts showed a markedly larger proportion of large bubbles (hundreds of microns to several millimetres in diameter); small bubbles still occurred but were proportionally fewer; bubble walls were thinner than in C1, strongly deformed and showed contracted shapes. Similar textural characteristics have been described in microvesicular and coarsely vesicular pumices from other Plinian deposits (e.g. Klug & Cashman, 1996; Polacci et al., 2001; and Shea et al., 2010). The general interpretation has been that microvesicular (lowest density) pumice records a less mature bubble vesiculation stage during very rapid magma ascent than coarsely vesicular (second lowest density) pumice at slightly lower ascent speed, where bubble coalescence is more advanced. This interpretation agrees with the observations of reduced bubble wall thicknesses in C2 and also a narrower clast density distribution, and a smaller mean clast

density, in C1 pumices than in C2 pumices (Figure, 4.12). The predominance of C1 pumice with a low degree of bubble coalescence therefore indicates that bubble coalescence occurred shortly before fragmentation, and, as suggested by Houghton et al. (2010), points towards a very rapid overall magma ascent through the conduit.

*'Grey' microlite-rich juvenile clasts:* Thin-section analysis showed that components C3 and C4 have markedly larger abundances of (several microns- to tens of microns-long) microlites than C1 and C2, which gives these clasts a light grey colour. This interpretation agrees with analyses of several other Plinian deposits that contain different proportions of white and grey juvenile pyroclasts populations (e.g. Pallister et al., 1992; Gardner et al., 1998; and Polacci et al., 2001). In these studies, grey microlite-rich juvenile clasts have been described as showing strong shear deformation structures, thick bubble walls, shear-collapsed bubble textures and thus an overall high density. Textural analysis of these dense 'pumices' from the 1991 Mount Pinatubo eruption (Polacci et al., 2001), the 1980 Mount St. Helens eruption (Klug & Cashman, 1994) and the AD 79 eruption of Vesuvius also showed a concurrence of tens of microns- to millimetre-wide domains of relatively undeformed, moderately deformed and strongly deformed vesicles that occur in close proximity to another in planar fabrics. These features have been attributed to strong shear due to the frictional interaction of the foaming magma with the conduit margin, and in particular with shear partitioning into high- and low-shear planes parallel to conduit walls creating the observed clast banding (Polacci et al. 2001).

The above described textural characteristics coincide with those found in microscopic analysis of the intermediate density C4 clasts in Y2 (cf. section 4.3). This also includes the wealth of pumice textures from highly vesiculated to extremely shear-collapsed and thus dense fabrics occurring in immediate contact with another in shear bands. The co-existence of low-density and high-density zones in a single pyroclast and their variable proportions in different C4 clasts explains the intermediate clast densities and their wide range from c. 800–1,600 kg/m<sup>3</sup>. C4 typically makes less than one to a few percent (by weight) of the deposited pyroclast cargo in any one sample. C3, the other grey microlite-rich juvenile pyroclast type, is two- to ten-times more abundant than C4 in Y2. C3 is denser than C1 and C2 (Table 4.1), but considerably lighter than C4, which is well explained by their abundance of moderately-sized, little deformed spherical bubbles of relatively uniform diameter (c. 40-80 microns),

next to larger (hundreds of microns) ovoid-shaped bubbles that are separated by extremely thin bubble walls, and their abundance of (heavy) microlites and larger phenocrysts.

The growth of microlites in grey pumices has been attributed to sudden decompression following the development of permeability in the vesiculating magma (Klug & Cashman, 1994). The presence of microlites in grey pumices have been proposed to aid the nucleation of bubbles, to increase magma viscosity and through hindering bubble coalescence potentially limiting the upper size range of fragmented 'grey magma' (Klug & Cashman, 1994). In fact, C3 clasts show a well-defined unimodal grain-size distribution with a common mode in the 2-4 mm size class and maximum clast sizes not exceeding 16 mm. Because C3 clasts have densities intermediate between low-sheared white pumices and highly sheared C4 clasts, they may represent a proportion of the ascending and foaming magma that is situated inbetween the low-density/low-shearing central conduit region and the highly sheared conduit margin zone. In this region, localized shear would be high enough to allow bubble wall rupture to cause degassing and microlite crystallization, but too low to strongly shear the bubbles (as would occur closer to the conduit walls).

Thin-section analyses of selected *obsidian clasts (C5)* showed a complex internal texture that is not discernable on the macroscopic scale. This revealed the occurrence of irregular shaped millimeters- to centimeters-long schlieren structures composed of clastic glass and crystal fragments and with non-sharp contacts to surrounding obsidian glass proper (Figure, 4.13). Obsidians also contain fracture zones that cut (and postdate the formation of) schlieren and obsidian glass. Similar textures were reported in pyroclastic obsidian from the A.D. 1340 Mono Craters eruptions (Newman et al., 1988; Rust et al, 2004). These textures were attributed to a brittle magma brecciation in contact with the conduit walls, where degassing along the brecciated zone next to the conduit margins is buffered by a sustained vapour flux from the magma and occurs through "highly permeable, brecciated magma along conduit walls" (Rust et al., 2004). They also recognized that there is annealing of magma that flows along the conduit margin.

### A Tentative Conduit Model for the Y2 Eruption

The fine-scaled sampling, grain-size and componentry work and the associated microscopic characterisations on the three Y2 tephra sections provide already classified and grain-size separated pyroclasts material for future quantitative microtextural analyses. This could

include, for instance, measurements of component vesicularity, glass and bubble fabrics and microlite content of the different componentry classes. These analyses will be needed to develop a quantitative conduit model for the Y2 eruption, which has not been the focus of this research. However, in the following, the existing data are combined with current conduit models of Polacci et al. (2001) and Shea et al. (2012) to build a first qualitative and testable framework for a Y2 conduit model.

This scheme focusses on the horizontal variations in the properties of the vesiculating and accelerating magma in the conduit just prior to magma fragmentation. In this region, due to increasing bubble nucleation and growth and friction with the bounding conduit walls, characteristic horizontal velocity (and associated shear) and density gradients result in the non-Newtonian melt-bubble flow as illustrated in Figure 5.5. In terms of velocity, this grades from a fastest, lowest-shear conduit core region, over an adjacent slower, moderate shear region to a lowest velocity, high-shear region that includes an extreme-shear boundary layer in contact with the conduit walls. The horizontal velocity gradient feedbacks with the degree of bubble coalescence (being lower in the faster core than the slower adjacent regions). Due to laterally increasing shear, resulting bubble deformation results in a strong horizontal density gradient, which acts as steepening the buoyancy-controlled (and viscosity-controlled) velocity profile during ascent. The fastest (low-shear), low-density core region underwent late stage nucleation with immature bubble coalescence producing microvesicular 'C1 magma'. Immediately adjacent, in a slower moving and slightly more sheared region, bubble coalescence is more advanced at similar depths. Mild shear-gradients deform bubble walls and enclosing vesicles, producing 'C2 magma'. Following this concept (Figure 5.5), vertical variation in the fragmentation level can account for changing proportions of 'C1 and C2 magma' immediately prior to fragmentation (C1/C2 increasing with decreasing fragmentation level).

Moving closer towards the conduit margin, an even slower region is envisaged where moderate shear localizes into wide shear bands causing the vesiculating magma to develop permeable pathways that cause decompression-induced microlite growth (Klug & Cashman 1994). Microlite growth enhances bubble nucleation, while hindering bubble coalescence creating the ripened 'C3 magma' with thin bubble walls. Even closer to the conduit, shear deformation of bubbles and localization of shear into shear bands dominates magma deformation and produces 'C4 magma' (e.g. Shea et al. 2012). In contact with the conduit

wall, extreme shear is causing magma brecciation and the incorporation of brecciated glass, crystal and country rock fragments into annealing magma that is creating permeable pathways at the conduit wall and, upon fragmentation, C5 obsidian as per the model of Rust et al. (2004).

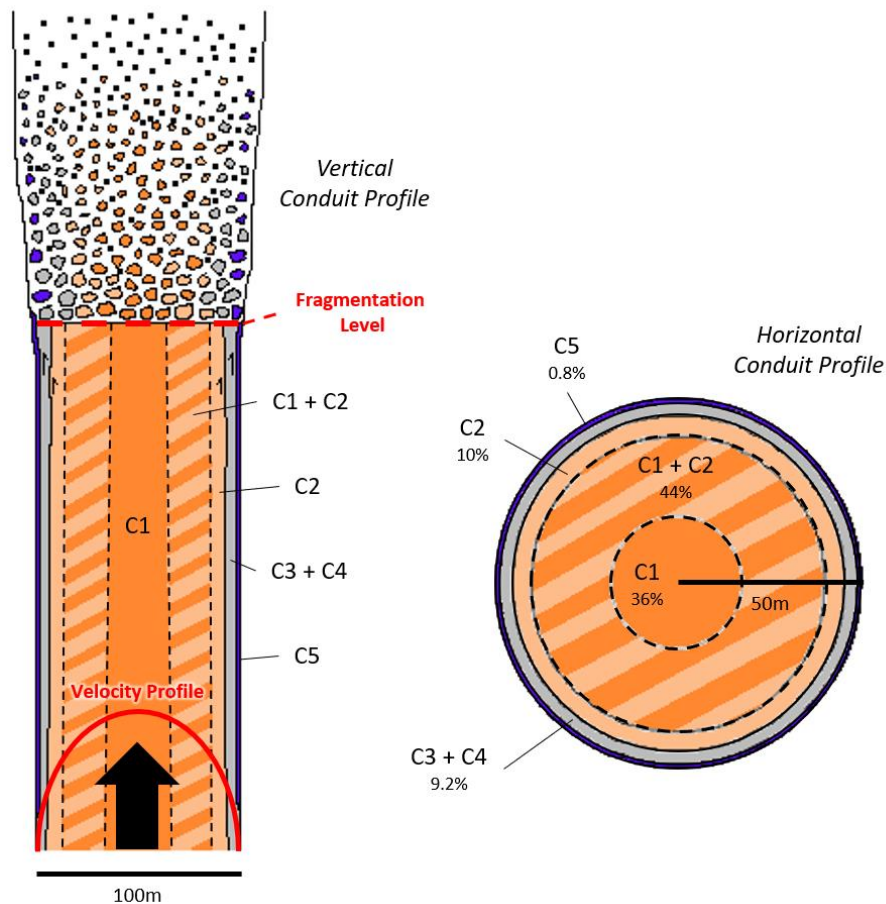


Figure 5.5 Tentative conduit model displaying horizontal density gradient in two views; a vertical profile (left) and a horizontal profile (right) assuming a conduit radius of 50 m. Black arrow indicates magma ascent, red line indicates velocity profile, red dashed line indicates fragmentation level, orange colour indicates C1 region, striped orange and light orange indicate C2 + C2 region, light orange indicates C2 region, grey indicates C3 + C4 region, purple indicates C5 region. Values are the volume of each component/ group within the conduit in percentage. Drawn by S. Tapscott for this thesis.

This tentative (close to fragmentation) conduit model, of linking pyroclasts textures to a horizontal gradient in the density of the variably maturely vesiculated magma that is overprinted by horizontal gradients in shear arising at the magma/conduit wall contact, is inspired by the transient conduit model for the AD79 eruption of Vesuvius (Shea et al., 2012). Under the assumption that this model is valid, the grain-size, componentry and clast

density data for Y2 can be used to estimate the radial extents in the conduit of the proportion of Y2 magma prior to fragmentation that will result in C1 to C5 pyroclasts. For example, the fine ash-poor sample 8 of Location 8 is representative for the typical form of the grain-size distribution and componentry distribution for the majority of analysed Y2 samples. For each juvenile componentry class, the determined total componentry class mass can be combined with the average component class density to derive the volumetric proportions of C1, C2, C3, C4 and C5 'magma'. Assuming that the sample constitutes a representative snapshot of the fragmented magma at a particular time (that is, it has not been significantly altered by particle density grading during transport in the umbrella cloud) the component volume proportions can be converted into two-dimensional area proportions. Considering a cylindrical conduit with a 50 m radius, the little sheared, lowest-density 'C1 magma' would occupy an 18 to 40 m radius central region (varying with the C1/C2 ratio); the second lowest density 'C2 magma' extends out to c. 45 m; the moderately to highly sheared 'C3 and C4 magma' would extend from c. 45 m to c. 49.6 m and shows radially increasing density; while the extremely sheared and brecciating 'C5 magma' that is forming obsidian occupies a 'boundary layer' against the conduit wall, which is only few decimetres wide (Figure, 5.5).

### **5.2.2 Petrological Characteristics and Crustal Depth of Origin of Foreign Pyroclasts.**

The variety of lithic lithologies seen in the Y2 samples offers a 'view' into the complex subsurface geology below the Y2 vent. Through componentry analysis and thin-section microscopy, ten petrologically distinct types of foreign lithics were distinguished and separated into three broad groups based on their estimated depth of origin, i.e. 'shallow', 'intermediate' and 'deep' lithics.

'Shallow' lithics are characterised by an absence of hydrothermal alteration. They constitute the most abundant group (c. 90 – 100 % of all lithics) and are present in all samples. In order of abundance, shallow lithics include: rhyolitic lava (c. 80 %), welded ignimbrites and volcanogenic breccias (c. 10 %), and obsidians and altered pumice (c.10 %). The 'shallow' group is interpreted to be sourced from upper crustal levels of a few hundred metres based on the dominance of rhyolitic lava fragments. These are interpreted here to constitute the same shallow-seated lava dome rocks found as lithics in the Taupo ignimbrite (Cole et al, 1998). The next most abundant 'shallow' lithics lithology constitute welded ignimbrite fragments that are similar in characteristics to those identified and linked to the Whakamaru



Formation by Cole et al. (1998). Also found 'Brown Ignimbrite' lithics can be correlated to the lowest member of the Waiora Formation (Cole et al. 1998).

'Intermediate' lithics constitute the least abundant group (c. 1 % or less) and include grey hydrothermally unaltered lacustrine sediments of the Huka Formation and hydrothermally altered green sandstone, quartzite and altered andesite. Foreign lithics of the 'intermediate' group are estimated to originate from depths between c. 400 m and c. 1.5 km. The lower depth boundary is based on the typical depths of the hydrothermally unaltered lacustrine sediments of the Huka Formation (that were found very sparsely in Y2) and which acts as the cap rock for the hydrothermal fields like those near Wairakei and Tauhara. The Huka Formation was deposited prior to, or immediately after, the 25.5 ka Oruanui eruption when the Taupo-Reporoa basin was occupied by 'Lake Huka' (Manville & Wilson, 2004; Barker et al., 2020). The estimated lower boundary for 'intermediate' lithics of c. 1,500 m origin depths of the hydrothermally altered sediments and altered andesites is estimated based on the presence of altered minerals. The green hydrothermally altered sediments are interpreted to be coloured due to the presence of either epidote, chlorite or actinolite, and are given an inferred depth of at least c.1.5 km corresponding to the c. 250 – 300°C temperature needed in pressurised hydrothermal systems to produce these minerals (Walshe, 1986; Pers. Comm., Colin Wilson 11/08/2020). However, the extremely low abundance of 'intermediate' lithics in Y2 makes it unlikely to envisage an active or old hydrothermal field below the Y2 vent. Instead, these lithics are here interpreted as being accidentally incorporated from the overlying deposits, most likely those related to the Oruanui eruption, which dredged up a large portion of green hydrothermally altered clasts and andesites. Following this interpretation, 'intermediate' lithics are therefore sourced from shallow depths and do not represent wall rock that became incorporated due to the rupture of a hydrothermal field during the Y2 eruptive episode.

The 'deep' lithic fraction accounts for only 2 % of the overall lithic fraction and is comprised of two types of microdiorites (cf. Section 4.3). The 'deep' lithic group is here estimated to encompass a depth range of c. 1.5 km to c. 5 km. The poorly defined upper depth boundary is based on the absence of hydrothermal alteration. The estimate of the lower depth boundary is that of the currently inferred approximate upper boundary of the rhyolitic crystal mush system at Taupo (Brown et al., 1998; Barker et al., 2015; Allan et al., 2017). The

incorporation of these plutonic lithic fragments is here interpreted as the result of excavation of a pathway for the rising magma from the mush zone towards the surface.

### **5.3 Chronostratigraphic Markers of Synchronous Deposition in Plinian Fall Deposits**

The identification of chronostratigraphic time markers in Plinian fall deposits can provide an important tool for the reconstruction of the temporally evolving eruption dynamics and the associated temporally evolving hazard footprints. In computational plume models, such time markers could provide real-world testbeds for the benchmarking and validation of hazard models, such that they can be deployed confidently for public safety.

For some plinian deposits, abrupt or transient vertical changes in pyroclasts composition associated with the withdrawal of magma from chemically zoned magma reservoirs have provided such time markers (eg. Hildreth, 1983; Eichelberger, 1980; Druitt & Bacon, 1988). This has allowed ‘timing’ different stages of Plinian eruptions, including those associated with the formation of hazardous pyroclastic density currents (e.g Fierstein & Wilson, 2005). However, many Plinian deposits do not provide such obvious geochemical time correlatives and are instead characterized by an overall vertical monotony. The Y2 is an example of such a monotonous plinian deposit.

In this research, vertical changes in the proportion of different pyroclast types were quantified through fine-scaled and continuous box-sampling and subsequent point-counting of three Y2 tephra sections. Interrogation of the componentry datasets shows that, in all three tephra profiles, there is a sudden increase over a narrow height-interval in the otherwise monotonously low-abundant C4 component (Figure, 4.25). In all three sections, this spike in C4 pyroclasts occurs synchronous with the position of the local maximum of the ratio of microvesicular and macrovesicular pumice C1/C2 (Figure 4.26), and the local minima of the abundance of ‘deep’ lithics (Figure, 4.27). The vertical correspondence of these three parameters allows for the unambiguous correlation across the analyzed tephra sections. Furthermore, this shows that the Y2 eruption can be subdivided into two time intervals: a first phase when the abundance of ‘deep’ lithics is decreased and when the ratio of microvesicular pumice over macrovesicular increased; and a second phase of opposite trends.

The vertical position of this componentry-based chronostratigraphic marker occurs at different absolute and relative heights in the three tephra section: at c. 69 cm (c. 25 % of total thickness) at Location 5; at c. 60 cm (c. 40 % of total thickness) at Location 2; and at c. 10 cm (c. 50 % of total thickness) at Location 8 (Figure, 5.6a). In general, a decrease of the absolute height of any chronostratigraphic marker with increasing radial distance from vent (that is from Location 5, over Location 2 to Location 8) is expected. However, because of the similar deposition onset at all three locations (see section 5.1 above for an approximation that deposition onset should only differ by a few tens of minutes) and the similar deposition cessation (marked by the overlying Y3 tephra without indication of a pronounced time gap), the relative (normalized) height of chronostratigraphic markers should be approximately similar and invariant with radial distance from vent. Figure 5.6b shows that this is not the case.

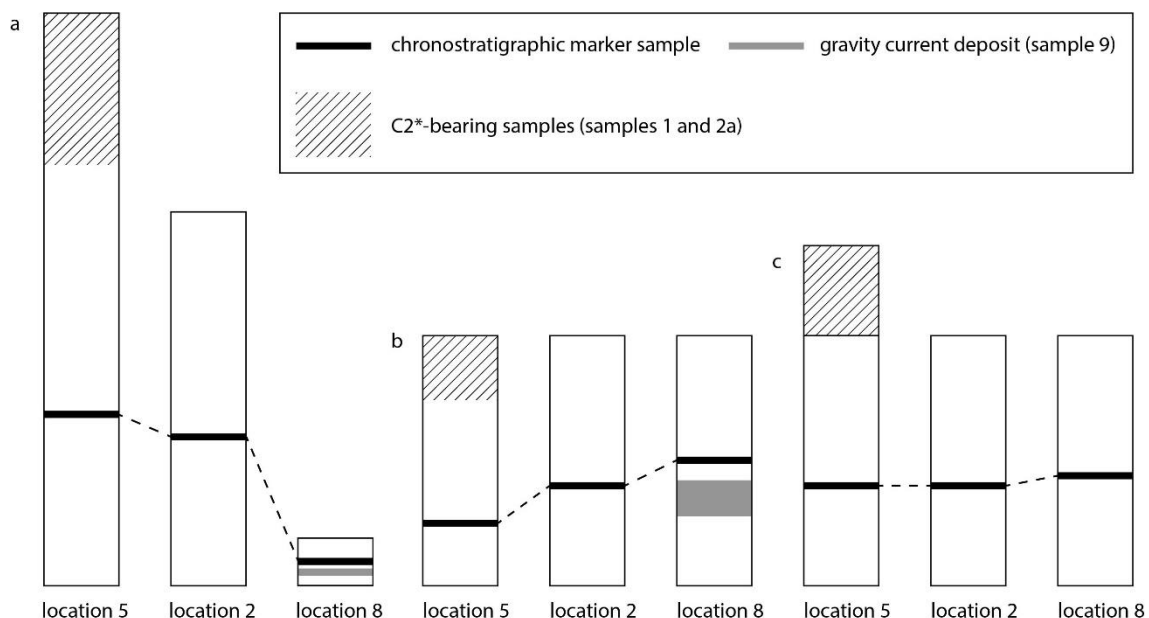


Figure 5.6 Vertical profiles of Locations 5, 2 and 8 showing chronostratigraphic markers. A) true height, B) normalised height and C) re-calculated normalised height. Drawn by G. Lube for this thesis.

The vertical componentry analysis also revealed the upper two samples (that is the upper c. 61 cm) of Location 5 show the occurrence, and increase with height, of transparent and thick bubble-walled pumice. This component (C2\*) is completely absent from the lower profile and does not occur at all at Locations 2 and 8. Further, the upper 61 cm of Location 5 show C1/C2 ratios smaller than 1. Elsewhere at Location 5 and at Locations 2 and 8 above the chronostratigraphic marker, C1/C2 always takes values above 1 (Figure, 4.26). This suggests

there are no time correlatives for the upper 61 cm of the tephra profile of Location 5 at Locations 2 and 8. Different explanations for this finding include an overall change in wind direction from WSW to W during eruption progression as also indicated by George Walker's isopleths data (Walker 1981a) and/or limited downwind advection of pyroclasts in the umbrella cloud during the late stage of the eruption. Subtraction the upper 61 cm from Location 5 shows that the recalculated relative (normalized) position of the C4-spike (also the C1/C2 maximum and 'deep' lithic minimum) occurs at 40 % of the total thickness in agreement with Location 2 (Figure 5.6c).

Sample 9 of Location 8 constitutes a poorly sorted pumice-bearing ash layer. This layer corresponds to the narrow, laterally thinning and vesiculated ash bed identified by Talbot et al. (1994), which they explained as the deposit of dilute ground-hugging gravity current that propagated in a roughly easterly direction from the vent. Adapting this interpretation, and because the relatively fast deposition of such a gravity current (several minutes in comparison to several hours for the fall sequence) is a different process to the tephra accumulation by fall from the umbrella cloud, the thickness of the gravity current deposit has been subtracted from the re-calculated relative (normalized) tephra profile of Location 8 in Figure 5.6c. This shows that the recalculated relative (normalized) position of the C4-spike (also the C1/C2 maximum and 'deep' lithic minimum) occurs at c. 45 % of the total thickness. The very slight difference between the positions of the chronostratigraphic marker (that is c. 40 % of total thickness at Locations 5 and 2 vs. c. 45 % of total thickness at Location 8) is readily explained with minor differences in local sedimentation rates of coarse ash- to lapilli dominated fall and ash-rich beds that occur at Location 8.

## **5.4 Y2 Eruption Evolution**

The here reported data is used to reconstruct the c. 11 hour-long Y2 eruption. After development of the c. 30 km high plume, the umbrella cloud was initially advected by westerly-southwesterly stratospheric winds (Wilson et al., 1978; Wilson & Walker, 1985) passing the most distal Location 3 less than half an hour after umbrella cloud advection commenced. After umbrella cloud overpassing, particle settling on the ground would have started around 1.5 hours later at Location 5 (most proximal location) and 2 hours later at Location 3 (most distal location).

The earliest deposited pyroclasts are dominated by C2 pumice, as well as shallow lithics, and show the highest abundances of deep lithics. This suggests that the Y2 magma, after excavating a pathway through the plutonic roof of the mush reservoir, ascended relatively unhindered through mid- and upper crustal levels. Decompression-induced magma vesiculation led to its accelerated ascent and (initially) strong vesicle coalescence (low C1/C2). Over the next c. 2 – 3 hours, C1/C2 increases suggesting that fast magma ascent led to fragmentation of dominantly prematurely coalesced magma, which is interpreted with very fast magma ascent and feeding of relatively steady and strong plume.

Approximately 3-4 hours into deposition there is an increase in the C4 component which has here been identified as a chronostratigraphic marker. The discernible increase in C4 components suggests increased shear of the foaming magma with the conduit walls, which is possibly related to high magma ascent rates. After that, C1/C2 ratios remain significantly larger than 1 for around 5-6 hours suggesting continuous fast magma ascent, fragmentation and feeding of a relatively steady Plinian plume. The upper c. 61 cm of the tephra profile at Location 5 represents approximately the last 1-2 hours of the eruption and is characterised by the presence of thick bubble walled transparent pumice clasts (C2\*). The presence of these clasts in the upper portion of Location 5, and their absence from Locations 2 and 8 suggests a change in wind direction from WSW to W winds as independently proposed by Wilson and Walker (1985) based on full deposit plume dispersal data.

The presence and temporary increase of the C2\* component is speculated to mark a slight but progressive decline in volatile content of the rising magma towards the end of the eruption resulting in a decrease in magma ascent rate. This interpretation is supported by a final strong decline in the C1/C2 ratio showing that the fragmenting magma 'had time' to strongly coalesce rather than fragmenting prematurely as suggested by the high C1/C2 ratios prior to that time. At this point, in combination with volatile loss, the plume may have started to decrease in height and power limiting the distal and lateral dispersal of the plume. In the studied tephra section, the phreatoplinian Y3 deposit overlies Y2 conformably without evidence for any significant time break. This confirms the earlier interpretation of Wilson & Walker (1985) that entry of water into the vent and the onset of eruption stage Y3 would have occurred immediately after the end of the Y2 eruption. From this study, there is no evidence that the large Plinian Y2 eruption was interrupted at any time, or that it significantly changed in eruption power, before the final couple of hours. Earlier identified ash beds at

the NE fringes of the Y2 dispersal (Talbot et al., 1994) are here confirmed to represent deposits of low-energy gravity currents and background sedimentation of very fine ash that is dispersed (likely by wind) from the vent for several tens of kilometres eastwards. Atmospheric moisture likely aided adhering of this fine (atmospheric) ash onto coarse ash and lapilli that were settling continuously from the stratospheric umbrella cloud and through this ash.

## 6 Summary and Conclusions

In this research, fine-scaled, continuous sampling of three tephra sections of the Y2 Plinian eruption and subsequent sample analyses via grain-size, componentry and clast density measurements were conducted to investigate vertical and lateral variations in tephra deposition. In combination with microscopic analysis of juvenile pyroclast textures and petrographic analysis of foreign lithic components, this research tried to decipher the characteristics and temporally variable conditions of magma ascent in the upper conduit leading to fragmentation. Further, the dataset was interrogated as to whether seemingly monotonous plinian fall deposits allow definition of syn-eruption chronostratigraphic time markers, which could aid in the interpretation of such deposits and in the validation of computational hazard models.

The main results of this research can be summarised as follows:

- Grain-size analyses showed that all samples, except for those from the distal tephra profile 3 at 41 km, are unusually poorly sorted for Plinian fall deposits. This poor sorting is due to the occurrence of a long fine-tail of fine and very fine ash. The ash content decreases strongly with radial distance from vent and increases also at the NE fringes of the deposit. This ash content has been attributed to a background sedimentation from an ash-laden atmosphere that occurs synchronous to particle settling from the umbrella cloud in the stratosphere. The ash-laden atmosphere is interpreted as dust produced at the vent and from the margin of the plume and is transported by low-level winds and as gravity currents for tens of kilometres. The production of fine ash at vent and its advection in the lower atmosphere into areas that may not be directly underneath the Plinian fall dispersal may need attention in hazard planning.
- The juvenile components of the Y2 eruption could be grouped into five distinctive textural classes. These are white, microlite-poor, microvesicular pumice (C1); white, microlite-poor coarsely vesicular pumice (C2); grey, microlite-rich macrovesicular

pumice (C3); grey, microlite-rich banded pumice (C4); and pyroclastic obsidian clasts (C5);

- Microtextural analysis and clast density analysis showed that these componentry classes show a systematic increase in clast density and increase in shear-deformed bubbles and glass from C1 to C5.
- A tentative conduit model for the time immediately prior to magma fragmentation, and using the framework of Shea et al. (2012), was developed to explain these juvenile pyroclast textures in context of strong horizontal gradients in magma density, magma rise velocity and shear arising from magma-wall rock interaction.
- In combination with the componentry and grain-size data, the tentative model was used to estimate the radial extents of the variably vesiculated and variably shear-deformed proportions of the magma. This suggests that the lightest and most vesiculated, fast rising central proportion of the magma occupied around 90% of the conduit cross-section with the remainder (a few meters in case of a 50 m conduit) being composed of progressively denser and intensely shear-deformed magma.
- Both the grey low-density pumices (C3) and grey, banded, intermediate-density pumices (C4) are characterised by an abundance of microlites and broader density distributions caused by viscous dissipation near the conduit margin as a result of increased shearing and degassing.
- Textural analysis of pyroclastic obsidian clasts that mark the outermost ‘conduit facies’ showed evidence for brittle magma brecciation, incorporation of clastic glass and crystal fragments and melt annealing within a few decimetre-wide boundary layer of the melt towards the conduit wall likely associated with the development of permeability for magma degassing.
- Identification and distinction of ten different types of foreign lithic lithologies and broad estimates of their likely depth of origin allowed reconstruction of processes of initial magma migration to the surface and vent and conduit excavation. This showed that deep excavation of plutonic country rock above the mush magma reservoir occurred strongly during onset of the eruption, but rapidly declined thereafter.



Significant wall rock excavation continued throughout the eruption but was strongly limited to the upper few hundred metres of the conduit. Wall rock from intermediate depths is markedly absent from the fall deposit suggesting relatively mild magma-conduit interaction during slower magma ascents in the lower c. 5 km.

- The componentry analysis allowed identification of a chronostratigraphic marker based on multiple componentry characteristics. From this the reconstruction of time isochrones of tephra deposition across the three tephra sections could be used to recreate the laterally variable deposition from the plume axis towards its margin. This also allowed estimating durations of different stages of the Y2 eruption. This information of temporally evolving tephra deposition on the ground and its variation with radial distance from the vent will be useful to inform spatially variable hazard impacts and to help improve hazard mitigation strategies.
- The chronostratigraphic markers can be used in future computational studies as a real-world test for the validation of plume and ash-dispersal models. For instance, in multiphase plume models that simulate Lagrangian tracer particles the time markers can be used to validate complex processes of plume expansion in a crosswind and time-variant settling of pyroclasts from umbrella clouds.

Some of the field and laboratory work conducted in this research project (e.g. the fine-scaled sampling, sieving, clast grouping into componentry classes, density analysis and thin section preparation) now allow for more detailed further investigations to add more complexity to the understanding of the Y2 eruption and large Plinian eruptions elsewhere. Suggestions for future research in this regard include:

- quantitative textural analysis on the already prepared componentry samples to constrain parameters such as bubble number density, three-dimensional vesicle fabrics and microlite abundances and size distributions to test and further constrain the suggested conduit model.
- Geochemical analysis of glass volatiles and microlites to add complexity to the timescales of magma vesiculation, degassing and fragmentation during the Y2 eruption. Results of such work could inform the input and boundary conditions of numerical plume models.

Other aspects of future research avenues arising from this research include: the development of a more complete dataset of field locations parallel and perpendicular to the deposit axis to better quantify the lateral plume dispersal as a function of time; and further mineralogical analyses regarding the composition of the lithic components to more accurately constrain depths of origin of excavated country rock to add complexity to the dynamics of magma rising before the onset of potentially catastrophic super-volcano eruptions.

## References

- Allan, A.S.R., Barker, S.J., Millet, M-A., Morgan, D.J., Rooyakkers, S.J., Schipper, C.I., & Wilson, C.J.N. (2017). A cascade of magmatic events during the assembly and eruption of a super-sized magma body. *Contributions to Mineralogy and Petrology*, 172(49), 1–34.
- Baines, P. G., & Sparks, R. S. J. (2005). Dynamics of giant volcanic ash clouds from supervolcanic eruptions. *Geophysical Research Letters*, 32(24).
- Bao, K., Wang, G., Lu, X., & McLaughlin, N.B. (2011). A potential flood hazard caused by Tianchi volcano eruption in Changbai Mountain, Northeast China. *Journal of Mountain Science*, 8(5), 677.
- Barker, S.J., Wilson, C.J.N., Allan, A.S.R., & Schipper, C.I. (2015). Fine-scale temporal recovery, reconstruction and evolution of a post-supereruption magmatic system: Taupo (New Zealand). *Contributions to Mineralogy and Petrology*, 170(5), 1–40.
- Barker, S. J., Wilson, C. J., Morgan, D. J., & Rowland, J. V. (2016). Rapid priming, accumulation, and recharge of magma driving recent eruptions at a hyperactive caldera volcano. *Geology*, 44(4), 323-326.
- Barker, S. J., Van Eaton, A. R., Mastin, L. G., Wilson, C. J. N., Thompson, M. A., Wilson, T. M., ... & Renwick, J. A. (2019). Modeling ash dispersal from future eruptions of Taupo supervolcano. *Geochemistry, Geophysics, Geosystems*, 20(7), 3375-3401.
- Barker, S. J., Rowe, M. C., Wilson, C. J., Gamble, J. A., Rooyakkers, S. M., Wysoczanski, R. J., ... & Kenworthy, C. C. (2020). What lies beneath? Reconstructing the primitive magmas fueling voluminous silicic volcanism using olivine-hosted melt inclusions. *Geology*, 48(5), 504-508.
- Barker, S. J., Wilson, C. J., Illsley-Kemp, F., Leonard, G. S., Mestel, E. R., Mauriohooho, K., & Charlier, B. L. (2020). Taupō: an overview of New Zealand's youngest supervolcano. *New Zealand Journal of Geology and Geophysics*, 1-27.
- Bebbington, M.S. (2020). Temporal-volume probabilistic hazard model for a supervolcano: Taupo, New Zealand. *Earth and Planetary Science Letters*, 536, 116–141.
- Biasse, S., Scaini, C., Bonadonna, C., Folch, A., Smith, K., & Höskuldsson, A. (2014). A multi-scale risk assessment for tephra fallout and airborne concentration from multiple Icelandic volcanoes: Part 1 hazard assessment. *Natural Hazards and Earth System Sciences*, 14(8), 2265–2287.
- Blott, S.J., & Pye, K. (2001). GRADISTAT: A grain size distribution and statistics package for the analysis of unconsolidated sediments. *Earth Surface Processes and Landforms*, 26(11), 1237–1248.

- Bonadonna, C., & Houghton, B. F. (2005). Total grain-size distribution and volume of tephra-fall deposits. *Bulletin of Volcanology*, 67(5), 441-456.
- Bonadonna, C., Folch, A., Loughlin, S., & Puempel, H. (2012). Future developments in modelling and monitoring of volcanic ash clouds: Outcomes from the first IAVCEI-WMO workshop on Ash Dispersal Forecast and Civil Aviation. *Bulletin of Volcanology*, 74(1), 1–10.
- Bonadonna, C., Costa, A., Folch, A., & Koyaguchi, T. (2015). Tephra dispersal and sedimentation. In H. Sigurdsson, B.F. Houghton, & S. McNutt (Eds.), *Encyclopedia of Volcanoes* (2nd ed., pp. 587–597). New York, NY: Academic Press.
- Breard, E.C., Lube, G., Jones, J.R., Dufek, J., Cronin, S.J., Valentine, G.A., & Moebis, A. (2016). Coupling of turbulent and non-turbulent flow regimes within pyroclastic density currents. *Nature Geoscience*, 9(10), 767–771.
- Briggs, N.D. (1976a). Recognition and correlation of subdivisions within the Whakamaru Ignimbrite, central North Island, New Zealand. *New Zealand Journal of Geology and Geophysics*, 19(4), 463–501.
- Briggs, N.D. (1976b). Welding and crystallisation zonation in Whakamaru ignimbrite, central North Island, New Zealand. *New Zealand Journal of Geology and Geophysics*, 19(2), 189–212.
- Brown, R.J., & Andrews, G.D. (2015). Deposits of pyroclastic density currents. In *The Encyclopedia of Volcanoes* (pp. 631-648). New York, NY: Academic Press.
- Brown, S.J.A., Burt, R.M., Cole, J.W., Krippner, S.J.P., Price, R.C., & Cartwright, I. (1998). Plutonic lithics in ignimbrites of Taupo Volcanic Zone, New Zealand: Sources and conditions of crystallisation. *Chemical Geology*, 148, 21–41.
- Burgisser, A., & Bergantz, G.W. (2002). Reconciling pyroclastic flow and surge: The multiphase physics of pyroclastic density currents. *Earth and Planetary Science Letters*, 202(2), 405–418.
- Bursik, M. I., Carey, S. N., & Sparks, R. S. J. (1992). A gravity current model for the May 18, 1980 Mount St. Helens plume. *Geophysical research letters*, 19(16), 1663-1666.
- Bursik, M. I., Sparks, R. S. J., Gilbert, J. S., & Carey, S. N. (1992). Sedimentation of tephra by volcanic plumes: I. Theory and its comparison with a study of the Fogo A plinian deposit, Sao Miguel (Azores). *Bulletin of Volcanology*, 54(4), 329-344.
- Carey, S.N., & Sparks, R.S.J. (1986). Quantitative models of the fallout and dispersal of tephra from volcanic eruption columns. *Bulletin of Volcanology*, 48,109–125.
- Carey, S., & Sigurdsson, H. (1989). The intensity of plinian eruptions. *Bulletin of Volcanology*, 51(1), 28–40.
- Cashman, K.V. (2004). Volatile controls on magma ascent and eruption. In R.S.J. Sparks & C.J. Hawkesworth (Eds.), *The State of the Planet: Frontiers and Challenges in Geophysics*. Washington, DC: American Geophysical Union.

- Cashman, K.V., & Scheu, B. (2015). Magmatic fragmentation. *Encyclopedia of Volcanoes* (pp. 459–471). New York, NY: Academic Press.
- Cashman, K., & Rust, A. (2016). Introduction: Part 2: Volcanic Ash: Generation and Spatial Variations. In *Volcanic ash: Hazard observation* (pp. 5-22). Elsevier Inc..
- Cashman, K., & Rust, A. (2016). Introduction: Part 3: Observations of Ash on the Ground. In *Volcanic Ash: Hazard Observation* (pp. 23-24). Elsevier Inc..
- Cashman, K., Sturtevant, B., Papale, P., & Navon, O. (2000). Magmatic Fragmentation. In H. Sigurdsson, B.F. Houghton & S. McNutt (Eds.), *Encyclopedia of Volcanoes* (1st ed., pp. 421–430). New York, NY: Academic Press.
- Cioni, R., Gurioli, L., Sbrana, A., & Vougioukalakis, S. (2000). Precursory phenomena and destructive events related to the Late Bronze Age Minoan (Thera, Greece) and AD 79 (Vesuvius, Italy) Plinian eruptions: Inferences from the stratigraphy in the archaeological areas. *Geological Society London: Special Publications*, 171(1), 124–141.
- Cole, J. W. (1990). Structural control and origin of volcanism in the Taupo volcanic zone, New Zealand. *Bulletin of volcanology*, 52(6), 445-459.
- Cole, J.W., Brown, S.J.A., Burt, R.M., Beresford, S.W., & Wilson, C.J.N. (1998). Lithic types in ignimbrites as a guide to the evolution of a caldera complex, Taupo volcanic centre, New Zealand. *Journal of Volcanology and Geothermal Research*, 80(3-4), 217-237.
- Dellino, P., Mele, D., Bonasia, R., Braia, G., La Volpe, L., & Sulpizio, R. (2005). The analysis of the influence of pumice shape on its terminal velocity. *Geophysical Research Letters*, 32(21), 1-4.
- Downs, D.T., Wilson, C.J.N., Cole, J.W., Rowland, J.V., Calvert, A.T., & Leonard, G.S. (2014). Age and eruptive center of the Paeroa Subgroup ignimbrites (Whakamaru Group) within the Taupo Volcanic Zone of New Zealand. *Geological Society of America Bulletin*, 126, 1131-1144
- Druitt, T.H. (1998). Pyroclastic density currents. *Geological Society, London, Special Publications*, 145(1), 145–182.
- Druitt, T.H., & Bacon, C.R. (1988). Compositional zonation and cumulus processes in the Mount Mazama magma chamber, Crater Lake, Oregon. *Earth and Environmental Science Transactions of The Royal Society of Edinburgh*, 79(2–3), 289–297.
- Druitt, T. H., Avard, G., Bruni, G., Lettieri, P., & Maez, F. (2007). Gas retention in fine-grained pyroclastic flow materials at high temperatures. *Bulletin of Volcanology*, 69(8), 881–901.
- Eichelberger, J.C. (1980). Vesiculation of mafic magma during replenishment of silicic magma reservoirs. *Nature*, 288(5790), 446–450.

- Eichelberger, J.C., & Koch, F.G. (1979). Lithic fragments in the Bandelier Tuff, Jemez Mountains, New Mexico. *Journal of Volcanology and Geothermal Research*, 5(1–2), 115–134.
- Ewart, A. (1963). Petrology and petrogenesis of the Quaternary pumice ash in the Taupo area, New Zealand. *Journal of petrology*, 4(3), 392–431.
- Fero, J., Carey, S.N., & Merrill, J.T. (2009). Simulating the dispersal of tephra from the 1991 Pinatubo eruption: Implications for the formation of widespread ash layers. *Journal of Volcanology and Geothermal Research*, 186(1-2), 120–131.
- Fierstein, J., & Wilson, C.J. (2005). Assembling an ignimbrite: Compositionally defined eruptive packages in the 1912 Valley of Ten Thousand Smokes ignimbrite, Alaska. *Geological Society of America Bulletin*, 117(7–8), 1094–1107.
- Folk, R.L., & Ward, W.C. (1957). Brazos River bar (Texas): A study in the significance of grain size parameters. *Journal of Sedimentary Research*, 27(1), 3–26.
- Froggatt, P. C. (1981). Stratigraphy and nature of Taupo Pumice formation. *New Zealand journal of geology and geophysics*, 24(2), 231–248.
- Froggatt, P. C., Wilson, C. J. N., & Walker, G. P. L. (1981). Orientation of logs in the Taupo Ignimbrite as an indicator of flow direction and vent position. *Geology*, 9(3), 109–111.
- Gardner, C.A., Cashman, K.V., Neal, C.A. (1998). Tephra-fall deposits from the 1992 eruption of Crater Peak, Alaska: Implications of clast textures for eruptive processes. *Bulletin of Volcanology*, 59, 537–555.
- Gladstone, C., & Sparks, R.S.J. (2002). The significance of grain-size breaks in turbidites and pyroclastic density current deposits. *Journal of Sedimentary Research*, 72(1), 182–191.
- Gould, R. (2012). Effusive and Explosive Eruptions. Retrieved from <https://www.geolsoc.org.uk/ks3/gsl/education/resources/rockcycle/page3599.html>
- Healy, J. (1964). Volcanic mechanisms in the Taupo Volcanic Zone, New Zealand. *New Zealand Journal of Geophysics*, 7(1), 6–23.
- Hess, K-U., & Dingwelt, D.B. (1996). Viscosity of hydrous leucogranitic melts: A non-Arrhenian model. *American Mineralogist*, 81, 1297–1300.
- Hildreth, W. (1983). The compositionally zoned eruption of 1912 in the valley of ten thousand smokes, Katmai National Park, Alaska. *Journal of Volcanology and Geothermal Research*, 18(1–4), 1–56
- Houghton, B.F., & Wilson, C.J.N. (1989). A vesicularity index for pyroclastic deposits. *Bulletin of Volcanology*, 51(6), 451–462.
- Houghton, B., & Carey, R.J. (2015). Pyroclastic fall deposits. *The Encyclopedia of Volcanoes* (pp. 599–616). New York, NY: Academic Press.

- Houghton, B.F., Hobden, B.J., Cashman, K.V., Wilson, C.J.N., & Smith, R.T. (2003). Large-scale interaction of lake water and rhyolitic magma during the 1.8 ka Taupo eruption, New Zealand. *Geophysical Monograph Series*, 140, 97–109.
- Houghton, B.F., Wilson, C.J.N., Fierstein, J., & Hildreth, W. (2004). Complex proximal deposition during the Plinian eruptions of 1912 at Novarupta, Alaska. *Bulletin of Volcanology*, 66, 95–133.
- Houghton, B.F., Carey, R.J., Cashman, K.V., Wilson, C.J., Hobden, B.J., & Hammer, J.E. (2010). Diverse patterns of ascent, degassing, and eruption of rhyolite magma during the 1.8 ka Taupo eruption, New Zealand: Evidence from clast vesicularity. *Journal of Volcanology and Geothermal Research*, 195(1), 31–47.
- Houghton, B. F., Carey, R. J., & Rosenberg, M. D. (2014). The 1800a Taupo eruption: “III wind” blows the ultraplinian type event down to Plinian. *Geology*, 42(5), 459–461.
- Kaminski, E., & Jaupart, C. (1997). Expansion and quenching of vesicular magma fragments in Plinian eruptions. *Journal of Geophysical Research*, 102, 12187–12204.
- Klug, C., & Cashman, K.V. (1994). Vesiculation of May 18, 1980, Mount St. Helens magma. *Geology*, 22(5), 468–472.
- Klug, C., Cashman, K.V. (1996). Permeability development in vesiculating magmas: Implications for fragmentation. *Bulletin of Volcanology*, 58, 87–100.
- Krumbein, W.C. (1934). Size frequency distributions of sediments. *Journal of Sedimentary Petrology*, 4, 65–77.
- Krumbein, W.C. (1938). Size frequency distributions of sediments and the normal phi curve. *Journal of Sedimentary Petrology*, 8, 84–90.
- Lejeune, A.M., & Richet, P. (1995). Rheology of crystal-bearing silicate melts: An experimental study at high viscosities. *Journal of Geophysical Research*, 100, 4215–4229.
- Lorenz, V. (1970). Some aspects of the eruption mechanism of the Big Hole maar, central Oregon. *Geological Society of America Bulletin*, 81(6), 1823–1830.
- Lorenz, V. (1974). Vesiculated tuffs and associated features. *Sedimentology*, 21(2), 273–291.
- Lube, G., Cronin, S.J., & Thouret, J.C. (2011). Kinematic characteristics of pyroclastic density currents at Merapi and controls on their avulsion from natural and engineered channels. *Geological Society of America Bulletin*, 123(5–6), 1127–1140.
- Lube, G., Breard, E.C.P., Cronin, S.J., & Jones, J. (2015). Synthesizing large-scale pyroclastic flows: Experimental design, scaling, and first results from PELE. *Journal of Geophysical Research: Solid Earth*, 120(3), 1487–1502.
- Lube, G., Breard, E. C., Esposti-Ongaro, T., Dufek, J., & Brand, B. (2020). Multiphase flow behaviour and hazard prediction of pyroclastic density currents. *Nature Reviews Earth & Environment*, 1–18.

- Manville, V., & Wilson, C. J. (2004). The 26.5 ka Oruanui eruption, New Zealand: A review of the roles of volcanism and climate in the post-eruptive sedimentary response. *New Zealand Journal of Geology and Geophysics*, 47(3), 525-547.
- Manville, V., & Wilson, C. J. N. (2004). Vertical density currents: a review of their potential role in the deposition and interpretation of deep-sea ash layers. *Journal of the Geological Society*, 161(6), 947-958.
- Manville, V., Segschneider, B., Newton, E., White, J.D.L., Houghton, B.F., & Wilson, C.J.N. (2009). Environmental impact of the 1.8 ka Taupo eruption, New Zealand: Landscape responses to a large-scale explosive rhyolite eruption. *Sedimentary Geology*, 220(3-4), 318-336.
- Milicich, S.D., Chambefort, I., Wilson, C.J.N., Alcaraz, S., Ireland, T.R., Bardsley, C., & Simpson, M.P. (2020). A zircon U-Pb geochronology for the Rotokawa geothermal system, New Zealand, with implications for Taupō Volcanic Zone evolution. *Journal of Volcanology and Geothermal Research*, 389, 1-19.
- Mitchell, S.J., Biass, S., Houghton, B.F., Anderson, A., Bonny, E., Walker, B.H., ... & Rosenberg, M.D. (2018). The interplay among clast size, vesicularity, post-fragmentation expansion, and clast breakage: An example from the 1.8 ka Taupo eruption. *Geological Society of America Special Paper*, 538, 375-383.
- Morrissey, M., Zimanowski, B., Wohletz, K., & Buettner, R. (2000). Vulcanian eruptions. In H. Sigurdsson, B.F. Houghton, S.R. McNutt, H. Rymer & J. Stix (Eds.), *Encyclopedia of Volcanoes* (pp. 463-476). New York, NY: Academic Press.
- Mourtada-Bonnefoi, C.C., & Laporte, D. (1999). Experimental study of homogenous bubble nucleation in rhyolitic magmas. *Geophysical Research Letters*, 26, 3505-3508.
- Newman, S., Epstein, S., & Stolper, E. (1988). Water, carbon dioxide and hydrogen isotopes in glasses from the ca. 1340 A.D. eruption of the Mono Craters, California: Constraints on degassing phenomena and initial volatile content. *Journal of Volcanology and Geothermal Research*, 35, 75-96.
- Nisbet, E. (2019). *Stratigraphy, grain-size characteristics and componentry of Y1: The initial phase of the AD232 Taupo eruption, New Zealand* (Honour's thesis, Massey University).
- Pallister, J.S., Hoblitt, R.E., & Reyes, A.G. (1992). A basalt trigger for the 1991 eruptions of Pinatubo Volcano? *Nature*, 356, 426-428.
- Polacci, M., Papale, P., & Rosi, M. (2001). Textural heterogeneities in pumices from the climactic eruption of Mount Pinatubo, 15 June 1991, and implication for magma ascent dynamics. *Bulletin of Volcanology*, 63, 83-97.
- Pyle, D.M. (1989). The thickness, volume and grainsize of tephra fall deposits. *Bulletin of Volcanology*, 51(1), 1-15.
- Pyle, D. M. (2015). Sizes of volcanic eruptions. *The Encyclopedia of Volcanoes* (pp. 257-264). New York, NY: Academic Press.
- Rotella, M.D., Wilson, C.J., Barker, S.J., Cashman, K.V., Houghton, B.F., & Wright, I.C. (2014). Bubble development in explosive silicic eruptions: Insights from pyroclast vesicularity textures from Raoul volcano (Kermadec arc). *Bulletin of Volcanology*, 76(8), 1-24.



- Rust, A.C., Cashman, K.V., & Wallace, P.J. (2004). Magma degassing buffered by vapor flow through brecciated conduit margins. *Geology*, 32(4), 349–352.
- Shea, T., Houghton, B. F., Gurioli, L., Cashman, K. V., Hammer, J. E., & Hobden, B. J. (2010). Textural studies of vesicles in volcanic rocks: an integrated methodology. *Journal of Volcanology and Geothermal Research*, 190(3-4), 271-289.
- Shea, T., Gurioli, L., & Houghton, B.F. (2012). Transitions between fall phases and pyroclastic density currents during the AD 79 eruption at Vesuvius: Building a transient conduit model from the textural and volatile record. *Bulletin of Volcanology*, 74(10), 2363–2381.
- Sigurdsson, H., Houghton, B., McNutt, S., Rymer, H., & Stix, J. (2015). *The Encyclopedia of volcanoes*. New York, NY: Academic Press.
- Smith, R. C. M. (1988). Landscape response to a major ignimbrite eruption: post-Taupo eruption sedimentation and landform evolution in the SE Taupo area (Doctoral dissertation, University of Auckland).
- Smith, R. T., & Houghton, B. F. (1995). Delayed deposition of plinian pumice during phreatoplinian volcanism: the 1800-yr-BP Taupo eruption, New Zealand. *Journal of volcanology and geothermal research*, 67(4), 221-226.
- Sparks, R.S.J. (1976). Grain size variations in ignimbrite and implications for the transport of pyroclastic flows. *Sedimentology*, 23, 147–188.
- Sparks, R.S.J. (1978). The dynamics of bubble formation and growth in magmas: A review and analysis. *Journal of Volcanology and Geothermal Research*, 3, 1-37.
- Sparks, R. S. J., Bursik, M. I., Ablay, G. J., Thomas, R. M. E., & Carey, S. N. (1992). Sedimentation of tephra by volcanic plumes. Part 2: controls on thickness and grain-size variations of tephra fall deposits. *Bulletin of Volcanology*, 54(8), 685-695.
- Sutton, A. N., Blake, S., Wilson, C. J., & Charlier, B. L. (2000). Late Quaternary evolution of a hyperactive rhyolite magmatic system: Taupo volcanic centre, New Zealand. *Journal of the Geological Society*, 157(3), 537-552.
- Suzuki, T. (1983). A theoretical model for dispersion of tephra. In D. Shimozuru & I. Yokoyama (Eds.), *Arc Volcanism: Physics and Tectonics* (pp. 95–113). Tokyo, Japan: Terra Scientific.
- Suzuki, Y.J., Costa, A., Cerminara, M., Esposti Ongaro, T., Herzog, M., Van Eaton, A.R., & Denby, L.C. (2016). Inter-comparison of three dimensional models of volcanic plumes. *Journal of Volcanology and Geothermal Research*, 326, 26–42.
- Talbot, J. P. (1989). Grain morphology and origins of fine ash deposits from the 180 AD Taupo eruption, central North Island, New Zealand.
- Talbot, J. P., Self, S., & Wilson, C. J. N. (1994). Dilute gravity current and rain-flushed ash deposits in the 1.8 ka Hatepe Plinian deposit, Taupo, New Zealand. *Bulletin of Volcanology*, 56(6-7), 538-551.

- Thorarinsson, S. (1950). The eruption of Mt. Hekla 1947–1948. *Bulletin volcanologique*, 10(1), 157-168.
- Thorarinsson, S. (1954). The eruption of Hekla, 1947-1948, Part II 3. The tephra-fall from Hekla on March 29 th, 1947. *Visindafelag Islendinga*, 68.
- Thorarinsson, S., & Einarsson, T. (1950), The eruption of Mt. Hekla: 1947-1948, II 2. A study of the earlier photographs of the eruption. *Rlsindafelag Islensinga*, 15.
- Thordarson, T. (1990). *The eruption sequence and eruption behaviour of the Laki 1783-1785 eruption, Iceland: Characteristics and distribution of eruption products* (Master of Science thesis, University of Texas).
- Valentine, G.A. (1987). Stratified flow in pyroclastic surges. *Bulletin of Volcanology*, 49(4), 616–630.
- Von Lichtan, I.J., White, J.D.L., Manville, V., & Ohneiser, C. (2016). Giant rafted pumice blocks from the most recent eruption of Taupo volcano, New Zealand: Insights from palaeomagnetic and textural data. *Journal of Volcanology and Geothermal Research*, 318, 73-88.
- Walker, G.P.L. (1971). Grain-size characteristics of pyroclastic deposits. *The Journal of Geology*, 79(6), 696–714.
- Walker, G.P.L. (1980). The Taupo pumice: Products of the most powerful known (ultraplinian) eruption? *Journal of Volcanology and Geothermal Research*, 8(1), 69–94.
- Walker, G.P.L. (1981a). The Waimihia and Hatepe plinian deposits from the rhyolitic Taupo volcanic center. *New Zealand Journal of Geology and Geophysics*, 24(3), 305–324.
- Walker, G.P.L. (1981b). Plinian eruptions and their products. *Bulletin of Volcanology*, 44(2), 223–240.
- Walker, G.P.L (1981c). Characteristics of two phreatoplinian ashes, and their water-flushed origin. *Journal of Volcanology and Geothermal Research*, 9(4), 395-407.
- Walker, G.P.L (1981d). Generation and dispersal of fine ash and dust by volcanic eruptions. *Journal of Volcanology and Geothermal Research*, 11(1), 81-92.
- Walker, G. P. (1983). Ignimbrite types and ignimbrite problems. *Journal of volcanology and geothermal research*, 17(1-4), 65-88.
- Walker, G. P. (1984). Downsag calderas, ring faults, caldera sizes, and incremental caldera growth. *Journal of Geophysical Research: Solid Earth*, 89(B10), 8407-8416.
- Walker, G.P.L., Heming, R.F., & Wilson, C.J.N. (1980). Low-aspect ratio ignimbrites. *Nature*, 283(5744), 286-287.
- Walker, G. P. L., Self, S., & Froggatt, P. C. (1981). The ground layer of the Taupo ignimbrite: a striking example of sedimentation from a pyroclastic flow. *Journal of Volcanology and Geothermal Research*, 10(1-3), 1-11.
- Walker, G. P. L., Wilson, C. J. N., & Froggatt, P. C. (1981). An ignimbrite veneer deposit: the trail-marker of a pyroclastic flow. *Journal of Volcanology and Geothermal Research*, 9(4), 409-421.

- Walshe, J.L. (1986). A six-component chlorite solid solution model and the conditions of chlorite formation in hydrothermal and geothermal systems. *Economic Geology*, 81(3), 681-703.
- Wilson, L. (1976). Explosive volcanic eruptions—III. Plinian eruption columns. *Geophysical Journal International*, 45(3), 543-556.
- Wilson, C. J. N. (1980). The role of fluidization in the emplacement of pyroclastic clasts: An experimental approach. *Journal of Volcanology and Geothermal Research*, 8(2-4), 231-249.
- Wilson, C. J. N. (1985). The Taupo eruption, New Zealand. II. The Taupo ignimbrite. *Philosophical Transactions of the Royal Society of London. Series A, Mathematical and Physical Sciences*, 314(1529), 229-310.
- Wilson, C. J. N. (1985). The Taupo eruption, New Zealand. II. The Taupo ignimbrite. *Philosophical Transactions of the Royal Society of London. Series A, Mathematical and Physical Sciences*, 314(1529), 229-310.
- Wilson, C.J.N. (1993). Stratigraphy, chronology, styles and dynamics of late Quaternary eruptions from Taupo volcano, New Zealand. *Philosophical Transactions of the Royal Society of London*, 343, 205–306.
- Wilson, C. J. (2001). The 26.5 ka Oruanui eruption, New Zealand: an introduction and overview. *Journal of Volcanology and Geothermal Research*, 112(1-4), 133-174.
- Wilson, C.J.N., & Walker, G.P.L. (1985). The Taupo Eruption, New Zealand. *Philosophical Transactions of the Royal Society of London*, 314, 199–228.
- Wilson, L., & Walker, G. P. L. (1987). Explosive volcanic eruptions-VI. Ejecta dispersal in plinian eruptions: the control of eruption conditions and atmospheric properties. *Geophysical Journal International*, 89(2), 657-679.
- Wilson, C.J.N., & Hildreth, E.W. (1997). The Bishop Tuff: New insights from eruptive stratigraphy. *Journal of Geology*, 105, 407–440.
- Wilson, L., Sparks, R.S.J., Huang, T.C., & Watkins, N.D. (1978). The control of volcanic eruption column heights by eruption energetics and dynamics. *Journal of Geophysical Research*, 83(B4), 1829–1836.
- Wilson, C. J. N., Ambraseys, N. N., Bradley, J., & Walker, G. P. L. (1980). A new date for the Taupo eruption, New Zealand. *Nature*, 288(5788), 252-253.
- Wilson, C. J. N., Houghton, B. F., Kampt, P. J. J., & McWilliamst, M. O. (1995). An exceptionally widespread ignimbrite with implications for pyroclastic flow emplacement. *Nature*, 378(6557), 605-607.
- Wilson, C. J. N., Houghton, B. F., McWilliams, M. O., Lanphere, M. A., Weaver, S. D., & Briggs, R. M. (1995). Volcanic and structural evolution of Taupo Volcanic Zone, New Zealand: a review. *Journal of volcanology and geothermal research*, 68(1-3), 1-28.
- Wilson, C. J. N., Houghton, B. F., Pillans, B. J., & Weaver, S. D. (1995). Taupo Volcanic Zone calc-alkaline tephra on the peralkaline Mayor Island volcano, New Zealand: identification and uses as marker horizons. *Journal of volcanology and geothermal research*, 69(3-4), 303-311.

Wilson, C. J. N., Gravley, D. M., Leonard, G. S., & Rowland, J. V. (2009). Volcanism in the central Taupo Volcanic Zone, New Zealand: tempo, styles and controls. *Studies in volcanology: the legacy of George Walker*. Special Publications of IAVCEI, 2, 225-247.

# Appendix 1

Abbreviations used in the following tables:

*a* - angular

*aP* - angular pumice

*BBS* - Boundary Based Sample

*BR* - banded rhyolite

*C* - crystal

*cA* - coarse ash,

*CBS* - Continuous Based Sample

*cL* - coarse lapilli

*cm* - centimetres

*fA* - fine ash

*fL* - fine lapilli

*fLP* - fine lapilli pumice

*GJ* - Grey Juveniles

*LB* - Lower Boundary

*LC* - lithic

*mA* - medium ash

*ML* - max lithic

*mL* - medium lapilli

*mm* - millimetres

*MP* - max pumice

*O* - obsidian

*P* - pumice

*R* - rounded

*Sa* - sub-angular

*SaP* - sub-angular pumice

*SR* - sub-rounded

*SRP* - sub-rounded pumice

*UB* - Upper Boundary


*vcL* - very coarse lapilli

*vfA* - very fine ash

*vfL* - very fine lapilli


Black lines on the outcrop photo outline the layer boundaries and maroon shows the internal layers that weren't extracted. Measurements and clast sizes are presented in millimetres.

Location 1	Sample Name	Thickness Info	Max Clast Size	Boundaries	Macroscopic Description	Field Interpretation	Additional Information
	1 BBS	6 cm	MP=~50 mm	UB= Sharp LB= Gradual	Moderately sorted, cL/vcL, massive, white pumice dominated, P: very vesicular>GJ(~5-10%)>BR(~1cm)>O(<0.5cm)>LC.	Fall	Clast supported
	2A CBS	24.8 cm	MP=~100 mm	UB= Gradual LB= Gradual	Poorly sorted, vcL, massive, white pumice with some pink in the middle, very vesicular, rounded vesicles Sa-a>BR(~20%)>O(~30%)>C>LC	Fall	Minor Iron Staining
	2B CBS	24.8 cm	MP=~10cm	UB= Gradual LB= Gradual	Poorly sorted, vcL, massive, white pumice with some pink in the middle, very vesicular, rounded vesicles Sa-a>BR(~20%)>O(~30%)>C>LC	Fall	
	2C CBS	24.8 cm	MP=120x190 mm	UB= Gradual LB= Gradual	Poorly sorted, vcL, massive, white pumice with some pink in the middle, very vesicular, rounded vesicles Sa-a>BR(~20%)>O(~30%)>C>LC	Fall	
	2D CBS	24.8 cm	MP=120x190 mm	UB= Gradual LB= Gradual	Poorly sorted, vcL, massive, white pumice with some pink in the middle, very vesicular, rounded vesicles Sa-a>BR(~20%)>O(~30%)>C>LC	Fall	
	2E CBS	24.8 cm	MP=~130 mm	UB= Gradual LB= Gradual	Poorly sorted, vcL, massive, white pumice with some pink in the middle, very vesicular, rounded vesicles Sa-a>BR(~20%)>O(~30%)>C>LC	Fall	
	2F BBS	5 cm	ML=~ 40-50 mm MP=~31.5 mm	UB= Gradual LB= Sharp	Moderately sorted, cL, massive, white pumice with some pink in the middle, very vesicular, rounded vesicles Sa-a> LC(~30%)>BR(~20%)>O(~30%)>C	Fall	
	3 BBS	4.5 cm	MP=~15 mm	UB= Sharp LB= Sharp	Poorly sorted, fA with larger pumices. P(0.2-1.5cm)>BR>GJ(~10%)	Rain Flush?	
	4 BBS	10 cm	MP=~40 mm	UB= Sharp LB= Sharp	Poor-Moderately sorted, cL, pumice dominated, P: weakly vesiculated>BR>LC(~1-5%.red, green, grey, hydrothermally altered)>C	Fall	
	5 BBS	5 cm	MP=~15 mm	UB= Sharp LB= Sharp	Poorly sorted, fA with larger pumices. P(0.2-1.5cm)>BR>GJ(~10%)	Rain Flush?	
	6 BBS	5.5 cm	MP= ~30 mm	UB= Sharp LB= Sharp	Poor-Moderately sorted, cL, pumice dominated, P: weakly vesiculated>BR>LC(~1-5%.red, green, grey, hydrothermally altered)>C	Fall	
	7 BBS	8 cm	MP= ~15 mm	UB= Sharp LB= Sharp	Poorly sorted, fA with larger pumices. P(0.2-1.5cm)>BR>GJ(~10%)	Rain Flush?	
	8 BBS	3.5 cm	MP= ~30 mm	UB= Sharp LB= Sharp	Poorly sorted, cL, massive, white pumice dominated. P>LC(green, grey)	Fall	
	9 BBS	5 cm	MP=~15 mm	UB= Sharp LB= Sharp	Poorly sorted, fA with larger pumices. P(0.2-1.5cm)>BR>GJ(~10%)	Rain Flush	
10 BBS	26.5 cm	MP~60 mm	UB= Sharp LB= Sharp	Poor-moderately sorted, vcL, massive, white pumice dominated. P: vesicular, round vesicles > BR (~8%)>LC(~4%)	Fall	Minor Iron Staining	
11 BBS	3 cm	MP=~15 mm	UB= Sharp LB= Sharp	Poorly sorted, fA with larger pumices. P(0.2-1.5cm)>BR>GJ(~10%)	Rain Flush?		
12 BBS	9 cm	MP=~40 mm	UB= Sharp LB= Sharp	Poor-moderately sorted, vcL, massive, white pumice dominated. P: vesicular, round vesicles >LC(~25%, ~2cm) > BR (~8%, ~4cm)	Fall		
13 BBS	4 cm	MP=~15mm	UB= Sharp LB= Sharp	Poorly sorted, fA with larger pumices. P(0.2-1.5cm)>BR>GJ(~10%)	Rain Flush?		
14 BBS	3.5 cm	MP=~40 mm	UB= Sharp LB= Sharp	Poor-moderately sorted, vcL, massive, white pumice dominated. P: vesicular, round vesicles >LC(~25-35%, ~1cm) > BR (~8%, ~4cm)	Fall		

Location 2	Sample Name	Thickness Info	Max Clast size	Boundaries	Macroscopic Description	Field Interpretation	Additional Information
	1 (BBS)	20 cm	MP=31.5 mm	UB=Sharp with Y3 LB=sharp	Poorly sorted, cL-vcL, white pumice dominated>BR>LC (red and iron stained)>O	Fall	Clast cupped, supporting clasts (1-5mm)
	2A (BBS)	22 cm	MP=31.5mm	UB=Gradual LB=Gradual	Moderate to poorly sorted, cL, white pumice dominated:aP-SRP>LC>BR	Fall	Weak banding is seen coarser finer (Figure 6.1.3 (A))
	2B (BBS)	22 cm	MP=22.4 mm	UB=Gradual LB=Gradual	Moderate to poorly sorted, cL, white pumice dominated:aP-SRP>LC>BR	Fall	Slightly iron stained
	2C (BBS)	22 cm	MP=22.4 mm	UB=Gradual LB=Gradual	Moderate to poorly sorted, cL, white pumice dominated:aP-SRP>LC>BR	Fall	
	3 (BBS)	8 cm	MP=22.4 mm	UB=sharp undulating LB=sharp undulating	Moderately to poorly sorted, fL, white-slightly yellow pumice>LC (~20%)>BR&O	Fall	
	4 (BBS)	6 cm	MP=11.2 mm	UB=sharp undulating LB=sharp undulating	Moderately sorted, mL-cL, dominated by white pumice: SaP>LC>BR.	Fall	
	5 (BBS)	3.5 cm	MP=11.2 mm	UB=sharp undulating LB=sharp	Moderately sorted, fL, dominated by white pumice: SaP>LC>BR.	Fall	Slight iron staining
	6 (BBS)	32 cm	MP=16 mm	UB=sharp LB=gradual undulating	Moderately to poorly sorted, mL, pumice dominated>LC>BR&O	Fall	
	7 (BBS)	11 cm	MP=22.4 mm	UB=sharp gradual LB= gradual undulating	Moderately to poorly sorted,vcL- cL, pumice dominated>LC>BR&O	Fall	Slight iron staining
8 (BBS)	3 cm	MP=16 mm	UB=sharp undulating LB=undulating	Moderately sorted, cL-mL, white P>LC(red, black and old lavas ~15-20%)>BR	Fall		





Location 3	Sample Name	Thickness Info	Max Clast Size	Boundaries	Macroscopic Description	Field Interpretation
	16 (30-31cm) CBS	1 cm	MP=4mm	UB/LB=Gradual	Well sorted; vFL,>, P white –creamy yellow> LC (~3%)>O	Fall
	15 (30-28cm) CBS	2 cm	MP=5.6mm	UB/LB=Gradual	Moderately sorted, fL dominantly pumice(Very Vesicular/SRP: white – creamy yellow)> C> O.	Fall
	14 (28-26cm) CBS	2 cm	MP=5.6mm	UB/LB=Gradual	Moderately sorted, mL, P: white – creamy yellow, AP,>C> O> LC (~1%)	Fall
	13 (26-24cm) CBS	2 cm	MP=4mm	UB/LB=Gradual	Moderately sorted, mL, P: white – creamy yellow aP>C> O>LC (~1%)	Fall
	12 (24-22cm) CBS	2 cm	MP=5.6mm	UB/LB=Gradual	Moderately Sorted, mL, P: white – creamy yellow AP>C> O> LC (~1%)	Fall
	11 (22-20cm) CBS	2 cm	MP=5.6mm	UB/LB=Gradual	Moderately sorted, mL, P: white – creamy yellow AP>C> O> LC (~1%)	Fall
	10 (20-18cm) CBS	2 cm	MP=5.6mm	UB/LB=Gradual	Moderately Sorted. mL, P: white – creamy yellow AP>C> O> LC (~1%)	Fall
	9 (18-16cm) CBS	2 cm	MP=11.2mm ML=~0.5-1cm	UB/LB=Gradual	Moderately sorted, mL, P: white – creamy yellow, SaP with vesicles ranging from round –stretched> LC>O	Fall
	8 (16-14cm) CBS	2 cm	MP=5.6mm	UB/LB=Gradual	Moderately to well sorted, fL, white – creamy yellow vesiculated Pumice> LC (~5-8%)> O(~3-6%)	Fall
	7 (14-12cm) CBS	2 cm	MP=8mm	UB/LB=Gradual	Moderately sorted pumice dominated mL, P: white – creamy yellow, SRP/SaP with rounded vesicles> C(MC=0.5cm)>LC (~4-7%)> BR, O, & GJ	Fall
	6 (12-10cm) CBS	2 cm	MP=8mm	UB/LB=Gradual	Moderately sorted, fL, white – creamy yellow P>LC (~10%)>C&O.	Fall
	5 (10-8cm) CBS	2 cm	MP=5.6mm	UB/LB=Gradual	Moderately sorted, fL, white – creamy yellow P> LC (~10%)> O(~4%)>C	Fall
	4 (8-6cm) CBS	2 cm	MP=5.6mm	UB/LB=Gradual	Moderately sorted, fL, white – creamy yellow P> LC (~10%)> O(~4%)>C	Fall
	3 (6-4cm) CBS	2 cm	MP=5.6mm	UB/LB=Gradual	Moderately sorted, fL, white – creamy yellow P> LC (~5%)>C> O(~4%)	Fall
2 (4-2cm) CBS	2 cm	MP=4mm	UB/LB=Gradual	Moderately sorted, fL, white – creamy yellow P> LC (~5%)> O(~1%)>C	Fall	
1 (2-0cm) CBS	2 cm	MP=4mm	UB=Gradual LB=Undulating	Moderately sorted, fL, white – creamy yellow P> LC (~5%)> C>O(~1%)	Fall	

Location 4	Subunit name	Thickness Info	Range	Boundaries	Macroscopic descriptions	Additional Information	Field Interpretation
	1 (BBS)	0.5 cm	MP=~2 mm	UB=Sharp LB=Gradual	Well Sorted; fL/mL dominantly Pumice: creamy white-Yellow: with fA, P>GJ>O>L.C	Ash from Y3 incorporated	Fall
	1.5 (BBS)	1.5 cm	MP=~2 mm	UB/LB=Gradual	Moderately Sorted; Pumice: white – yellow: fLP> LC (~10-15%), >C (~4%), O.& GJ (~3%)		Fall
	2 (CBS)	2 cm	MP=~6 mm	UB/LB=Gradual	Moderately Sorted; Pumice: white – yellow: fLP> LC (~10-15%), >C (~4%), O.& GJ (~3%)		Fall
	3 (CBS)	2 cm	MP=~6 mm	UB/LB=Gradual	Moderately Sorted; Pumice: white – yellow: fLP> LC (~10-15%), >C (~4%), O.& GJ (~3%)		Fall
	4 (CBS)	2 cm	MP=~6 mm	UB/LB=Gradual	Moderately Sorted; Pumice: white – yellow: fLP> LC (~10-15%), >C (~4%), O.& GJ (~3%)		Fall
	5 (CBS)	2 cm	MP=~6 mm	UB/LB=Gradual	Moderately Sorted; Pumice: white – yellow: fLP> LC (~10-15%), >C (~4%), O.& GJ (~3%)		Fall
	6 (CBS)	2 cm	MP=~6 mm	UB/LB=Gradual	Moderately Sorted; Pumice: white – yellow: fLP> LC (~10-15%), >C (~4%), O.& GJ (~3%)		Fall
	7 (CBS)	2 cm	MP=~6 mm	UB/LB=Gradual	Moderate-Poorly sorted; fLP white – yellow: >LC (~5%)> C (~4%)> GJ (~3%)>O		Fall
	8 (CBS)	2 cm	MP=~6 mm	UB/LB=Gradual	Moderate-Poorly sorted; fLP white – yellow: >LC (~5%)> C (~4%)> GJ (~3%)>O		Fall
	9 (CBS)	2 cm	MP=~6 mm	UB/LB=Gradual	Moderate-Poorly sorted; fLP white – yellow: >LC (~5%)> C (~4%)> GJ (~3%)>O		Fall
	10 (CBS)	2 cm	MP=~6 mm	UB/LB=Gradual	Moderate-Poorly sorted; fLP white – yellow: >LC (~5%)> C (~4%)> GJ (~3%)>O		Fall
	11 (CBS)	2 cm	MP=~6 mm	UB/LB=Gradual	Moderate-Poorly sorted; fLP white – yellow: >LC (~5%)> C (~4%)> GJ (~3%)>O		Fall
12 (CBS)	2 cm	MP=~6 mm	UB=Gradual LB=Undulating	Moderate-Poorly sorted; fLP white – yellow: >LC (~5%)> C (~4%)> GJ (~3%)>O	LB with paleosol wet/muddy. Small amounts of this mud was incorporated in the lower sample. In this Location there is a small gully with Y4 and Y5 entering the Y2 unit (figure x)	Fall	

Location 5	Sample Name	Thickness Info	Max Clast Size	Boundaries	Macroscopic Description	Field Interpretation	Additional Information
	1 BBS	17 cm	MP=45mm ML=~2-4cm	UB=Sharp LB=Sharp	Moderately sorted, cL/vcL, P: white & grey, minimal staining, dense > LC (~20%;red/purple)>O(~2.5-0.1cm, ~5%)=C, minimal BR.	Fall	
	2A CBS	43.667 cm	MP=31.5mm	UB=Sharp LB=Gradual	Moderately to poorly sorted, cL, P: white-grey-pink, dense with some glassy, banded, Grey Pumice(~2-5%)>LC (20%, brownish purple,green, minor oxidation)>C(~5%)>O	Fall	Minor coarser finer alteration.
	2B CBS	43.667cm	MP=45mm	UB=Gradual LB=Gradual	Moderately to poorly sorted, cL, P: white-grey-pink, dense with some glassy, banded, Grey Pumice(~2-5%)>LC (10-14%, brownish purple,green, minor oxidation)>C(~5%)>O	Fall	
	2C CBS	43.667cm	MP=45mm	UB=Gradual LB=Gradual	Moderately to poorly sorted, cL, P: white-grey-pink, dense with some glassy, banded, Grey Pumice(~2-5%)>LC (8%, brownish purple,green, minor oxidation)>C(~5%)>O	Fall	
	3 BBS	25 cm	MP=31.5mm	UB=Gradual LB=Gradual	Moderately to poorly sorted, mL, P: white-grey-pink, dense, round vesicles>fibrous pumice(~15-20%)>LC (8%, brownish purple,green, minor oxidation)>C(~5%,max~4mm)>O	Fall	
	4 BBS	9 cm	MP=31.5mm ML=~2cm	UB=Gradual LB=Gradual	Moderately to well sorted, fL/mL, P:white-grey, dense with few fibrous> LC (~35%,red,green pumice,brown)>C(~5%)>O	Fall	
	5 BBS	5 cm	MP=22.4mm	UB=Gradual LB=Gradual	Moderately to well sorted, cL, P: white-grey, dense with few fibrous> LC (~35%,red,green pumice,brown)>C(~3-5%, max~0.2-0.5cm)>O	Fall	
	6 BBS	8.5 cm	MP=22.4mm	UB=Gradual LB=Gradual	Moderately to well sorted, fL/mL, P:white-grey, dense with few fibrous> LC (~40%,red,green pumice,brown)>C(~5%)>O	Fall	
	7 BBS	14.5 cm	MP=45mm	UB=Gradual LB=Gradual	Moderately sorted, cL, P: white-white with pink centre ~10%, with grey to dark grey banded pumice>LC (~20%,green)>O, minor crystals	Fall	
	8 BBS	1 cm	MP=16mm	UB=undulating gradual LB=undulating gradual	Poorly sorted, creamy white to light grey,vfA/fA with cL, P>LC, undulating layer.	Rain Flush	
9 BBS	18 cm	MP=45mm	UB=undulating gradual LB=Undulating	Poorly sorted, cL/vcL, P: white-grey-light yellowish brown,banded, coarser towards base> LC (~10% top, brown,reds,green, increase at base ~30%) >C(~3%)>GJ&O.	Fall	Normal graded Iron staining	
10 BBS	4.5 cm	MP=8mm	UB=Undulating LB=Undulating	fA with mL pumices mixed in. Creamy white to light grey.	Possibly Y1 with impact pumices	Impact pumices incorporated	

Location 6	Sample Name	Thickness Info	Max Clast Size	Boundaries	Macroscopic Description	Field Interpretation	Additional Information
	1 (BBS)	6 cm	MP=~16-22.4 mm	UB=Sharp undulating LB=Gradual	Moderate to poorly sorted, cL, P: white, vesicular>GJ,O,&LC(~5%), Lower 1cm fL, LC+O+GJ(40%)	Fall	
	2a (BBS)	9.5 cm	MP=~16mm	UB=Gradual LB=Gradual	Moderate to poorly sorted, cL, P: white vesicular>LC(green, pink, brown)>O(0.5cm)	Fall	1cm of finer lithic rich lapilli, that could not be separated from the sample is included (marked by red line)
	2b (BBS)	9.5 cm	MP=~16 mm	UB=Gradual LB=Gradual	Moderate to poorly sorted, cL, P: white vesicular to very vesicular, elongated-rounded>LC (green, pink, brown)>O(0.5cm)>BR(5%)	Rain flush	
	3 (BBS)	3.5 cm	MP=~8 mm	UB=Gradual LB=sharp	Moderately to poorly sorted, fL/mL, P: white vesicular to very vesicular >LC (green, pink, brown)>O(0.5cm, ~1%)>>GJ(~45%)>, LC (~1%) lack of crystals. Lower 2cm line lithic rich band of fL	Fall	
	4 (BBS)	4 cm	MP=~4 mm	UB=sharp LB=sharp	fA-mA, creamy light brown to white, P>O&GJ(~50% combined), no lapilli band.	Fall with a small rain flush bed. Dilute gravity Current?	Upper section has a small 0.8cm ashier band (marked by the red lines) that could not be separated out of the sample due to the coarseness of the pumice.
	5 (BBS)	2 cm	MP=~8 mm	UB=sharp LB=sharp	Moderately sorted, mL, pumice dominated, P>O+GJ(~5%)	Fall	
	6 (BBS)	5 cm	MP=~2 mm	UB=sharp LB=sharp	fA-mA, creamy light brown to white, P>O&GJ(~50% combined), no lapilli band.	Rain Flush? Dilute Gravity Current?	
	7 (BBS)	3 cm	MP=~2-4 mm	UB=sharp LB=sharp	Moderately sorted, mL, pumice dominated, P:white, very vesicular, fibrous>GJ+O(~35-40%)>LC (~5%)	Fall	
	8 (BBS)	7 cm	MP=~2 mm	UB=sharp LB=sharp	fA-mA, creamy light brown to white, with a fL 1cm band in the middle P>O&GJ(~50% combined),	Dilute Density Current	
9 (BBS)	6.5 cm	MP=~8-16 mm	UB=sharp LB=undulating	Moderate to poorly sorted, top and bottom of bed lined with fL, P:white-light brown stained, vesicular>GJ. Middle of bed pumice dominated>GJ(~5-10%)>O(~5-10%)>LC (~3%, brown, green & red)	Fall		

Location 7	Sample Name	Thickness Info	Max Clast Size	Boundaries	Macroscopic Description	Field Interpretation	Additional Information
	1 (BBS)	2 cm	MP=~1-2 mm	UB=Sharp LB=Gradual	Moderately to well sorted fL, pumice dominated. P: white-light grey>LC (~30%)>C(~3%)	Fall	Minimal weathering
	2 (BBS)	6 cm	MP=~1-4 mm	UB=Gradual LB=Gradual	Moderately to well sorted, fL/mL, pumice dominated. P: white-light grey>LC (~20-30%)>C(~3%)	Fall	
	3 (BBS)	4 cm	MP=~2-4 mm	UB=Gradual LB=Gradual	Moderately sorted, mL/cL, pumice dominated. P: white-light grey>LC (~5-10%)>C(~3%)	Fall	Iron staining
	4 (BBS)	14.5 cm	MP=~4 mm	UB=Gradual LB=Gradual	Moderately sorted, cL, Pumice dominated, P: white grey>LC (~15%)>C(~3%)	Fall	Small coarser finer banding seen
	5 (BBS)	4 cm	MP=~4 mm	UB=Gradual LB=Sharp undulating	Moderately sorted mL/cL, lithic dominated (40-60%)>P(white-light grey)	Fall	
	6 (BBS)	3 cm	MP=~3-5 mm	UB=Sharp undulating LB=Sharp	Grey-beige cA with cL, P: white to beige	Fall	

Location 8	Sample Name	Thickness Info	Max Clast Size	Boundaries	Macroscopic Description	Field Interpretation	Additional Information
	1 (BBS)	1.5 cm	MP=11.2 mm	UB=Mix boundary LB= sharp	Poorly sorted, cL with fA, Pumice dominated. P>LC.	Fall	Uppermost Lapilli layer with Y3 ash incorporated
	2 (BBS)	2 cm	MP=11.2 mm	UB=sharp LB=sharp	Moderately sorted, mL, yellow-brown pumice. P>GJ(~15%)>LC>BR	Fall	
	3 (BBS)	1.3 cm	MP=5.6 mm	UB=sharp LB=sharp	Poorly to Very Poorly sorted, cL/mL with cA/mA, pumice dominated.	Rain Flush	Matrix supported (Figure 6.1.5 B)
	4 (BBS)	4.5 cm	MP=8.0 mm	UB=sharp LB=sharp	Poorly to moderately sorted, cL, finer coarser alteration. Pumice: creamy white-brown>LC (predominantly in fines)	Fall	
	5 (BBS)	0.7 cm	MP=5.6 mm	UB=sharp LB=sharp	mA-cA with vL/fL. Pumice: white-brown, lithic dominated. P ~ LC. Upper 4mm Lapilli dominated	Rain Flush	
	6 (BBS)	0.4 cm	MP=8.0 mm	UB=sharp LB=sharp	Moderately to poorly sorted, mL/cL, white – pale brown Pumice>LC (~10-15%)>O&BR	Fall	
	7 (BBS)	0.6 cm	MP=5.6 mm	UB=sharp LB=sharp	Ashy white-grey mA-cA with fL-mL Pumice. P>C>LC.	Rain Flush	
	8 (BBS)	2.7 cm	MP=16 mm	UB=sharp LB=sharp	Poorly sorted, cL, yellow-brown vesiculated Sa-SR Pumice>LC>O(~35-40%)>GJ	Fall	Clast supported
	9 (BBS)	2.3 cm	MP=5.6 mm	UB=sharp LB=sharp	Ashy white-light grey fA-mA, P>C.	Dilute Gravity Current	(Figure 6.1.5 C.)
	10 (BBS)	3 cm	MP=22.4 mm	UB=sharp LB=sharp	Poorly sorted, cL, yellow-brown vesiculated Sa-SR Pumice>LC>O(~30%)>GJ	Fall	Clast supported

# Appendix 2

Image 1

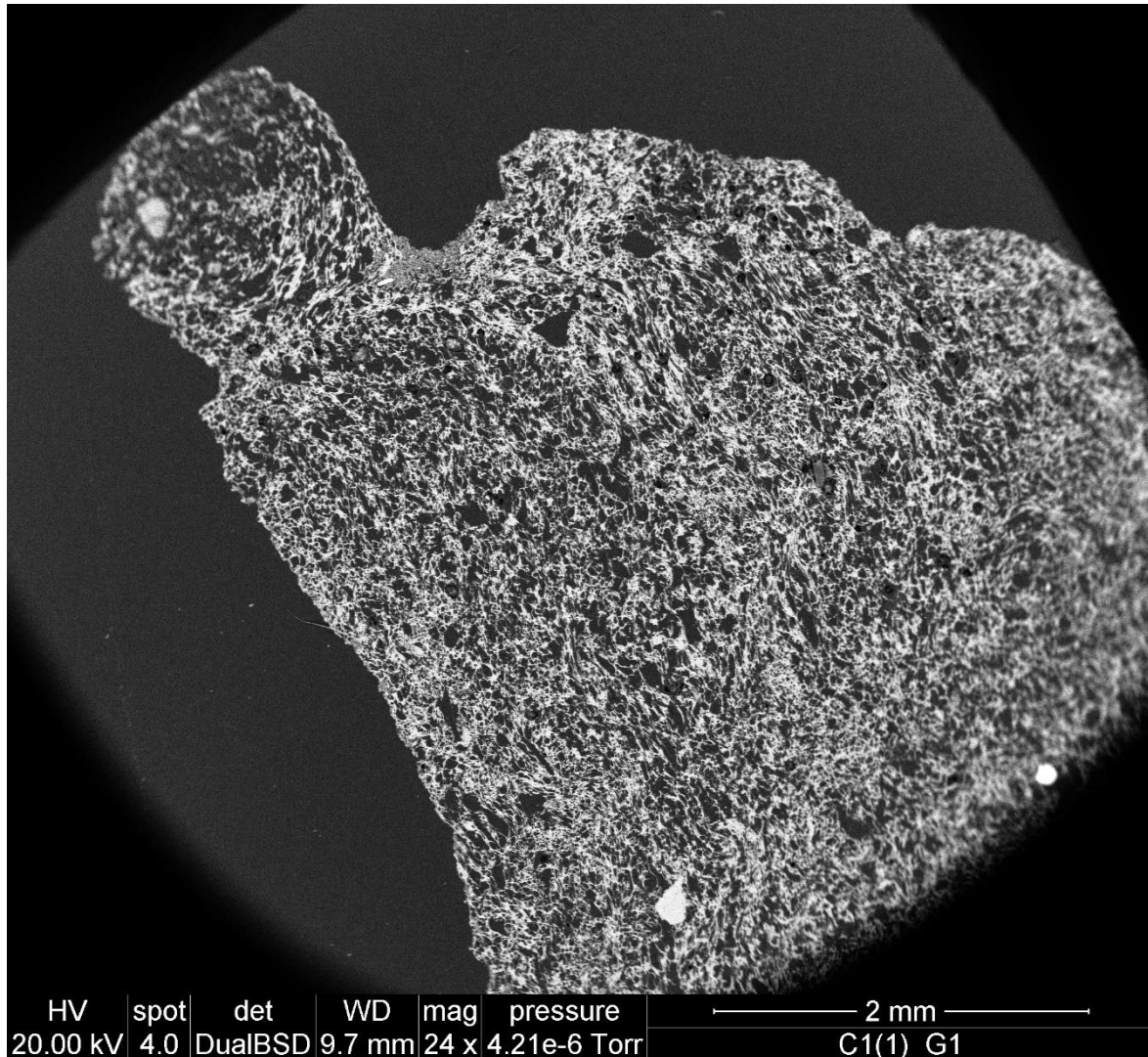


Image 2

